NAT'L INST. OF STAND & TECH R.I.C.
A11105 476688

NIST
PUBLICATIONS

NIST
United States Department of Commerce
Technology Administration
National Institute of Standards and Technology

NIST Technical Note 1500-2
Materials Reliability Series

Procedures for the Electron-Beam Moiré Technique

E.S. Drexler

QC
100
.U5753
NO.1500-2
1998

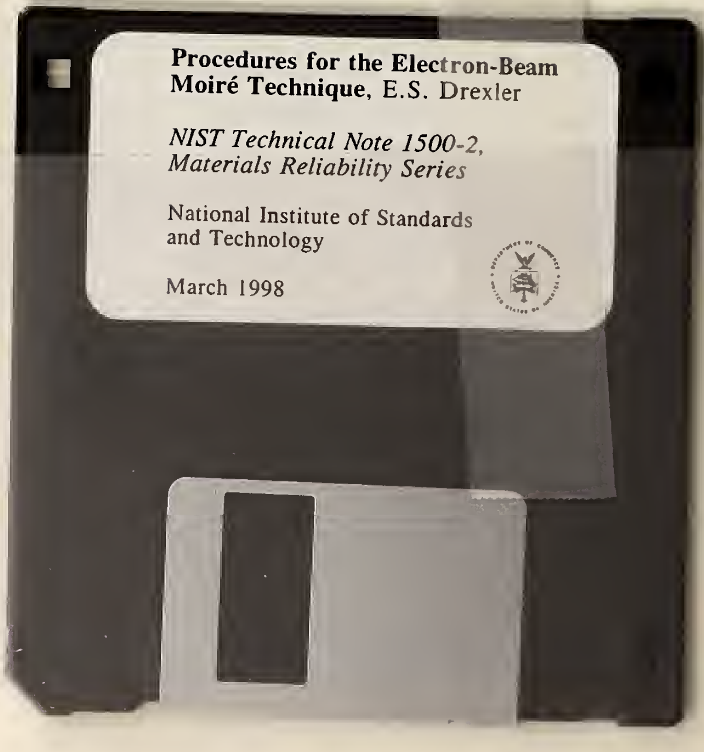

Procedures for the Electron-Beam Moiré Technique, E.S. Drexler

NIST Technical Note 1500-2,
Materials Reliability Series

National Institute of Standards
and Technology

March 1998

NIST Technical Note 1500-2
Materials Reliability Series

Procedures for the Electron-Beam Moiré Technique

E.S. Drexler

Materials Reliability Division
Materials Science and Engineering Laboratory
National Institute of Standards and Technology
325 Broadway
Boulder, Colorado 80303-3328

March 1998

U.S. DEPARTMENT OF COMMERCE, William M. Daley, Secretary
TECHNOLOGY ADMINISTRATION, Gary R. Bachula, Acting Under Secretary for Technology
NATIONAL INSTITUTE OF STANDARDS AND TECHNOLOGY, Raymond G. Kammer, Director

National Institute of Standards and Technology Technical Note
Natl. Inst. Stand. Technol., Tech. Note 1500-2, 140 pages (March 1998)
CODEN:NTNOEF

U.S. GOVERNMENT PRINTING OFFICE
WASHINGTON: 1998

For sale by the Superintendent of Documents, U.S. Government Printing Office, Washington, DC 20402-9325

Contents

Foreword

The Materials Reliability Series of NIST Technical Notes are reports covering significant research accomplishments of the Materials Reliability Division. The Division develops measurement technologies that enable the producers and users of materials to improve the quality and reliability of their products. Measurement technologies are developed for process control to improve the quality and consistency of materials, for nondestructive evaluation to assure quality of finished materials and products, and for materials evaluation to assure reliable performance. Within these broad areas of measurement technology, the Division has focused its resources on three research themes:

- Intelligent Processing of Materials—To develop on-line sensors for measuring the materials' characteristics and/or processing conditions needed for real-time process control.

- Ultrasonic Characterization of Materials—To develop ultrasonic measurements for characterizing internal geometries of materials, such as defects, microstructures, and lattice distortions.

- Micrometer-Scale Measurements for Materials Evaluation—To develop measurement techniques for evaluating the mechanical, thermal, and magnetic behavior of thin films and coatings at the appropriate size scale.

This report is the second in the series. It covers research on electron-beam moiré, one of the projects in our research on Micrometer-Scale Measurements.

PROCEDURES FOR THE ELECTRON-BEAM MOIRÉ TECHNIQUE

E. S. Drexler

National Institute of Standards and Technology
Boulder, Colorado 80303

The background, setup, and procedures for the electron-beam moiré technique are described here. This document is intended to give the reader as many details as possible about the technique, so that the reader will have the information required to conduct e-beam moiré experiments in his or her own laboratory. Essential equipment include a scanning electron microscope (SEM), access to electron-beam or another type of lithography process, and computers to run the lithography process and to aid in reducing and analyzing the data.

Keywords: electron-beam lithography; electron-beam moiré; experimental mechanics; lithography; moiré.

Electron-Beam Moiré

Electron-beam (e-beam) moiré is a recently developed technique first described by Robinson [1], followed by Kishimoto et al. [2]. The technique has been refined and fostered at NIST by Dally and Read [3], its theory described by Read and Dally [4], and its application reported in Referecnes [5–9].

Utilizing many of the principles of video moiré [10], e-beam moiré displays better resolution, as it is conducted in the scanning electron microscope (SEM). E-beam moiré is based on the fundamentals of optical moiré while exploiting the spatial resolution of the SEM. Imaging with an electron beam circumvents the limitations on resolution due to the wavelength of light. In addition to the resolution capabilities of the technique, e-beam moiré has the advantage of being able to see the substrate through the moiré fringe field, so that you can identify how the materials' systems and their structures contribute to local deformations.

As with moiré interferometry, e-beam moiré does not require a separate, tangible reference grating. The reference grating is an integral part of the SEM—the rastering of the electron beam—and exists whenever the current in the filament is sufficient to produce an image. The electron beam rasters across the field of view at regular intervals: 480 raster scans per image for a typical imaging system. The pitch p_r of the "reference grating" depends, therefore, on the magnification and viewing area of the system; specifically, $p_r = S/MR$, where S is the nominal image size, M is the magnification, and R is the number of raster scan lines. S and R are constants that can be obtained from the service manual or the manufacturer of the SEM.

The specimen grating is a series of ridges and trenches generated by e-beam lithography. This lithography takes place in the SEM with the aid of a computer program that controls the location and dwell time of the electron beam. Figure 1 shows the procedure used to make the specimen grating. The polished surface of the specimen is made conductive, then a thin coating of radiation-sensitive resist is spun on, and the specimen is baked to drive off the volatiles from the resist. The radiation-sensitive resist is then exposed to an electron beam in the desired pattern, followed by development of the pattern using a solution of alcohol and solvent to dissolve the exposed areas. Table 1 shows the various grating sizes, types, and pitches that have been obtained with this lithography system.

The magnification is nominally the same for the lithography as it is for imaging. The number of lines contained in the specimen grating is one or two times the number of rasters of the electron beam so that the initial correlation is approximately one-to-one (or one-to-two). A null field, one for which there is an exact one-to-one correlation exists between the specimen and reference gratings, is very rare. Because the SEM is focused and tuned using electromagnetic lenses to adjust for differences in focal distance, it is virtually impossible to replicate tuning conditions between sessions on the SEM. An additional complication is that the SEM used at NIST is not

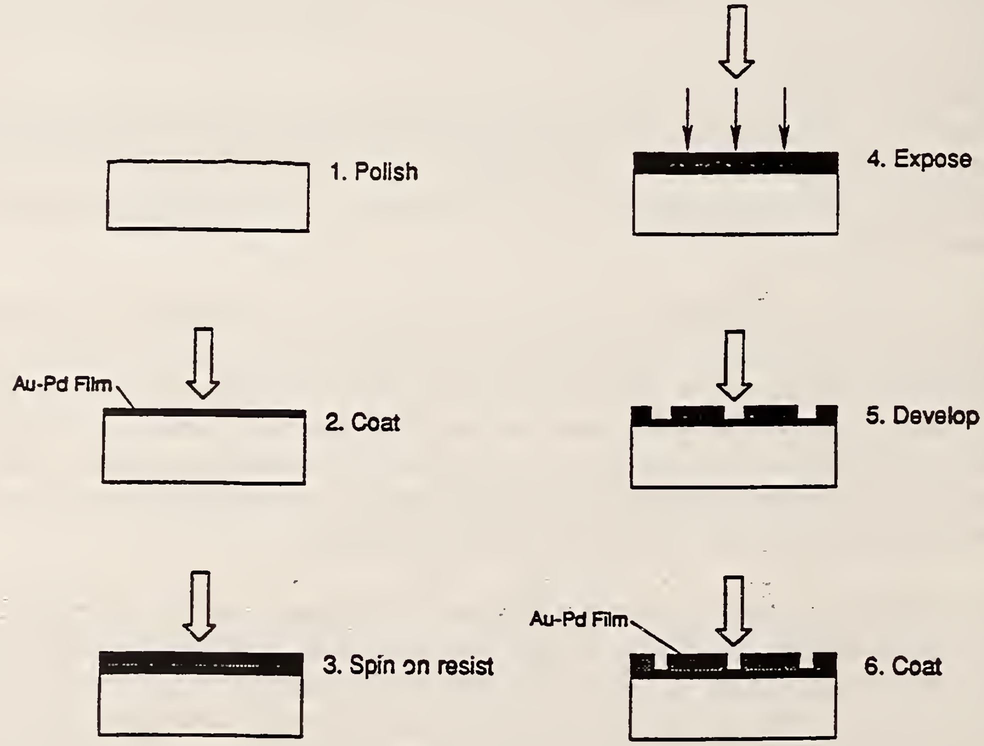

Figure 1. Schematic showing the processing steps in making the specimen grating for e-beam moiré.

Table 1. Sizes and pitches of patterns produced.

PATTERN WIDTH, μm	LINE PITCH, nm	MAGNIFICATION
1000 (L: S, X)*	900	100×
500 (L: S, X)	900	200×
(L: S, X)	450	
200 (L: S, X)	350	500×
(L: S; D)**	175	
100 (L: S; D)	175	1000×
50 (D)	90	2000×

*L = lines, S = single orientation, X = crossed-line gratings
** D = antidots (holes in PMMA)

capable of continuous magnifications; that is, magnifications are available only in increments preset by the manufacturer.

If the pitch of the specimen grating is slightly different than that of the reference grating, moiré fringes will be present for the initial condition. *With e-beam moiré, light and dark fringes are not the result of light passing through a grating, but rather the result of the electron beam interacting with the topography of the specimen grating lines.* The electron signal originating from the corners of the ridges will produce light fringes, whereas the trenches absorb the electrons, producing dark fringes.

A change in the moiré fringe density is the result of the presence of physical deformation in the region of the grating. Expansion in the specimen can produce either an increase or decrease in the density of fringes depending on the initial condition. If in the initial condition the pitch of the specimen grating is larger than that of the reference grating, expansion will lead to more fringes. If, however, the pitch of specimen grating is smaller than that of the reference grating, expansion will move the pitch size closer to a one-to-one correspondence, and therefore fewer fringes. Figure 2 demonstrates this concept. The origin of the x-axis is defined as the null condition, fringes to the right of the origin are fringes of expansion, $(+)N$, and fringes to the left are fringes of contraction, $(-)N$. If our initial condition is to the left of the origin and the specimen is expanded, the number of fringes will decrease until the null condition is achieved, after which the number of fringes will again increase. If, rather, the specimen is contracted, the number of fringes of contraction will increase. The reverse is true if the initial condition is to the right of the origin. Expansion will result in an increased number of fringes of expansion, and contraction will lead to fewer fringes until the null condition results, followed by an increasing number of fringes of contraction.

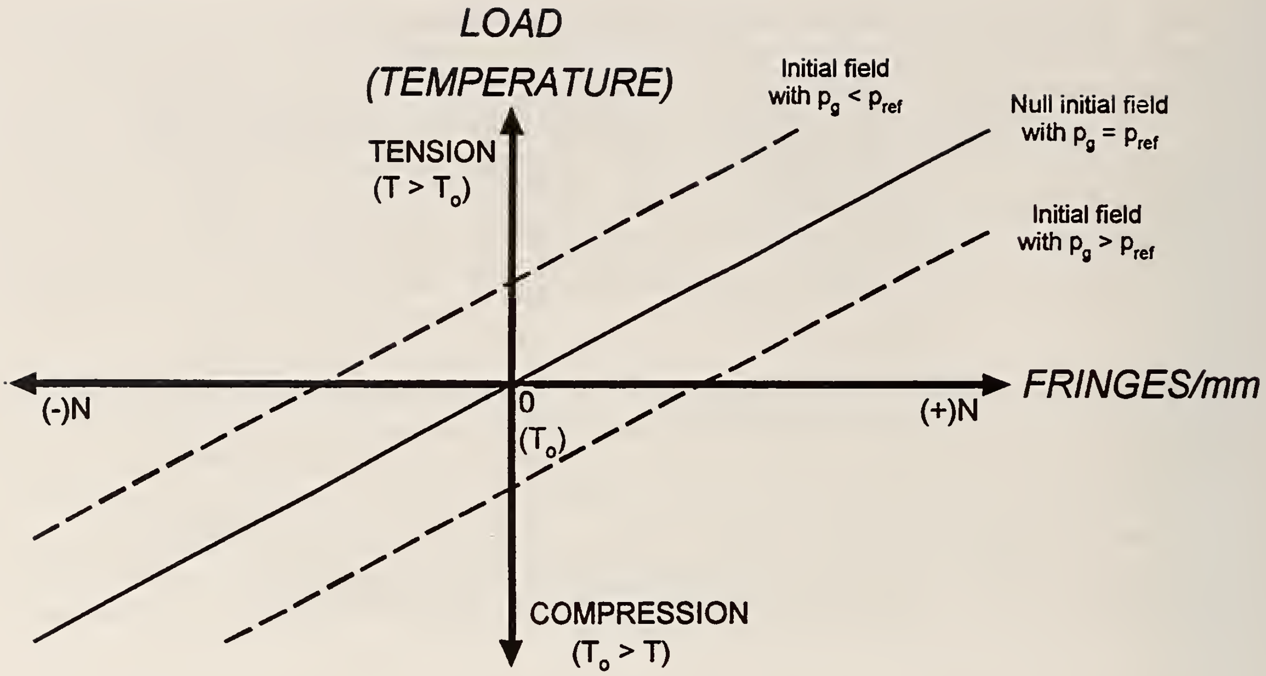

Figure 2. Diagram showing the relationship between positive and negative fringes, and the relative pitch of the specimen and reference gratings in the initial fringe field. In this figure, (+)N are fringes of expansion and (–)N are fringes of contraction.

In the more familiar optical-moiré system shown in Figure 3, for every line from the specimen grating that moves out of the field of view, one moiré fringe appears [11]. Knowing the pitch of the "reference grating" and the initial fringe density allows the quantification of strain either across the entire grating or at a local feature.

The resolution of the technique ranges from 90 to 900 nm/fringe order. Determination of values for strain from the moiré images depends on the pitch of the specimen grating and the ability to perceive fractions of fringes. How well you can discern fractions of fringes depends on the total number of fringes in the field of view and on the contrast. If only 4 fringes were present, it would be easy to detect, say, 1/10 or even 1/20 of a fringe with good contrast. However, if 25 fringes were in the field of view, perhaps 1/4 of a fringe is the best that you could delineate. Therefore, the resolution of the technique would fall in a band ranging from 225 nm to 9 nm.

The mathematical developments for determining engineering normal (ε) and shear (γ) strains follow those for geometric moiré. For small strains and small rotations

$$\varepsilon_x = \partial u_x/\partial x, \ \varepsilon_y = \partial u_y/\partial y, \tag{1}$$

$$\text{and } \gamma_{xy} = \partial u_x/\partial y + \partial u_y/\partial x, \tag{2}$$

where u_x and u_y are the displacements measured from the 0 and 90° images, respectively. In moiré $(u_x, u_y) = N_{(x,y)} p_r$, where $N_{(x,y)}$ is the fringe order. (Throughout the remainder of this paper u_x-field

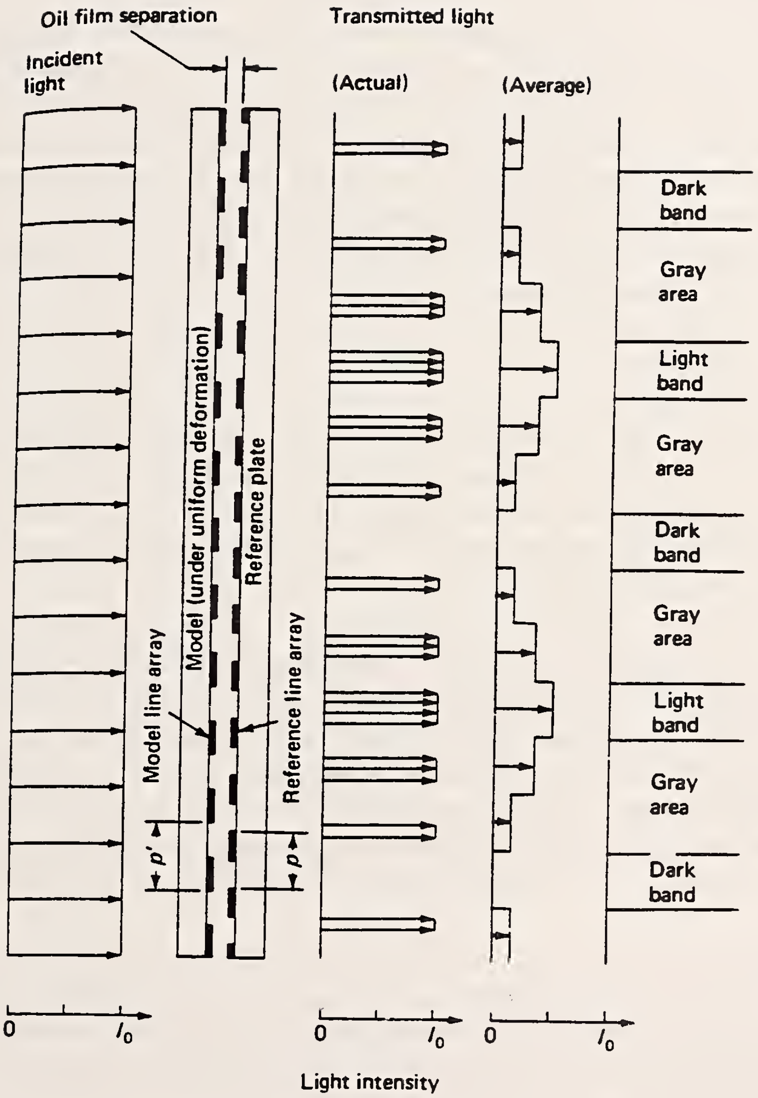

Figure 3. Schematic of an optical moiré system showing the light transmission through a specimen and reference grating where $p_r \neq p_s$. (From J.W. Dally and W.F. Riley, Moiré methods, Chapter 11 in *Experimental Stress Analysis.* New York: McGraw-Hill; 1991 [11]. Used with permission of McGraw-Hill.)

and 0° will refer to the observed images where the grating lines are perpendicular to the longest dimension of the specimen, and u_y-field and 90° to images having the grating lines parallel to the longest dimension.)

Please see Dally and Riley [11] and Durelli and Parks [12] for a complete review of the mathematical development characterizing geometric moiré, and References [3 and 4] for the theory behind e-beam moiré. (Appendix A contains all published material from NIST researchers on e-beam moiré.)

There are limitations to this technique, as it is conducted at NIST. Displacements are available only from the in-plane surface of the specimen. No attempt has been made to measure out-of-plane displacements. A single e-beam moiré image cannot provide any quantitative information; the technique relies on the changes observed in the fringe field from an initial condition. Another disadvantage is the inability to assign a precise fringe order to the moiré fringes observed. Because the pattern covers a limited area and not a region extending to a free surface, fringe orders must be assigned arbitrarily. The significance of this is that absolute displacements are not usually quantifiable; strains, however, are.

Specimen Preparation

At the Materials Reliability Division of NIST we have studied a number of electronic packaging specimens with e-beam moiré. These include plated through-hole, ball-grid array, isotropically and anisotropically conductive adhesive, and high-density interconnect specimens. The e-beam moiré technique has been used to measure regions of high relative displacements among the materials contained within the package.

A specimen is cross sectioned so that it is approximately 3mm to 4 mm thick. The sectioned specimen is ground flat and parallel on both sides using SiC paper in several steps from 120 to 1200 grit if the materials have nearly the same hardness, and on diamond-imbedded film if there is a great disparity in hardnesses. Lapping/polishing fixtures are commercially available to aid in making specimens that are flat with parallel faces. One side of the specimen is then polished with 6 μm diamond spray on a napless synthetic silk polishing cloth. Following the polish the surface is cleaned with methanol and cotton batting, and dried with clean, filtered (to 0.1 μm) compressed air.

On the day that the gratings are to be written, each specimen receives a final polish with 1 μm diamond spray on synthetic silk polishing cloth. Once again the specimen is cleaned with methanol and cotton batting, and the surface is dried with clean, filtered compressed air. The specimen is placed in a methanol ultrasonic bath for 30 s, followed by surface cleaning with acetone and cotton batting, and drying with compressed air.

AuPd is deposited using a sputter coater [13]. A sputter coater works by dislodging material from a source with argon ions accelerated in an electric field and depositing the source atoms onto the surface of the specimen. The specimen remains cool throughout the process.

To apply a thin, even coat of polymethyl methacrylate (PMMA), it is spun onto the surface of the specimen. The PMMA is purchased in a chlorobenzene solution with 4 percent solids. For our purposes this solution is cut in half by mixing a one-to-one solution of the purchased PMMA with chlorobenzene to form a 2 percent solids solution of PMMA. Held onto the surface of the spinner by a vacuum, 3 to 5 drops of 2 percent PMMA are placed on the surface of the specimen, then the specimen is spun at 2250 rpm for 30 s. The specimen is then placed on an aluminum block on a hot plate with the block preheated to 170 °C, and cured at this temperature for 1 h to drive off the chlorobenzene. If 170 °C exceeds the temperature limit for the specimen, an alternative cure schedule of 100 °C for 2 h is acceptable. The specimen is now ready for lithography.

Electron-Beam Lithography

The lithography is performed in an SEM [14]. D.T. Read of NIST wrote a BASIC program (Appendix B) that controls the location and dwell time of the electron beam, generating regularly-spaced straight lines. Lines are actually a series of closely-spaced, overlapping spots. To obtain crossed-line gratings the lines are written in one orientation first, then the specimen is "rotated" 90° and the lithography process is repeated. This “rotation” takes place electronically rather than physically—the x output from the photomultiplier is sent to the y input of the CRT, and vice versa. The effect is the same as if the specimen were rotated clockwise ~90°. (The rotation is accurate to ±1° and precise to ±20" .) The rotation unit [15] used performs the input/output exchange with a flick of a switch.

Through an input file into the program, the operator specifies the size of the pattern in magnification, the number of lines, the probe current, and the number of dwell stops on the scan line. The PMMA is very sensitive to the electron beam, so at no time can one look at the surface of the specimen under normal “illumination,” but must locate where to place the pattern using a probe current of extremely low intensity (≤0.2 pA).

The microscope is set to 20 kV of accelerating voltage to write the patterns. An aperture of 50 μm is chosen to focus the beam as tightly as possible. The astigmatism, centering of the aperture, working distance, and focus are also carefully adjusted and tuned in order to obtain as small a spot size as possible. A small spot size for the electron beam is necessary, particularly when we attempt to obtain line pitches of 90 to 225 nm.

Writing the actual patterns is a matter of locating where you want to place the pattern, setting the magnification to the desired viewing area, and adjusting the probe current with the fine and coarse potentiometers on the SEM to that specified in the computer input file. A Faraday cup measures the probe current and blocks the beam from reaching the surface of the specimen until the computer takes control of the electron beam to begin writing the pattern.

When all the patterns on a given specimen are written, the specimen is removed from the SEM for development. During exposure the electron beam breaks the polymer chains of the PMMA, but development of the specimen is required to wash those broken polymer chains away. The developer is a 3:1 solution of isopropanol and methyl isobutyl ketone (MIBK). Gently the specimen is agitated in the isopropanol/MIBK solution for 40 s, then rinsed in a stream of isopropanol for 20 s, followed by a 30 s rinse in deionized water. Clean, filtered compressed air is used to dry the specimen. At this point it is often possible to see diffraction of light on those patterns with line pitches >350 nm. The lines are visible in the optical microscope for line pitches of the same magnitude. But in order to see the quality of lines with finer pitches, it is necessary to look at them in the SEM. Following development, however, the surface of the specimen is a nonconductive polymer. This surface will become electrically charged in the SEM so that it is impossible to view the patterns. Deposition of a thin (<10 nm) coating of AuPd is deposited over the polymer provides a conductive surface.

Once the surface of the specimen is coated with AuPd, it can be returned to the SEM and the quality of the patterns evaluated. There are three reasons a pattern can be rejected for use; it may be overexposed, underexposed, or inconsistently exposed. Inconsistent exposure can arise when the specimen is not perfectly flat in the area of the pattern—either the specimen as a whole is not flat or the softer regions are gouged out. If the beam's focal point is above the surface of the specimen, the pattern will be insufficiently exposed, resulting in lines with poor contrast or no lines at all. If the beam's focal point is below the surface, the interaction area may be so large that the overexposed lines touch each other, or all the PMMA is exposed and removed upon development.

Another cause of inconsistent exposure is having a specimen containing components with vastly differing molecular or atomic masses. As the primary electron beam enters a material, the electrons interact with that material (Figure 4). The secondary electrons used to image the

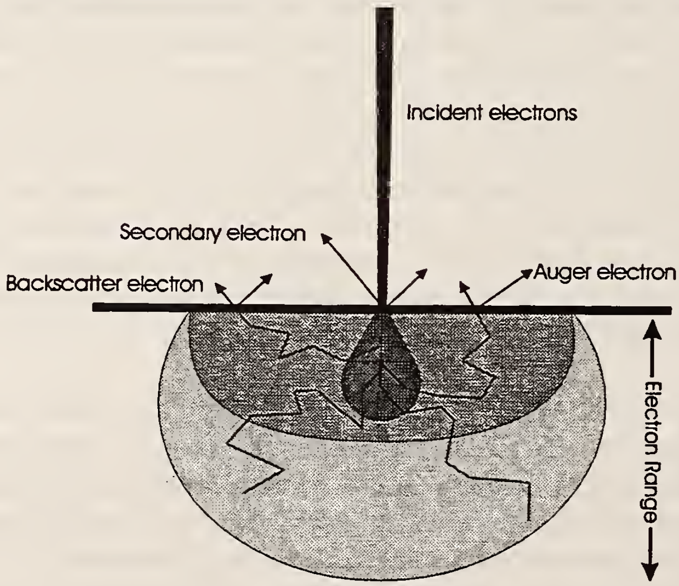

Figure 4. Origin and depth of incident, secondary, backscattered, and Auger electrons. The incident electrons affect the area of the dark bulb, the secondary electrons emit from the near-surface, the backscatter and Auger electrons originate from the intermediate area, and the lightest stippled area indicates the region from which the electrons are unable to reach the surface.

surface scatter elastically from near the surface. Backscattered electrons are the result of inelastic collisions. The heavier the material the more energy the backscattered electrons have. This energy allows the backscattered electrons from a larger interaction area to reach the surface. Herein lies the problem with electron-beam lithography across materials with disparate backscattered-electron energies. The PMMA resist is sensitive to electrons—whether secondary or backscattered. If, for example, an exposed region contains Si and Au, the Si has an atomic mass of ~28 g/mol and the Au 197 g/mol. The exposed Au will have a much larger interaction area than the Si, resulting in the Au being overexposed as compared with the Si.

Thermal Testing

The thermal load testing of a specimen is conducted in the SEM using a heating/cooling stage [16] (Figure 5). The stage has a temperature range of –196 to 400 °C, but testing of electronic packages is usually conducted in the nominal range of –50 to 150 °C. Cooling is provided by liquid-nitrogen–cooled nitrogen gas that flows through tubing in the stage. A PID (proportional, integral, derivative) controller maintains the set temperature by balancing the heater output with the chilled gas.

The patterns are usually observed under a low accelerating voltage (5 kV to 7 kV), a working distance of 13 mm to 15 mm, and a probe current of 10 pA to 12 pA in order to optimize the resolution without damaging the PMMA. Before any images are acquired, the stage is cycled between 0 °C and 100 °C (or over an appropriate temperature range in the elastic-strain regime) twice before returning to the ambient temperature noted when the filament was first saturated. The objective is to ensure that any macroscopic adjustments occur before the start of image

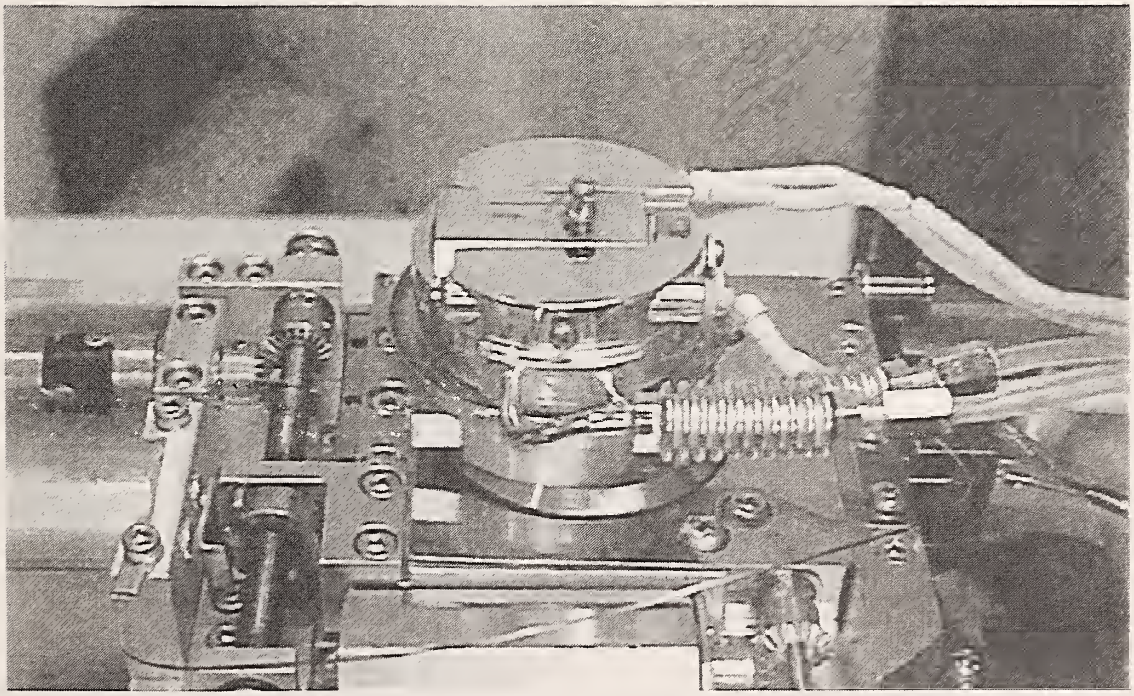

Figure 5. Photograph of the heating/cooling stage used at NIST.

acquisition. The one-hour period required to do this cycling also gives the electron beam time to stabilize. The electron beam must be stable in order for the data to be reproducible [17]. Images are then stored digitally from both orientations at ambient temperature. Typically 0° and 90° images are collected at regular temperature intervals (usually 50 °C) until the maximum temperature is attained. During thermal unloading, images are collected at an intermediate and at the minimum temperature.

Mechanical Testing

Mechanical tests are conducted in the SEM on a stage [18] with a motor-driven screw-type actuator and a load capacity of ~4450 N (Figure 6). With the present hardware it is capable of only uniaxial compression and tension. A universal joint used to drive the stage, and the wires that monitor the load and displacement, have access into the SEM chamber through a plate that replaces the side port.

The gage length of the specimen is limited to ~15 mm. It is loaded onto the stage with wedge grips, and each end is tightened with two bolts. The motor speed is regulated with a pot-type knob that sets the rate between 0 and 100 percent of 330 rpm. Most of the loadings are conducted at ~15 percent, taking <1 min to load 90 N. The load is read off a digital display on the controller for the stage. Images from the 0° and 90° orientations are acquired at regular load intervals, and a final image is collected at the end of the test at a load of 0 N.

The conditions for observing the moiré fringe fields are an accelerating voltage of 5 to 7 kV, a working distance of 16 to 18 mm, a probe current of 10 to 20 pA, and the appropriate

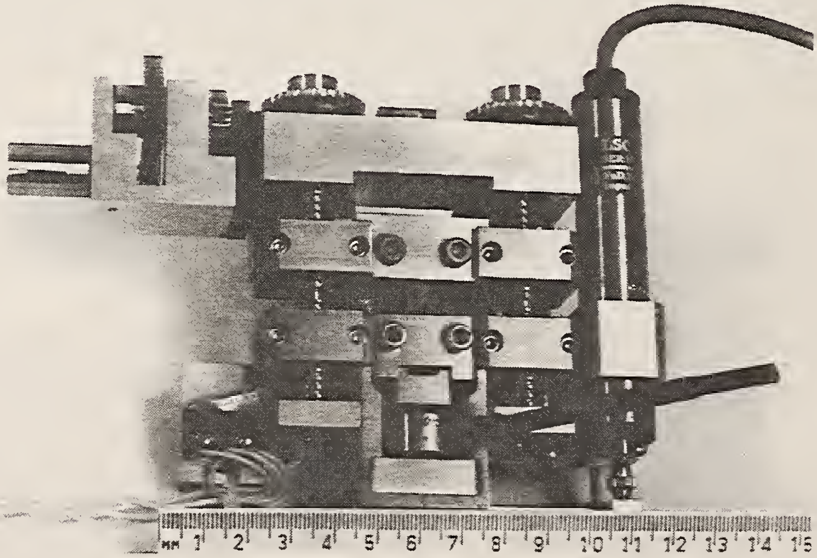

Figure 6. Photograph of the mechanical stage used at NIST.

magnification. The filament should be saturated for a minimum of 60 min before the first images are acquired.

Analysis of the Moiré Fields

A fringe tracing program that was written by D.T. Read of NIST-Boulder (Appendix B) allows you to assign a locus of points that defines the center of the fringe. This fringe center is also a contour of equal displacement on the surface of the specimen. The effect of the crossed-line grating is analogous to having a full-view 0-90° displacement gage with resolution on the order of tens of nanometers. Thus, strains calculated from data obtained with this technique are fully quantitative.

Once the fringe centers have been identified, analysis may be completed in the manner described by Reference [19] in the chapter on geometric moiré. Figure 7 shows the general procedure followed. The fringe centers are identified on the u-field and v-field images. Line profiles are chosen running perpendicular and parallel to the orientation of the lines of reference grating on each image.

Programs designed to reduce and analyze moiré fringe fields are commercially available. This author cautions the reader to verify that the analysis program works on e-beam moiré images. Because the substrate material is visible through the fringes, the fringe intensity, or gray-scale, may be different on different adjacent materials.

A graph is made of the distance along the chosen trace versus the assigned fringe order. The fringe order is then converted into length by multiplying by the pitch of the reference grating, p_r. (Recall that each fringe is the result of a frequency mismatch between the specimen and the reference gratings of one complete line.) The example shown in Figure 7 assumes that the initial fringe field is null. However, with e-beam moiré the initial fringe field is rarely null, so every subsequent image is analyzed by studying the difference between it and the initial condition image.

In the thermal tests an initial room-temperature image is collected, followed by images collected at regular temperature intervals between –50° and 150 °C. Similarly, in the mechanical loading tests an image is collected before applying a load, then subsequent images are collected at regular load intervals. The slopes obtained from the line profiles from the initial images must be subtracted from the slopes from the line profiles from subsequent images to see how each loading step affected the fringe field. Strain data are calculable from these plots of relative displacement versus position along the trace. The slopes of the curves, $\partial u_x/\partial x$ and $\partial u_y/\partial y$, from the line profiles perpendicular to the orientation of the reference grating in the u_x-field and u_y-field images, respectively, are the normal strains as given by eq (1). The shear strain is the sum of the slopes from the curves obtained parallel to the orientation of the lines of the reference grating, $\partial u_x/\partial y + \partial u_y/\partial x$, as given by eq (2). The strains are, therefore, fully quantifiable and locally significant.

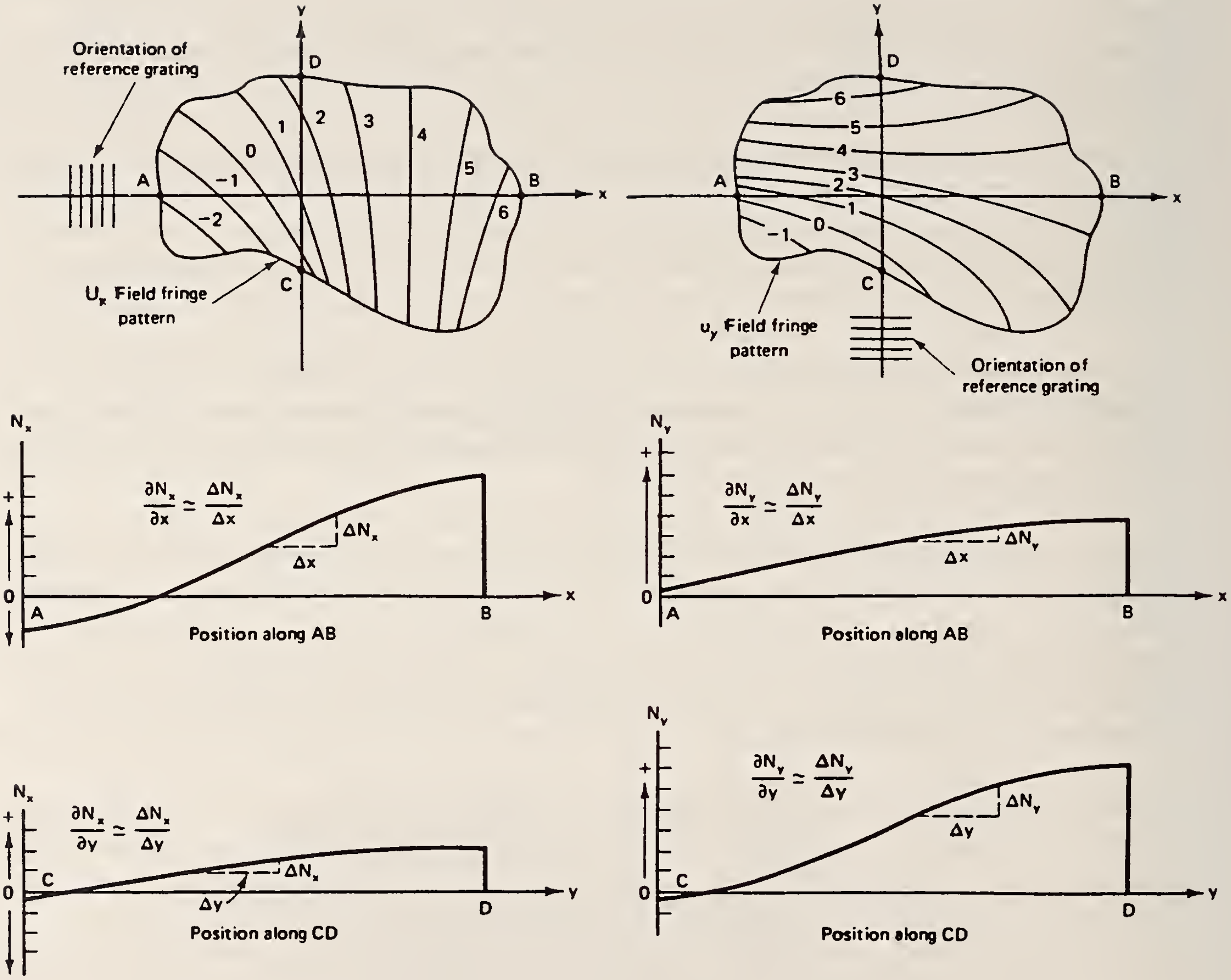

Figure 7. Procedure used to analyze the moiré fringe data (From V.J. Parks, Geometric moiré, in *Handbook on Experimental Mechanics*, edited by A.S. Kobayashi, first edition, published for the Society of Experimental Mechanics, Inc. Englewood Cliffs, NJ: Prentice-Hall; 1987 [19]. Used with permission of Prentice-Hall.)

References

[1] Robinson, D.W. High resolution moiré contouring by a hybrid technique combining light and electron optics. *Opt. Laser Technol.* 13: 145–149; 1981.

[2] Kishimoto, S.; Egashire, M.; Shina, N. Measurements of grain boundary sliding and observations of microgrids for high temperature use. *J. Soc. Mater. Sci. Jpn.* 40: 637–641; 1991.

[3] Dally, J.W.; Read, D.T. Electron-beam moiré. *Exp. Mech.* 33: 270–277; 1993.

[4] Read, D.T.; Dally, J.W. Theory of electron-beam moiré. *J. Res. Natl. Inst. Stand. Technol.* 101: 47–61; 1996.

[5] Read, D.T.; Dally, J.W. Local strain measurements by electron beam moiré. P.A. Engel and W.T. Chen, eds. *Proc., ASME 1993international electronics packaging conference, Advances in electronic packaging, Vol. 1: Structural analysis materials and processes design reliability,* EEP-4–1; 1993 Sept. 29–Oct. 2, Binghamton. NY. New York: ASME: 163–169; 1993.

[6] Read, D.T.; Dally, J.W. Electron-beam moiré study of fracture of a glass fiber reinforced plastic composite. *Trans. Amer. Soc. Mech. Eng.* 61: 402–409; 1994.

[7] Read, D.T.; Drexler, E.S. Local deformation of plated through holes under thermomechanical loading. M.A. Schen, H. Abe, and E. Suhir, eds. Proc., *ASME 1994 international mechanical engineering congress and exposition, Mechanics and materials for electronic packaging, Vol. 2: Thermal and mechanical behavior and modeling.* AMD-187; 1994 Nov. 6–11, Chicago, IL. New York: ASME: 185–194; 1994.

[8] Drexler, E.S. *Thermal and mechanical deformation of conductive adhesives using electron-beam moiré.* M. S. Thesis in Materials Science. Golden, CO: Colorado School of Mines: 116 pp.; 1996.

[9] Drexler, E.S.; Berger, J.R. Electron-beam moiré study of local deformation in conductive adhesives. S.K. Groothuis, P.S. Ho, K. Ishida, and T. Wu, eds. Materials Research Society Symposium Proceeding 445: Electronic Packaging Materials Science IX. Pittsburgh, PA: MRS: 75–80; 1997.

[10] Morimoto, Y.; Hayashi, T. Deformation measurement during powder compaction with a scanning moiré method. *Exp. Mech.* 24: 112–116; 1984.

[11] Dally, J.W.; Riley, W.F. Moiré methods, Chapter 11 in *Experimental stress analysis.* New York: McGraw-Hill: 389–423; 1991.

[12] Durelli, A.J.; Parks, V.J. *Moiré analysis of strain.* Englewood Cliffs, New Jersey: Prentice-Hall: 399 pp; 1970.

[13] Model 6.2 Hummer sputter coater, manufactured by Anatech Limited.*

[14] Model 6100 SEM, manufactured by JEOL.*

[15] Rotation unit, designed by Advanced Microscopy Technology.*

[16] Model C1003 heating and cooling stage, manufactured by Oxford Instrumemts.*

[17] Berger, J.R.; Drexler, E.S. Error analysis and thermal expansion measurement with electron-beam moiré. Submitted to *Exp. Mech.*

[18] Mechanical stage, no. 18211, manufactured by Ernest Fullam, Inc.*

[19] Parks, V.J. Geometric moiré in *Handbook on experimental mechanics*, A.S. Kobayashi, ed. Englewood Cliffs, New Jersey: Prentice-Hall: 282–313; 1987.

* Trade names are furnished to provide the reader with exact details on the equipment used by NIST and to evince the commercial availability of the equipment discussed. Such identification implies neither recommendation nor endorsement by NIST; other apparatus from other sources may be found that work as well.

Appendix A: Publications

A1

Electron Beam Moiré

by Dally and Read (1993)

Electron Beam Moiré

by J. W. Dally and D.T. Read

ABSTRACT—A method of writing very high frequency line and dot patterns, in excess of 10,000 lines/mm, is described. This method uses a very small diameter, 10 to 20 nm, beam of electrons to sensitize a 100-nm thick layer of electron resist. The line and dot patterns are produced by etching the sensitized resist. Moiré fringe patterns occur when the line arrays are observed in the scanning electron microscope. Moiré fringes with excellent contrast have been produced at magnifications as high as 1900×. This capability permits e-beam moiré to be employed in micromechanics. Examples of line arrays, dot arrays and moiré fringe patterns on a brass disk and on a tensile specimen fabricated from glass-fiber-reinforced plastic are demonstrated to introduce the possibilities for micromechanics applications.

Introduction

Since its introduction by Weller and Shepard[1] in 1948, the moiré method of displacement and strain analysis has been improved by introducing new techniques and new technologies. The development of geometric or mechanical moiré methods, which occurred during the period from 1948 to 1970, has recently been reviewed by Parks[2] and has been described in detail by Theocaris.[3] Since 1980, most of the development has involved moiré interferometry where diffraction gratings are produced by interference of two plane beams from a coherent light source.[4, 5] Moiré interferometry represented a major advance because the frequency of the specimen grating was increased by a factor of about 50 to 4,000 ℓ/mm. This increase improved the sensitivity of the method and extended the applicability of the moiré method to a wider range of problems.[6]

Since further increases in the frequency of the specimen gratings are limited by the wavelength of light, it is necessary to employ a nonoptical method to achieve line arrays with frequencies of 10,000 ℓ/mm or higher. Our colleagues[7] in high resolution lithography have already solved this problem by writing very fine lines using an electron beam. Patton[8] used lines written with an electron beam to study slip at grain boundaries. Kishimoto *et al.*[9,10] were the first to introduce e-beam moiré and to demonstrate its application to study microdeformation. In these studies, relatively coarse gratings were produced with pitches between 3.7 and 7.1 μm. The moiré fringe patterns were produced by interfering the lines in the array with the scanning lines in a conventional scanning electron microscope (SEM). This method of moiré fringe formation is similar to video-scanning moiré introduced by Morimoto *et al.*[11] in 1984.

This paper describes a study of e-beam writing methods to produce very high-frequency line and dot gratings (10,000 ℓ/mm) which are suitable for moiré applications. Examples of line and dot gratings are presented to show the quality of the arrays which can be produced with this method. The ability to write patterns on both homogenous and heterogenous materials such as glass-fiber-reinforced plastics is demonstrated. The application of e-beam moiré at high magnification (1,900×), which is required in micromechanics, is emphasized. Finally, a moiré pattern from a high frequency line array (10,000 ℓ/mm), which represents the displacement field at interfaces in a GFRP specimen, is described.

e-Beam Generation and Control

Let us consider the column of a typical SEM shown in Fig. 1 to introduce the methods used to generate and control an electron beam. The electrons are generated by thermionic emission at a heated tungsten filament, which has a V-shaped tip about 200 μm in diameter. The filament is maintained at a high negative voltage during operation. The electrons emitted are accelerated to the anode (ground) with acceleration voltages that are adjustable from about 1 to 50 kV.

A Wehnelt cylinder with a circular aperture centered on the filament apex is biased negatively with respect to the cathode. The effect of the filament, Wehnelt cylinder, and anode is to produce a stream of electrons which converge with a crossover diameter d_0 and a divergence angle α_0 as

---

J.W. Dally (SEM Fellow) is Professor of Mechanical Engineering, University of Maryland, College Park, MD 20742. D.T. Read (SEM Member) is Physicist, National Institute of Standards and Technology, Materials Reliability Division, Boulder, CO 80303.

Original manuscript submitted: June 10, 1992. Final manuscript received: April 14, 1993.

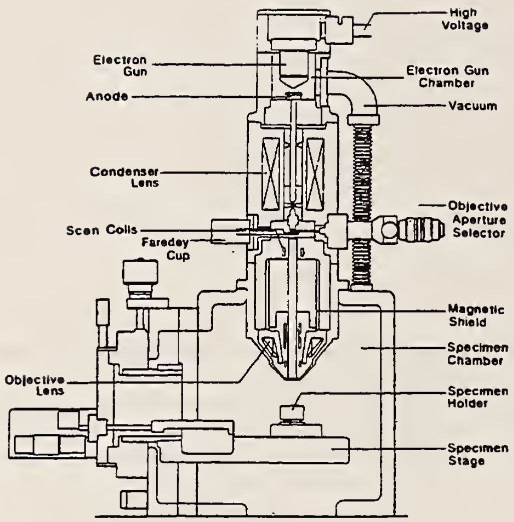

Fig. 1(a)—Schematic diagram of elements in the vacuum column of an SEM

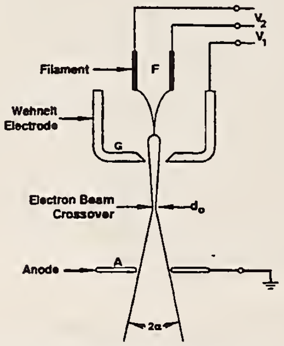

Fig. 1(b)—The gun used in forming the electron beam

illustrated in Fig. 1(b). A typical value of d_0 is 25 µm, and a typical value of α_0 3 mrad. Conventional electromagnetic lenses are positioned in the SEM column to focus the electron beam by the interaction of the electromagnetic field of the lens on the moving electrons. The condenser and objective lens are used to reduce the beam diameter by a factor of 1,000 or more, to the final spot diameter d_f of 5 to 20 nm on the specimen.

The objective (or probe-forming) lens is different from the axially symmetric condenser lenses. This lens must accommodate many detectors located near the specimen. Its magnetic field must not affect the collection of secondary electrons from the specimen. Also, the bore of the lens must accommodate scanning coils, stigmator, and beam aperture. The objective lens is used to focus the electron beam at different specimen working distances, which usually range from about 10 to 40 mm. The spot size is minimized by reducing the working distance to improve resolution of the SEM. However, the depth of field is increased by increasing the working distance, which produces a smaller divergence angle a. The depth of field is also dependent on the beam limiting aperture as indicated in Table 1.

TABLE 1—TYPICAL DEPTH OF FIELD WITH A WORKING DISTANCE OF 10 MM[12]

Magnification	Aperture Diameter (µm)			
	50	100	200	500
	Depth of Field (µm)			
10^1	8000	4000	2000	800
10^2	800	400	200	80
10^3	80	40	20	8
10^4	8	4	2	0.8

e-beam Characteristics

The diameter of the e-beam is of critical importance in writing either line or dot patterns to produce a high resolution moiré grating. The variables which affect the beam diameter include the filament material, the accelerating voltage, and the probe current. The probe current is the electrical current transmitted as the electron beam from the filament to the specimen. Typical results[12] for the beam diameter as a function of probe current are shown in Fig. 2. Since we seek to minimize beam diameter, low probe currents (10 to 50 pA) are employed with higher acceler-

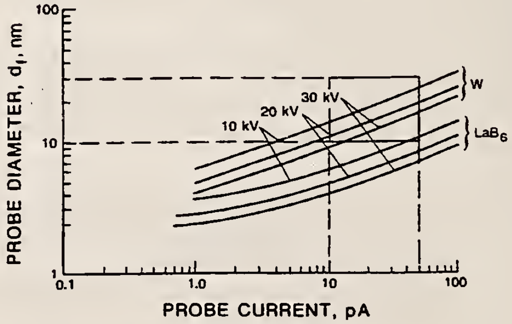

Fig. 2—Electron beam diameter as a function of probe current, filament material and accelerating voltage

ating voltages (20-30 kV). The filament material used was tungsten, although lanthanum hexaboride, LaB_6, produces a tighter beam. Inspection of Fig. 2 shows that the beam diameter ranges from about 10 to 20 nm as the probe current increases from 10 to 50 pA with an accelerating voltage of 30 kV. The beam diameter increases as the accelerating voltage is decreased.

It is important to note the difference between the filament current and the probe current. The filament current, about 200 to 240 μA, heats the tungsten filament and produces the electrons at the gun [see Fig. 1(b)]. The probe current is the incident current produced by the electron beam striking the specimen. The probe current is adjusted with the condenser lenses (for a given aperture). Increasing the magnification of a condenser lens increases the divergence angle, and a larger portion of the electron beam is blocked by the beam-limiting aperture. This blockage reduces the current in the beam.

The probe current is measured with a Faraday cup, that is inserted into the beam of electrons. Because the Faraday cup does not allow either backscattered or secondary electrons generated by the incident beam to escape, the current flowing from the cup to ground is due entirely to the incident beam. The probe current is measured with a dc picoammeter.

This description shows that a beam of electrons with a diameter in the range of 10 to 20 nm can be produced in a typical SEM. Moreover, by controlling the scanning coils, this beam can be directed over the surface of the specimen to trace any specified pattern on the x-y plane. This beam is employed to write high density line and dot gratings for application in micromechanics.

e-beam—PMMA Interactions

The interaction of the electron beam with solids has been employed since 1968[7] to write intricate patterns required to fabricate very dense microelectronic devices. Certain plastics, such as polymethylmethacrylate (PMMA), undergo a chemical change during electron bombardment. The electrons sensitize the exposed material to etching in a suitable solvent. The etching rate is controlled by the electron dose, and etch boundaries are determined by contours of electron energy deposition. The electrons involved in sensitizing the PMMA come from the incident electron beam, the backscattered electrons, and the secondary electrons. The shape of the etch pit in monolithic PMMA[13] resembles a pear because of inelastic and elastic scattering of the electrons. The depth and width of the pear-shaped cavity depends on the electron dose, number of electrons per unit volume, and the developing time in the solvent.

Writing in a thin uniform layer of PMMA on a substrate is more difficult than writing in monolithic PMMA, because backscattered electrons and secondary electrons from the substrate also contribute to the electron dose. One attempts to write either line or dot patterns in e-beam moiré with exceedingly small pitch. The incident beam is the most important source of the electron dose. Indeed, if the incident beam were the only source of electrons, it would be possible to write line and dot arrays with a pitch of 20 to 40 nm, since the incident beam diameters in the range of 10 to 20 nm can be achieved. The effect of elastic and inelastic scattering of the electrons as the incident beam enters the PMMA is to increase the diameter of the beam. However, this effect is minimized by reducing the thickness of the layer of PMMA to 100 nm.

Backscattered electrons from the substrate increase the diameter of the spot of PMMA being exposed. The number of backscattered electrons, those that enter the substrate and reemerge in the PMMA layer, is relatively large (about 30 percent in copper[12]). Large numbers of backscattered electrons are useful in scanning electron microscopy because they provide a signal that is detected to define the surface features of a specimen. However, in e-beam writing, the backscattered electrons are detrimental because they increase the minimum feature size that can be subjected to a controlled dosage. The fraction of electrons (relative to the incident beam) that is backscattered depends on the atomic number of the substrate with the backscatter coefficient increasing with atomic number. Line and dot arrays with very small pitch can be achieved in a very thin PMMA layer on substrate materials with low atomic number.

e-beam Writing Experiments

A series of experiments were performed to determine the parameters to employ in writing line and dot arrays and the minimum pitch which could be achieved. Aluminum, brass, and GFRP were used as the substrate materials. The metallic substrates were disks 12.7 mm in diameter and 1 to 2 mm thick. The GFRP was a strip 6 × 32 mm by 2 mm thick. The surfaces of the specimens were ground smooth and flat using a series of water-lubricated abrasive-coated papers ending with 5-μm grit. The final polish was achieved by finishing with 3- and then 1-μm diamond particles. The substrates were cleaned in acetone subjected to ultrasonic activation.

The specimens were coated with PMMA within a few hours of polishing. The PMMA resist used for coating is a two-percent solution of PMMA, 950,000 relative molecular weight, with chlorobenzene as the solvent. The PMMA resist was spun on the specimens, at a speed of 3000 RPM for 30 s. The specimens were then baked on a hot plate for 30 minutes at 160°C. This process produces a cured layer of PMMA resist that is approximately 100-nm thick. The application is performed in a class-100 clean room.

The specimens were mounted on a specimen stage in a digitally controlled SEM that was equipped with a Faraday cup and a beam blanker. The SEM was operated with an accelerating voltage of 20 kV and a 50-μm aperture. The working distance was set at 25 mm and the specimen surface was 23 mm from the objective lens. The Faraday cup was inserted into the electron beam, and the beam current i_B was adjusted to a specified value in the range from 10 to 40 pA.

The e-beam in the SEM is computer controlled, and patterns are written in the PMMA resist in accordance with programmed instructions that involve three different software packages. The first is a CAD (computer-aided drafting) program where the length, pitch, and number of lines are

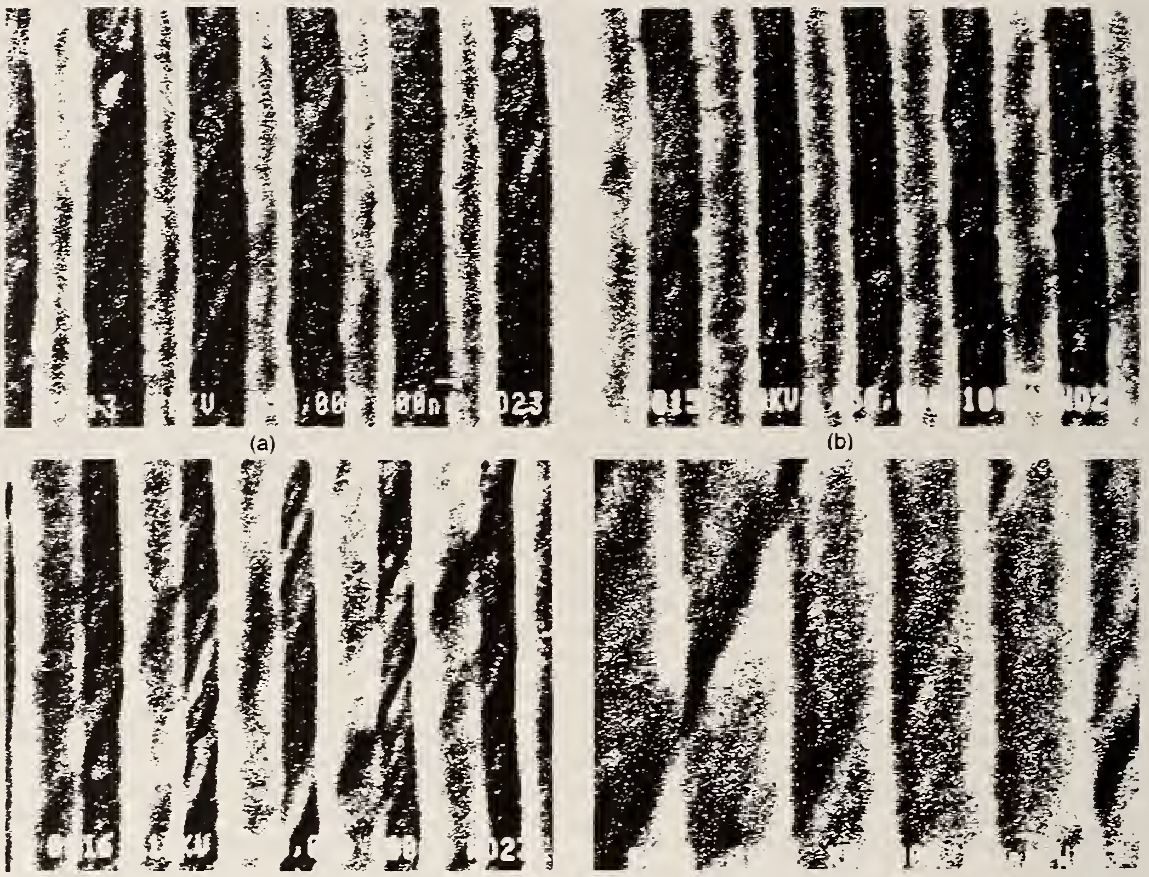
(a) (b) (c) (d)

Fig. 3—Effect of electron exposure on width of trench and ridge (pitch 400 nm, substrate brass)

specified to define a line array. Similarly, for a dot array, the pitch in x and in y and the number of dots are specified.

The second program provides instructions to the SEM for controlling the electron beam in writing the pattern specified in the CAD file. When a line is written, the electron beam is moved from point to point, and the line is produced by many closely spaced points. To write a line with a series of points, the center-to-center distance is about 1/4 the final line width. To properly expose the PMMA, we adjust the line dose and the area dose. The line dose D_L is

$$D_L = i_B t_e / cc \qquad (1)$$

and the area dose D_A is

$$D_A = (i_B t_e)/(cc)\,(p) \qquad (2)$$

where

i_B = beam current
t_e = exposure time per point
cc = center-to-center distance
p = pitch of the line array.

The units commonly used for D_L and D_A are nC/cm and μC/cm^2. We specify i_B, t_e, and cc in this second program, and the pitch p in the CAD program to give the line and area doses that are required for the most suitable exposure of the PMMA resist.

The final program executes the instructions provided in the files of the two previous programs. This program provides digital signals to the scanning coils and the beam blanker to move the beam so as to generate the specified line or dot array.

After the patterns are written, the specimen is developed in a solution consisting of three parts (by volume) of isopropyl alcohol to one part of methyl isobutyl ketone for 40 s. The specimen is immediately rinsed in isopropyl alcohol for 20 s followed by a second rinse in deionized water for 30 s. Next, the specimen is blown dry with a clean gas. The development of the resist is an etching process, and precise control is critical.

Finally, the specimen was coated with a very thin layer (10 to 20 nm) of a gold-palladium alloy by plasma sputtering. This metallic coating is necessary to provide a conductive surface that prevents a surface charge from developing when viewing the specimen in the SEM.

Experiments were conducted to write lines and square arrays of dots with pitches of 400, 200, 100, 75, and 50 nm. Line and area dosage was varied for each pitch to establish writing parameters. Typical results are presented in Figs. 3 through 7.

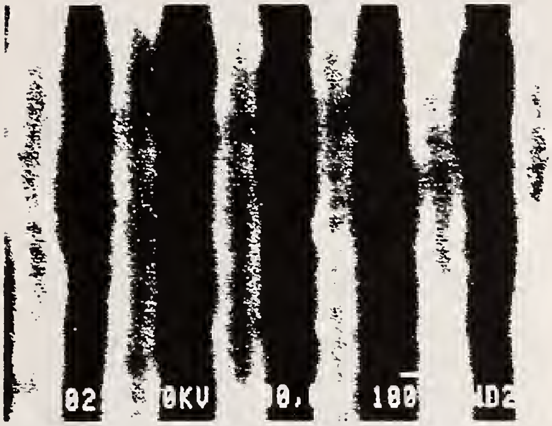

Fig. 4—Demonstration of quality of a line array with a 200-nm pitch

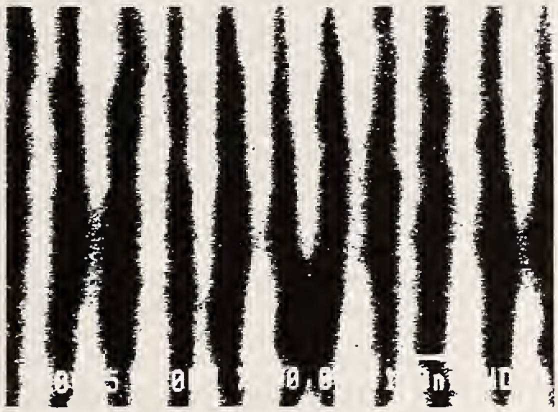

Fig. 5(a)—Lines on 100-nm centers shown at 100,000×

The effect of exposure, measured in terms of line dosage and area dosage, is shown in Figs. 3(a)-3(d) for a line array with a 400-nm pitch. These images were recorded on an SEM at a magnification of 50,000×. The scale bar representing 100 nm is given. In the illustrations, the dark regions represent trenches where the PMMA resist has been etched away, and the light areas show ridges where the resist is intact. The thin dark lines that are inclined to the trenches and ridges are scratches left by polishing the surface of the brass substrate. In Fig. 3(a), with the largest line and area dosage, the trenches are about 225-nm wide, and the ridges are only 175-nm wide. The wandering of the edges separating the trenches and the ridges is due to oscillations in the position of the incident electron beam and the random nature of electron backscattering. As the exposure is decreased, while holding the developing (etching) time constant, the width of the trench decreases. In Fig. 3(b), the trench and ridges are of equal width. In Fig. 3(c), the trench width is only 150 nm and the ridge width is 250 nm. An example of underexposure, in Fig. 3(d), shows that the trenches are not well defined.

The line array shown in Fig. 4, at a magnification of 100,000×, is at a pitch of 200 nm. In this experiment, the line and area dosages were 1.25 *n*C/cm and 62.5 μC/cm^2. The trench width was about 85 nm and the ridge width was 115 nm. The waviness of the edges between the trenches and the ridges is more apparent because the reduced pitch required higher magnification.

The line array shown in Figs. 5(a) and 5(b) is at a pitch of 100 nm. In Fig. 5(a), the lines and the trenches are nearly the same in width. The waviness of the edges becomes more apparent with decreasing width. In Fig. 5(b), we show the same pattern with an exposure near the lower limit for this 100-nm pitch. In this experiment, the trenches are only 25 nm wide. This result indicates the possibility of producing line arrays with frequencies of 20,000 ℓ/mm.

The current limit on the pitch of the line arrays that was achieved in this series of experiments is 75 nm. An inspection of the SEM image recorded at 120,000× presented in Fig. 6 shows that the pitch varies from line to line ranging

Fig. 5(b)—Lower exposure shows trenches 25-nm wide

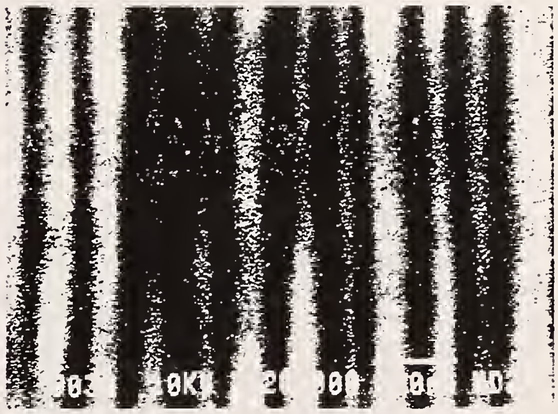

Fig. 6—Line array with a pitch of 75 nm at a magnification of 120,000×

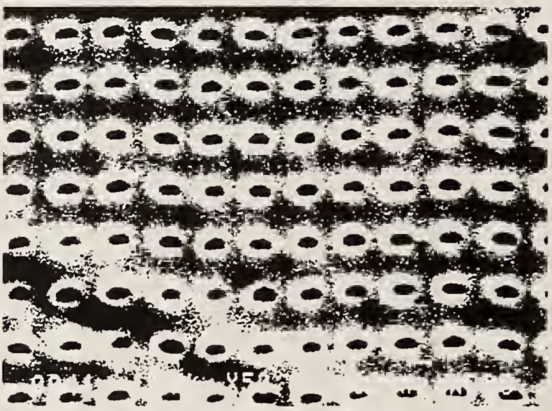

Fig. 7—A dot pattern on 200-nm centers at 50,000×

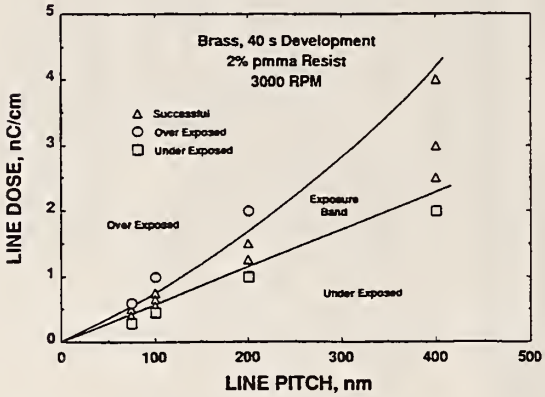

Fig. 8—Line dosage as a function of line pitch

from 55 to 95 nm, although the average pitch over 10 lines is 75 nm. The apparent pitch variation is local and is due to the waviness of the trenches. The electron beam is oscillating with an amplitude of about 20 nm as it moves along from point to point in writing a line.

A dot pattern on 200-nm centers is presented in Fig. 7. The dots are somewhat elongated, with an aspect ratio of about 2 to 1. We believe the elongation is due to astigmatism of the electron beam in this particular experiment, because we have produced much more nearly circular dots in other experiments. Each dot is produced with an exposure time of 1,000 μs and a probe current of 10 pA. The dot patterns have the advantage that they can be produced in much less time per unit area of pattern than the line arrays. Also, the resulting pattern serves as a cross grating which is necessary in two-dimensional moiré.

From these experiments, we have deduced the electron beam line dosage required to write line arrays of various pitches, Fig. 8. For line pitches of 400 nm, the exposure band is very wide, ranging from 2.5 to 4.0 *nC*/cm. Although the ratio of the trench-to-ridge width varies across this band, the line arrays are suitable for moiré applications. However, as the pitch decreases, the exposure band decreases markedly. At pitches of 100 nm, the line dosage must be controlled within a band from 0.55 to 0.75 *nC*/cm. It appears that a good first approximation for line dosage as a function of pitch is

$$D_L = 6.5\,p \tag{3}$$

where D_L is in *nC*/cm and p is in μm.

Moiré Fringe Formation

The line or dot patterns can be interrogated either by line counting that involves a fast-Fourier transform (FFT) of a digital image[14] or by producing scanning moiré fringes.[8, 10] In this paper, we illustrate typical moiré fringe patterns that are produced by the scanning lines in a SEM. The scanning lines in a SEM have a pitch p_r that depends on the magnification and the scan rate selected for observation or photography. The pitch p_r is given by

$$p_r = s/(mM) \tag{4}$$

where

s = characteristic length (about 90 mm) dependent on the SEM
m = number of scan lines in the image
M = magnification

The reference pitch can be varied by adjusting either m or M; however, the variation is not continuous since the choices of m are very limited and the magnification is varied from 10 to 300,000× in discrete steps.

Moiré fringe patterns are observed when

$$p_s = \beta p_r\,(1 + \alpha) \tag{5}$$

where

p_s = pitch of the lines on the specimen
β = Post's multiplication factor[15]
α = mismatch factor ranging from 0 to 0.1

Examples of typical moiré fringe patterns are shown in Fig.10. The fringe pattern in Fig. 10(a) has formed over a 50 × 50 μm square patch of lines on 100-nm centers. The irregularities in this pattern are due to surface imperfections that were frequently encountered on brass surfaces. These pits usually range in size from 1 to 5 μm. The moiré pattern in Fig. 9(b) was formed over a 50-μm square patch of dots arranged on 200-nm centers. The specimen in this case was GFRP, and the ends of the fibers can be seen in the background.

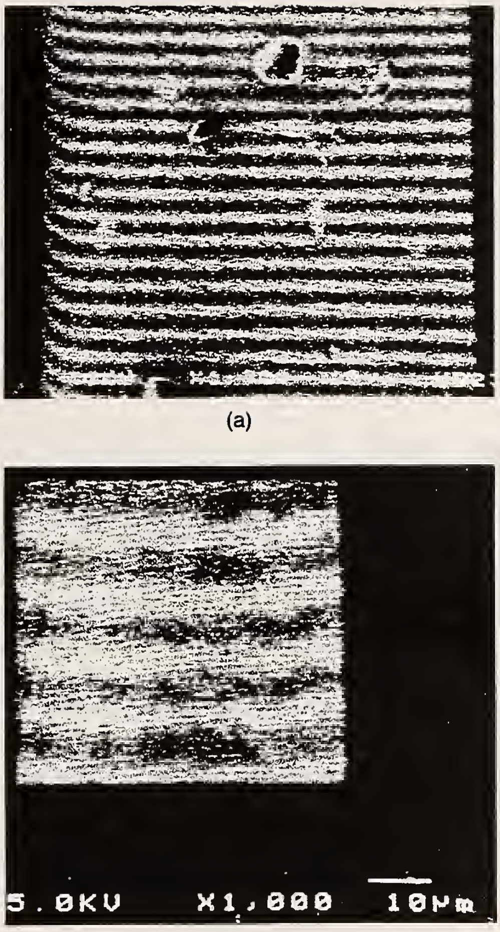

(a)

(b)

Fig. 9—Moiré fringe formation in a SEM: (a) 100-nm lines on brass, (b) 200-nm dot pattern on GFRP

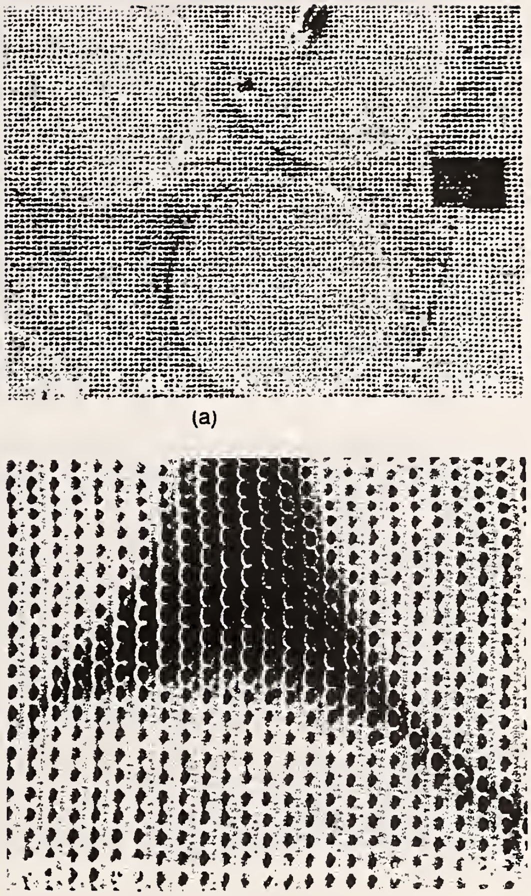

(a)

(b)

Fig. 10—Dot patterns on 200-nm centers on a cross-ply GFRP specimen with 8 μm fibers at 5,500× and 20,000×

Discussion and Conclusions

Electron beam moiré avoids the limits imposed on optical methods of moiré by the wavelength of light. Both line and dot patterns can be written on metallic and composite specimens with spatial frequencies as high as 13,300 ℓ/mm. Moiré fringe patterns can be formed using the scanning lines of an SEM as the reference gratings at magnifications as high as 1,900× with 100-nm pitch line patterns.

The potential applications of e-beam moiré in micromechanics are evident from the line frequencies which can be achieved and the magnifications involved in forming the image of the moiré fringes. To illustrate the micromechanics potential of the method, a dot pattern, on 200-nm centers, is shown in Fig. 10. In Fig. 10(a) at 5500×, the dot pattern covers one complete fiber end, parts of three others, and part of a longitudinal fiber. About 40 rows of dots are written over the end of a fiber 8 μm in diameter. The triangular matrix region between three fibers is shown in Fig. 10(b) where the dot pattern is represented at a magnification of 20,000×.

A moiré fringe pattern obtained from a 100-nm pitch line array positioned at an interface between a longitudinal ply and a crossply is illustrated in Fig. 12. The specimen in this case was fabricated from a cross-ply glass-fiber-reinforced epoxy 2-mm thick 6-mm wide and 33-mm long. The specimen was loaded in tension within the vacuum chamber of the SEM using a specially adapted tensile loading system.

The fringe pattern in Fig. 11(a) is with a small nominal load and is due to mismatch. The fringe pattern in Fig. 11(b) is due to both mismatch and imposed strain. The fringe distortion was not expected since mismatch fringes are straight. The distortions are due to the small changes in expansion of the glass and the epoxy that occurred between the time of the etching and the time of testing. These local deformations may be produced by either differential expansion of the epoxy due to diffusion or due to temperature.

An inspection of the interface region between the longitudinal and the cross plies shows that the change in the

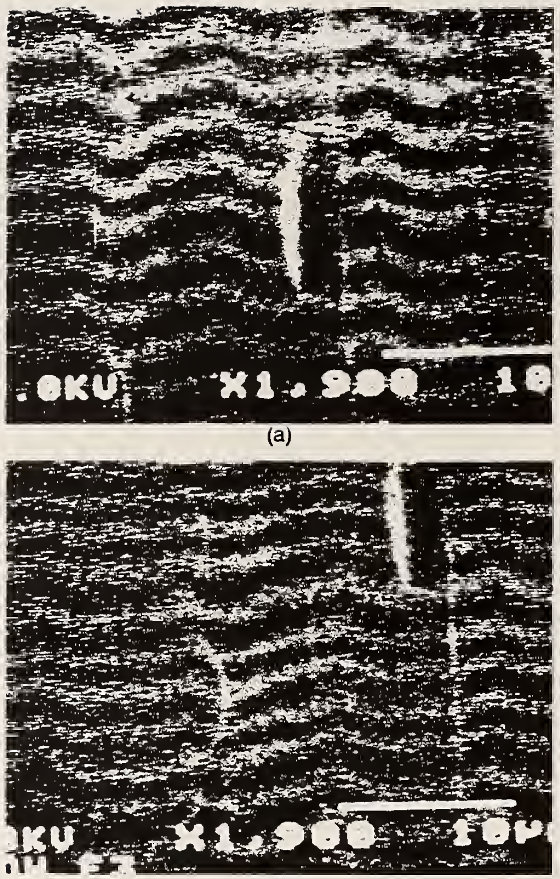

(a)

(b)

Fig. 11—Moiré fringe pattern at an interface between longitudinal and cross plies (100-nm line grating): (a) zero load pattern, (b) pattern at a nominal tensile stress of 146 MPa.

number of fringes over the characteristic dimensions of the fiber diameter (8 µm) is very small. This fact indicates that the localized strain concentrations at the interface are not large. Subsequent experiments have shown that large interface shearing strains occur only after cross-ply cracking develops at higher loads.

Acknowledgments

Thanks are due to R.E. Harris and J. Martinis for the use of the lithographic facility in the Electromagnetic Technology Division at NIST; and to Greg Zimmerli for introducing us to electron beam lithography.

References

1. Weller, R. and Shepard, B.M., "Displacement Measurement by Mechanical Interferometry," Proc. Soc. for Exp. Stress Analysis, **6** *(1), 35-38 (1948).*

2. Parks, V.J., Geometric Moiré, Handbook on Experimental Mechanics, ed. A.S. Kobayashi, Prentice-Hall, Englewood Cliffs, NJ, 282-313 (1987).

3. Theocaris, P.S., Moiré Fringes in Strain Analysis, Pergamon Press, Elmsford, NY (1969).

4. Post, D., "Optical Interference for Deformation Measurements - Classical, Holographic and Moiré Interferometry," Mechanics of Nondestructive Testing, ed. W.W. Stinchcomb, Plenum Press, New York, 1-53 (1980).

5. McDonach, A., McKelvie, J. and Walker, C.A., "Stress Analysis of Fibrous Composites Using Moiré Interferometry," Opt. and Laser Eng., **1***, 85-105 (1980).*

6. Post, D., "Moiré Interferometry: Advances and Applications," EXPERIMENTAL MECHANICS, **31** *(3), 276-280 (1991).*

7. Haller, I., Hatzakis, M. and Srinivasan, R., "High Resolution Positive Resists for Electron-beam Exposure," IBM J. Res. and Dev., **12***, 251 (1968).*

8. Patton, N.E. and Mahoney, M.W., "Creep of Titanium-Silicon Alloys," Met. Trans. A, **7A***, 1685-1692 (1976).*

9. Kishimoto, S., M. Egashira, Shinya, N. and Carolan, R.A., "Local Micro-Deformation Analysis by Means of Microgrid and Electron Beam Moiré Fringe Method," Proc. 6th Int. Conf. on Mech. Behavior of Materials, ed. M. Jono and T. Inoue, **4***, 661-666 (1991).*

10. Kishimoto, S., Egashira, M. and Shinya, "Measurement of Grain Boundary Sliding and Observation of Microgrids for High Temperature Use," J. Soc. for Mat. Sci. Japan (in Japanese), **40** *(452), 637-641 (1991).*

11. Morimoto, Y. and Hayashi, T., "Deformation Measurement During Powder Compaction by a Scanning Moiré Method," EXPERIMENTAL MECHANICS, **24***, 112-116 (1984).*

12. Goldstein, J.I., Newbury, D.E., Echlin, P., Joy, D.C., Fiori, C. and Lifshin, E., Scanning Electron Microscopy and X-Ray Microanalysis, Plenum Press, New York, 19-203 (1981).

13. Everhart, T.E., Herzog, R.F., Chung, M.S. and Devore, W.J., "Electron Energy Dissipation Measurements in Solids," 6th Int. Cong. on X-Ray Optics and Microanalysis, 81-86 (1971).

14. Santo, M., Dally, J.W. and Read, D.T., "A Grid-Moiré Hybrid Method for Measuring Strain and Displacement," Optical Engineering, in press.

15. Post, D., "Sharpening and Multiplication of Moiré Fringes," EXPERIMENTAL MECHANICS, **7** *(4), 154-159 (1967).*

A2

Local Strain Measurement by Electron Beam Moiré

by Read and Dally (1993)

EEP-Vol. 4-1, Advances in Electronic Packaging
ASME 1993

LOCAL STRAIN MEASUREMENT BY ELECTRON BEAM MOIRÉ

David T. Read
Materials Reliability Division
National Institute of Standards and Technology
Boulder, Colorado

James W. Dally
Department of Mechanical Engineering
University of Maryland
College Park, Maryland

ABSTRACT

Moiré fringe patterns can occur when high-frequency line arrays are observed in the scanning electron microscope. We have applied this phenomenon to local deformation measurement in a glass-fiber-reinforced plastic and in a plated-through-hole. In the GFRP, local strain measurements were made by interpreting the moiré fringe patterns over gage lengths from 10 to 30 µm at a 0-90 ply interface during tensile testing. Load shedding by the transverse ply was evident from the fringe patterns. On a cross section of a plated-through-hole, inhomogenous strains were observed.

INTRODUCTION

Since its introduction by Weller and Shepard [1] in 1948, the moiré method of displacement and strain analysis has been improved by introducing new techniques and new technologies. The development of geometric or mechanical moiré methods, which occurred during the period from 1948 to 1970, has recently been reviewed by Parks [2] and has been described in detail by Theocaris [3]. Since 1980, most of the development has involved moiré interferometry where diffraction gratings are produced by interference of two plane beams from a coherent light source [4,5]. Moiré interferometry represented a major advance because the frequency of the specimen grating was increased by a factor of about 50 to 4 000 lines/mm. This increase improved the sensitivity of the method and extended the applicability of the moiré method to a wider range of problems [6].

D. Post and colleagues presented moiré interferometry data showing the shear-strain differences among 0° plies, 90° plies, and resin-rich regions between plies [7]. They have applied well-developed techniques to a series of issues in the behavior of composite materials and interfaces [8-10]. In particular, the stiffness difference between fiber and matrix produced zig-zag fringes [8].

Since further increases in the frequency of the specimen gratings are limited by the wavelength of light, it is necessary to employ a different form of energy to achieve line arrays with frequencies of 10 000 lines/mm or higher. Our colleagues in high resolution lithography have already solved this problem by writing very fine lines using an electron beam [11]. Paton used lines written with an electron beam to study slip at grain boundaries [12]. Kishimoto et al. [13,14] were the first to introduce e-beam moiré and to demonstrate its application to study microdeformation. In these studies, relatively coarse gratings, with pitches between 3.7 and 7.1 µm, were used. The moiré fringe patterns were produced by interfering the lines in the array with the scanning lines in a conventional scanning electron microscope (SEM). This method of moiré fringe formation is similar to the video scanning moiré techniques introduced by Morimoto et al. [15] in 1984.

In this paper we first demonstrate the use of electron beam lithograhy to to produce very high frequency line and dot gratings (10 000 lines/mm) which are suitable for moiré applications. The ability to write gratingss on both homogenous and heterogenous materials such as glass fiber-reinforced plastics is demonstrated. The application of e-beam moiré at high magnification (1 900X), which is required in micromechanics, is emphasized

We then describe the use of electron-beam moirwé to study displacements and strains in a tensile specimen fabricated from a $[0_2/90]_s$ glass fiber reinforced epoxy, and discuss

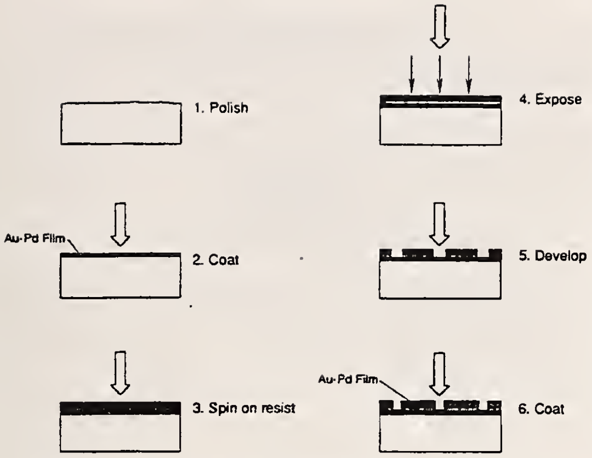

Figure 1. Electron-beam lithography steps to produce line gratings for electron beam moiré.

progress on applying this technique to the study of thermomechanical displacements in the plated-through-hole.

GRATING PREPARATION

A series of experiments were performed to determine the parameters to employ in writing line and dot arrays and the minimum pitch which could be achieved. Aluminum, brass, and GFRP were used as the substrate materials. The metallic substrates were disks 12.7 mm in diameter and 1 to 2 mm thick. The GFRP was a strip 6 x 32 mm by 2 mm thick. Figure 1 summarizes the grating preparation.

The surfaces of the specimens were ground smooth and flat using a series of water-lubricated abrasive-coated papers ending with 5 µm grit. The final polish was achieved by finishing with 3 and then 1 µm diamond particles. The substrates were cleaned in acetone subjected to ultrasonic activation. Non-conductive specimens were coated with a conductive layer.

The specimens were coated with PMMA within a few hours of polishing. The PMMA resist used for coating is a 2% solution of PMMA, 950 000 relative molecular weight, with chlorobenzene as the solvent. The PMMA resist was spun on the specimens, at a speed of 3000 RPM for 30 s. The specimens were then baked on a hot plate for 30 minutes at 160°C. This process produces a cured layer of PMMA resist that is approximately 100 nm thick. The application is performed in a class-100 clean room.

The specimens were mounted on a specimen stage with a built-in glass-on-carbon resolution standard, in a digitally controlled SEM that was equipped with a

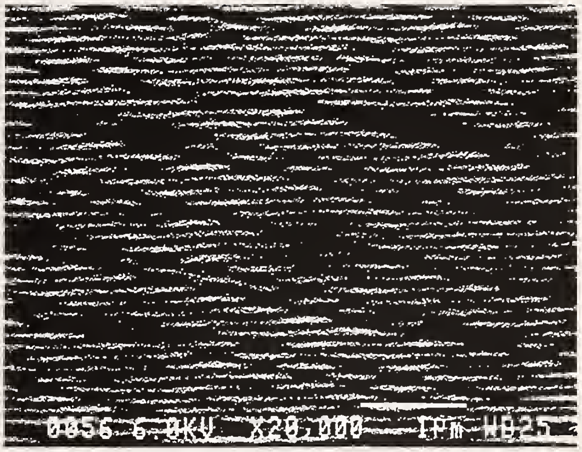

Figure 2. An SEM microphotograph of a line grating with a pitch of 10 000 lines/mm on GFRP.

Faraday cup and a beam blanker. The SEM was operated with an accelerating voltage of 20 kV and a 50 µm aperture. The working distance was set at 25 mm and the specimen surface was 23 mm from the objective lens. The Faraday cup was inserted into the electron beam, and the beam current was adjusted to a specified value in the range from 10 to 40 pA. The e-beam in the SEM is computer conrolled; gratings are written in the PMMA resist point-by-point. To write a line with a series of points, the center-to-center distance is about 1/4 the final line width. To properly expose the PMMA, we adjust the line dose and the area dose. The line dose is about 0.8 nC/cm for lines with a pitch of 100 nm, and increases nearly linearly with the pitch.

After the gratings are written, the specimen is developed in a solution consisting of three parts (by volume) of isopropyl alcohol to one part of methyl isobutyl ketone for 40 s. The specimen is immediately rinsed in isopropyl alcohol for 20 s followed by a second rinse in deionized water for 30 s. Next, the specimen is blown dry with a clean gas. The development of the resist is an etching process; precise control is critical.

Finally, the specimen is coatied with a very thin layer (10 to 20 nm) of a gold-palladium alloy by plasma sputtering. This metallic coating is necessary to prevent surface charge accumulation when viewing the specimen in the SEM.

Figure 2 shows a line grating from a GRFP specimen that is discussed further below. This grating, shown at a magnification of 20 000X, has a pitch of 100 nm. The thin dark lines correspond to trenches in the PMMA resist formed by etching the regions struck by the electron beam. The wider light lines are ridges in the resist. The dark lines on a diagonal are due to a malfunction in the e-beam control during the exposure of the resist. Fortunately, the primary lines, which are horizontal and on 100 nm centers, are

Figure 3. An SEM microphotograph of a GFRP specimen with a 200-nm-pitch dot grating, shown at 50 000X.

Figure 4. Line gratings on the tensile specimen. The different shades indicate different line densities and exposures.

dominant since they cover about 85% of the area. Although the grating was flawed, it produced well-defined moiré fringes with good contrast. Figure 3 shows a dot grating with a pitch of 200 nm.

Figure 5a. Tensile specimen, after failure. The black drops are conductive paste, which electrically grounds the specimen surface to the grips.

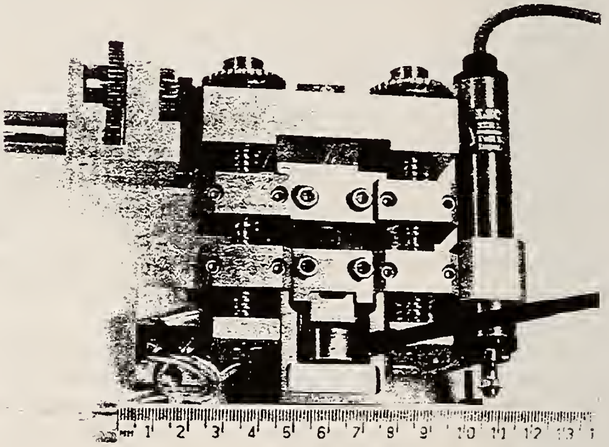

Figure 5b. Tensile testing stage for the scanning electron microscope.

STRAIN FIELD DEVELOPMENT IN GFRP UNDER TENSION

Specimen Preparation

The composite material investigated is a glass fiber reinforced epoxy known as 52/3501-6. The panels were laid up by hand and cured in an autoclave. The lay-up included 48 layers of prepreg oriented $[0_2/90]_s$. The lay-up was symmetrical, with a surface to midplane sequence of 0/0/90/0/0/90/ ... 0/0/90|. This composite was

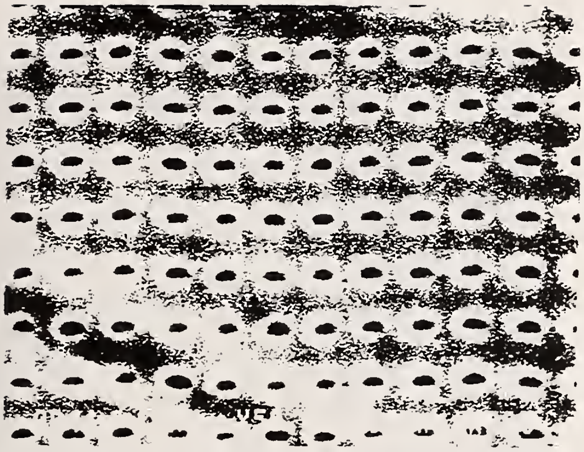

Figure 3. An SEM microphotograph of a GFRP specimen with a 200-nm-pitch dot grating, shown at 50 000X.

Figure 4. Line gratings on the tensile specimen. The different shades indicate different line densities and exposures.

dominant since they cover about 85% of the area. Although the grating was flawed, it produced well-defined moiré fringes with good contrast. Figure 3 shows a dot grating with a pitch of 200 nm.

Figure 5a. Tensile specimen, after failure. The black drops are conductive paste, which electrically grounds the specimen surface to the grips.

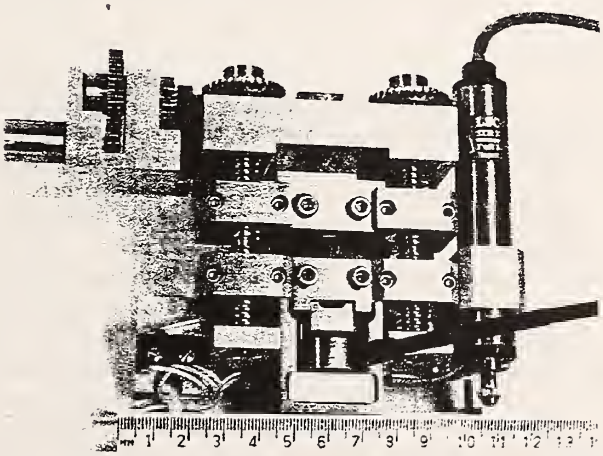

Figure 5b. Tensile testing stage for the scanning electron microscope.

STRAIN FIELD DEVELOPMENT IN GFRP UNDER TENSION

Specimen Preparation

The composite material investigated is a glass fiber reinforced epoxy known as 52/3501-6. The panels were laid up by hand and cured in an autoclave. The lay-up included 48 layers of prepreg oriented $[0_2/90]_s$. The lay-up was symmetrical, with a surface to midplane sequence of 0/0/90/0/0/90/ ... 0/0/90|. This composite was

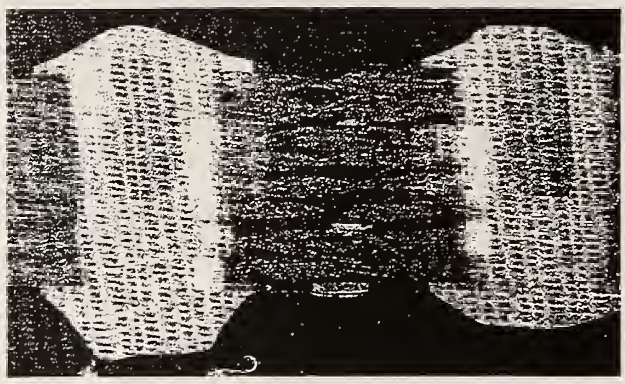

Figure 8. Cross-section of a plated-through-hole showing gratings as square patterns.

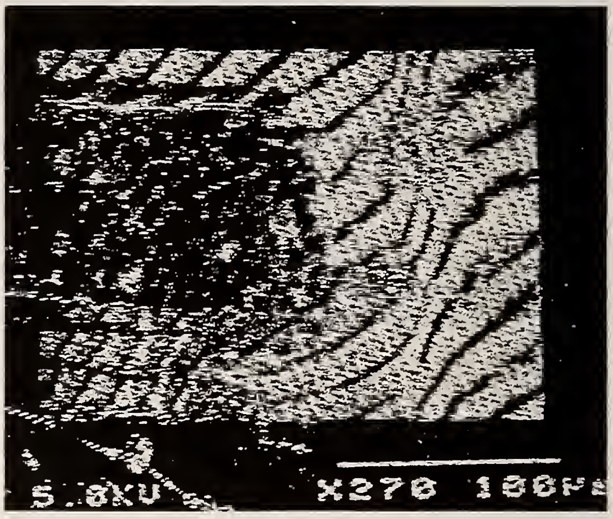

Figure 9. Moiré fringes on a plated-through-hole cross section at the interface between figerglass, copper, and solder. Note the bent fringes.

that the strain in the 0° ply has increased, and significant shearing strain has occurred over the resin-rich area at the interface. Failures in the 90° ply above and below the grating area were visible in the SEM. This cross ply cracking markedly degraded the contribution of the 90° ply to the tensile stiffness of the composite.

Analysis of Fig. 7, obtained at an applied stress of 524 MPa, gives the following results. The strains in the 90° ply are 0.9×10^{-3}, although the global strain on the specimen, as estimated from the global Young's modulus, is 14×10^{-3}. Clearly, the cross ply cracking has nearly eliminated the load-carrying capability of the 90° plies. The strain in the first fiber of the 0° ply varies over its length in the field of view. Over the bottom portion of this fiber, the strain is 13.5×10^{-3}. Over the top portion of this fiber, the strain is only 8.65×10^{-3}. The average strain over both the top and the bottom portions is 10.9×10^{-3}. The damage in the cross plies and other fractures must have affected the local region being analyzed.

The effect of damage is most evident at the interface, where moiré fringes that are inclined 17° to the vertical indicate significant shear in the resin-rich region between the 0° and 90° plies.

Normal and shear strains were determined from observed displacement gradients, using analysis procedures familiar from geometric optical moiré. Shear strains were approximated by assuming that the x-direction displacements were insignificant. We determined γ_{xy} by noting a shift of 5 fringe orders across the interface as we move from the lower fiber end in the 90° ply to the first longitudinal fiber in the 0° ply. The thickness of the resin-rich area at the lower fiber is 5.29 μm. The resulting engineering shear strain $\gamma_{xy} = 9.3\%$. This is a very large shearing strain that is supported by the matrix material, preventing delamination.

A final feature, evident in Fig. 7, is a crack in one of the longitudinal fibers. This fiber was not perfectly straight in the lay-up and in polishing we have formed a dagger-shaped section. We observe a discontinuity of the moiré fringe to the left of crack, indicating another localized shear strain. Measurements of Δv and Δx indicate that γ_{xy} in the matrix material just above and to the left of the crack was about 4.5%.

THERMOMECHANICAL STRAINS IN A PLATED-THROUGH-HOLE

A plated-through hole in a printed wiring board is a composite structure that includes glass-fiber-reinforced plastic, copper, and solder. The difference between the out-of-plane thermal expansion rate of the board and those of copper and solder is well known to be large, and consequently to be the driving force in potential failure mechanisms which can be a problem if the manufacturing process is not carefully controlled.

The plated-through-hole specimen was cut from a large circuit board from a commercial electronic product. A cross-section was potted in epoxy and ground and polished to expose cross-sections of plated-through-holes. Gratings were applied by electron-beam lithography as described above. For examining thermally-induced displacements, a commercially-supplied heating stage for the SEM was used. A thermocouple was placed on the top surface of the specimen.

Quantitative use of electron-beam moiré in thermomechanical experiments is complicated by electric and magnetic deflection of the electron beam by the heater in the stage, and by small progressive displacements of the specimen caused by thermal expansion of the stage. Figure 8 shows a cross section of a plated-through-hole in a printed wiring board with two internal copper layers in addition to the front and back surface layers. The squares on this micrograph are line gratings produced by electron beam lithography. A variety of grating pitches wre used. The observations reported below come from a grating with a pitch of 1 μm. Figure 9 shows electron beam moiré patterns on a plated-through-hole at 144° C. This image shows, left-to-right, fiberglass printed-circuit-board (PCB), copper, and solder. The large thermal expansion of the PCB creates a shear deformation, indicated by the slanting moiré fringes. Note the concentrated deformation at the copper-solder interface. Engineering (angle) shear strains of over 1 percent have been observed in the neighborhood of the copper-solder interface. Fringes at angles corresponding to even higher shear strains have been seen, however the interpretation is difficult. The fringe mismatches may be indicating local decohesion between the solder and the copper. By contrast, the fringes in the copper and the GFRP seem to be the same after heating as before.

SUMMARY CONCLUSIONS

(1) Line gratings with a pitch of 100 nm can be fabricated by electron beam lithography with sufficient contrast and efficiency to form electron beam moiré patterns at a magnification of 1900 X, where the raster scan of the scanning electron microscope provides a virtual reference grating with a similar pitch with 500 lines across the field of view.

(2) These moiré patterns can be formed on unstressed specimens and also on tensile specimens during testing, and on specimens heated up to 150°C. Local strains over fields tens of μm can be evaluated with a strain resolution of a few parts in 10^{-4}.

(3) During a tensile test of a glass-fiber-reinforced plastic composite several interesting phenomena were observed:

a) Before failure of the 90° ply, we measured a local modulus E_1 = 36 GPa over a gage length of about 25 μm.

b) When the 90° ply failed by transverse cracking, its load-carrying capability effectively vanished. Failure of the 90° ply produced shearing strains in the resin-rich area between the 0° and 90° plies.

c) After failure of the 90° ply, the strain increments at different locations were not proportional to the increments of the average stress. The increasing numbers of cracks in the 90° plies and in the longitudinal fibers produced a new strain distribution.

(4) The electron beam moiré technique can be applied to theromechanical stressing of plated-through-holes. It has revealed high, irreversible shear strains in the solder near the copper plating.

ACKNOWLEDGMENTS

The preparation of plated-through-hole specimens by Elizabeth Drexler is appreciated.

REFERENCES

1. Weller, R. and Shepard, B.M., "Dislacement Measurement by Mechanical Interferometry," Proc. Society for Experimental Stress Analysis, Vol. 6, No. 1, pp. 35-38, 1948.

2. Parks, V.J., Geometric Moiré, Handbook on Experimental Mechanics, Ed. A.S. Kobayashi, Prentice-Hall, Englewood Cliffs, N.J., pp. 282-313, 1987.

3. Theocaris, P.S., Moiré Fringes in Strain Analysis, Pergamon Press, Elmsford, N.Y., 1969.

4. Post, D., "Optical Interference for Deformation Measurements -Classical, Holographic and Moiré Interferometry," Mechanics of Nondestructive Testing, Ed. W.W. Stinchcomb, Plenum Press, New York, pp. 1-53, 1980.

5. McDonach, A., McKelvie, J., and Walker, C.A., "Stress Analysis of Fibrous Composites Using Moiré Interferometry," Optics and Laser Eng., Vol. 1, pp. 85-105, 1980.

6. Post, D., "Moiré Interferometry: Advances and Applications," Experimental Mechanics, Vol. 31, No. 3, pp. 276-280, 1991.

7. Post, D., Dai, F. L., Guo, Y., and Ifju, P., "Interlaminar shear moduli of cross-ply laminates: An experimental analysis," Journal of Composite Materials 23 (3), 1989, 264-279.

8. Post, D., Czarnek, R., Joh, D., Jo, J., and Guo, Y., "Experimental Study of Metal-Matrix Composite," Experimental Mechanics 27 (2), June, 1987, 190-194.

9. Post, D., Czarnek, R., and Joh, D., "Shear Strains in a Graphite/PEEK Beam by Moiré Interferometry," Experimental Mechanics 27 (3), September, 1987, 246-249.

10. Post, D. and Wood, J. D., "Determination of Thermal Strains by Moiré Interferometry," Experimental Mechanics 29 (3), September, 1989, 318-322.

11. Haller, I., Hatzakis, M. and Srinivasan, R., "High Resolution Positive Resists for Electron-beam Exposure," IBM Journal Research and Development, Vol. 12, pp. 251, 1968.

12. Paton, N.E. and Mahoney, M.W., "Creep of Titanium-Silicon Alloys," Metallurgical Transactions A, Vol. 7A, pp. 1685-1692, 1976.

13. Kishimoto, S., M. Egashira, Shinya, N. and Carolan, R.A., "Local Micro-Deformation Analysis by Means of Microgrid and Electron Beam Moiré Fringe Method," Proceedings of the Sixth International Conference on Mechanical Behavior of Materials, M. Jono and T. Inoue, eds., Kyoto, Japan, Vol. 4, pp. 661-666, 1991.

14. Kishimoto, S., Egashira, M. and Shinya, "Measurement of Grain Boundary Sliding and Observation of Microgrids for High Temperature Use," Journal of the Society for Materials Science Japan, Vol. 40, No. 452, pp. 637-641, 1991 (in Japanese).

15. Morimoto, Y. and Hayashi, T., "Deformation Measurement During Powder Compaction by a Scanning Moiré Method," Experimental Mechanics, Vol. 24, pp. 112-116, 1984.

A3

Electron Beam Moiré Study of Fracture of a Glass Fiber Reinforced Plastic Composite

by Read and Dally (1994)

D. T. Read
Materials Reliability Division,
National Institute of Standards
and Technology,
Boulder, CO 80303

J. W. Dally
Mechanical Engineering Department,
University of Maryland,
College Park, MD 20742

Electron Beam Moiré Study of Fracture of a Glass Fiber Reinforced Plastic Composite

Using the method of electron beam moiré, a small region at an interface of a $[O_2/90]_s$ *glass fiber reinforced plastic composite has been examined during tensile testing. The tensile test was conducted inside a scanning electron microscope, with a high spatial frequency line grating (10,000 lines/mm) at the interface between a longitudinal ply and a transverse ply. During the test, this region was observed at a magnification of 1900×. Local strain measurements were made by interpreting the moiré fringe patterns over gage lengths that varied from 10 to 30 μm. The magnitude and distribution of the local strains depended on the damage that occurred with monotonically increasing load. Load shedding by the transverse ply was evident from the fringe patterns. Extremely high local strains were observed: longitudinal fiber strains up to three percent, normal strains up to three percent, and shear strains up to 40 percent in the epoxy matrix.*

Introduction

Glass fiber reinforced plastic fabricated from several layers or plies is classified as a laminated composite. Although each layer is orthotropic, and the layers may have different orientations, the laminate acts as a single body with a global stiffness that is related to the stiffness and orientation of the individual plies (Halpin, 1984). In a structural analysis of a laminated composite, planes through a typical cross-section are assumed to remain plane after deformations due to tensile or bending loads (Tsai and Hahn, 1981, and Vinson and Sierakowski, 1986). Stresses vary from ply to ply because of changing elastic constants, but the displacements are continuous across the interfaces. Experiments with tension members, beams, plates, and shells (Halpin, 1984) confirm that the results of analysis using laminate theory are not always adequate, and more involved micromechanics theories (Chamis, 1974) are necessary to predict the loss of stiffness and strength. Here we report experimental results showing some deviations from the plane sections remain plane assumption of the simple laminate theory even prior to extensive ply damage. The need for micromechanics theory when damage occurs is clearly established.

Electron beam (e-beam) moiré (Kishimoto et al., 1991; Dally and Read, 1992) was used to study displacement and strains in a tensile specimen fabricated from a $[O_2/90]_s$ glass fiber reinforced epoxy. Displacement and strain were measured on a microscale during four phases of loading:

(1) prior to cross ply cracking,
(2) after cross ply cracking,
(3) after extensive damage, but before delamination, and
(4) after delamination, prior to rupture.

The analysis was performed with a high-frequency line grating (10,000 lines/mm) that was written with an e-beam over an area 50 × 80 μm. The patch of grating was positioned at an interface between a cross ply and a longitudinal ply. The measurement field included three rows of fibers associated with the cross ply, the resin-rich interface, and several fibers in the longitudinal ply.

Background. Some experimental studies of the deformation and failure of composite materials have utilized detailed observations of the behavior of specimens under load. To cite an outstanding example, D. Post and colleagues presented moiré interferometry data showing the shear strain differences among 0 deg plies, 90 deg plies, and resin-rich regions between plies (Post et al., 1989). They have applied well-developed techniques to a series of issues in the behavior of composite materials and interfaces (Post et al., 1987a, Post et al., 1987b, Post and Wood, 1989). In particular, the stiffness difference between fiber and matrix-produced zig-zag fringes (Post et al., 1987a).

High-magnification observation of fracture surfaces was used by Bandyopadhyay et al. (1989) to support their explanation of the difference in fracture toughness between two types of carbon fiber composites. The techniques of Raman spectroscopy (Galiotis et al., 1988) and of speckle interferometry (Anastasi et al., 1987) have also been used to map stresses and deformations in composites at lower spatial resolution.

Detailed theoretical models of the micromechanical behavior

Contributed by the Applied Mechanics Division of THE AMERICAN SOCIETY OF MECHANICAL ENGINEERS for publication in the ASME JOURNAL OF APPLIED MECHANICS.

Discussion on this paper should be addressed to the Technical Editor, Professor Lewis T. Wheeler, Department of Mechanical Engineering, University of Houston, Houston, TX 77204-4792, and will be accepted until four months after final publication of the paper itself in the ASME JOURNAL OF APPLIED MECHANICS.

Manuscript received by the ASME Applied Mechanics Division, Oct. 1, 1992; final revision, Feb. 23, 1993. Associate Technical Editor: W. N. Sharpe, Jr.

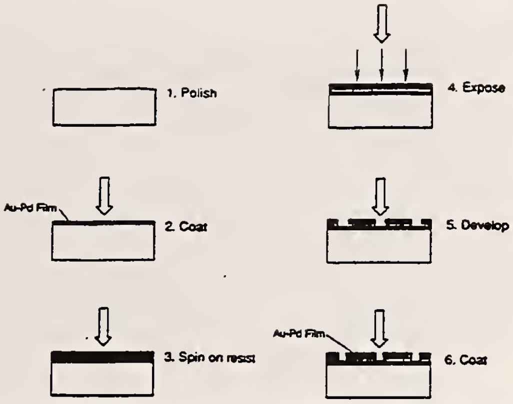

Fig. 1 Electron-beam lithography procedure to produce line gratings for electron beam moiré on the GFRP tensile specimen

of composites have been formulated (Lee et al., 1989), but their verification has relied on macroscopic observations. It is well recognized that demonstration of the macroscopic usefulness of such models does not constitute proof of their micromechanical assumptions.

e-Beam Moiré. e-Beam moiré is similar to optical moiré except that an electron beam is used to produce the line gratings and a scanning electron beam is then employed to generate the moiré fringe pattern. The technique for producing the line grating is shown in Fig. 1. We first prepared the surface of the specimen by grinding it smooth and flat with a series of water-lubricated abrasive papers ending with 5 μm grit. The final polish was achieved by finishing with 3 and then 1 μm diamond particles. The second step was the application of a very thin (10 to 20 nm) gold palladium coating by plasma sputtering. This metallic coating is necessary to render the specimen surface conductive, to prevent a surface charge from developing on the glass fiber reinforced plastic specimen under the electron beam.

The specimens were then coated with polymethylmethacrylate (PMMA) which serves as an electron beam resist. The PMMA solution used for coating was two percent PMMA, molecular weight of 950,000, with chlorobenzene as the solvent. The PMMA resist was spun on the specimens, at a speed of 3000 RPM for 30 seconds. The specimens were then baked on a hot plate for 30 minutes at 160°C. This process produces a cured layer of PMMA resist that is approximately 100 nm thick.

The specimen was mounted on a specimen stage in a digitally controlled scanning electron microscope equipped with a Faraday cup and a beam blanker. The scanning electronic microscope was operated with an accelerating voltage of 20 kV and a 50 μm aperture. The probe current was adjusted to 10 pA, which produces a focussed beam of electrons 10 to 15 nm in diameter. The e-beam in the scanning electronic microscope was computer controlled and patterns were written in the PMMA resist with programmed instructions. These instructions defined both the geometry of the pattern and the electron dosage.

After the patterns were written, the specimen was developed in a solution consisting of three parts (by volume) of isopropyl alcohol to one part of methyl isobutyl ketone for 40 s. The specimen was immediately rinsed in isopropyl alcohol for 20 s followed by a second rinse in deionized water for 30 s. The development of the resist is an etching process; precise control of the development is critical. Finally, the specimen was coated again with a very thin layer (10 to 20 nm) of a gold palladium alloy to provide a conductive surface on top of the PMMA.

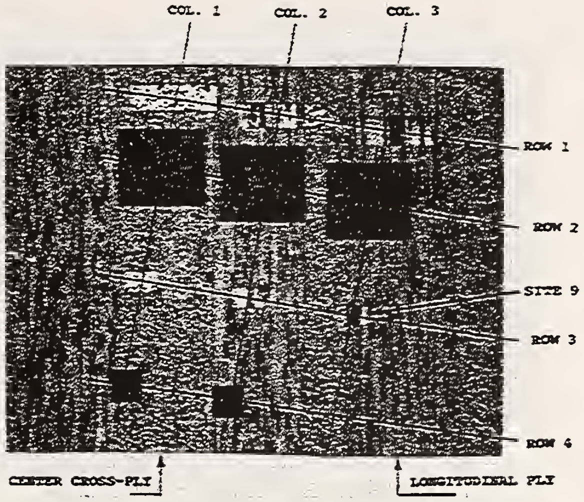

Fig. 2 Line and dot gratings on the tensile specimen

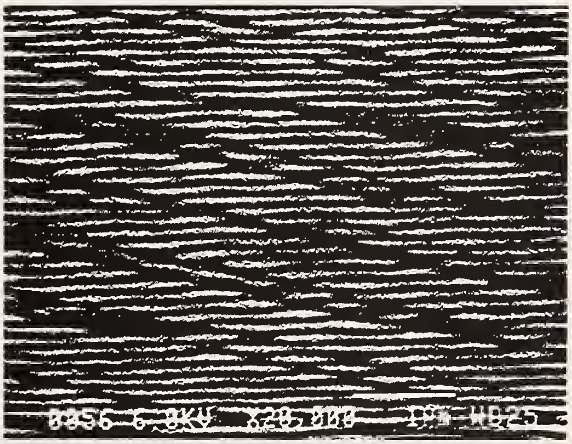

Fig. 3 An SEM micrograph of the moiré grating used in this study with pitch p_s = 100 nm

Twelve different patterns were written on the specimen as illustrated in Fig. 2. The top three patterns, along row 1, are lines 250 μm long on 200 nm centers. The next three patterns, along row 2, are dots placed in a rectangle 240 × 200 μm in size on 200 nm centers. The three patterns on row 3 are lines 80 μm long on 100 nm centers; 500 lines are included in each pattern. Two dot patterns placed in an 80 μm square on 100 nm centers are shown along row 4. The third pattern located at column 3 in row 4 was underexposed. The difference in the shading indicates different line densities and exposures of the patterns.

The pattern at site 9, the third pattern in the third row, was selected for observation in the study. This pattern, having a density of 10,000 lines/mm, was located at an interface between a cross ply and a longitudinal ply. Also, the line array provided 80 or more lines across each of several glass fibers (8 to 10 μm in diameter) which was enough to investigate intraply and intrafiber deformations. Finally, the quality of the line grating was sufficient to produce scanning moiré fringes with good contrast.

A scanning electron microscope micrograph of the moiré grating at site 9 taken at 20,000×, presented in Fig. 3, shows the detail of the line array. The thin dark lines correspond to

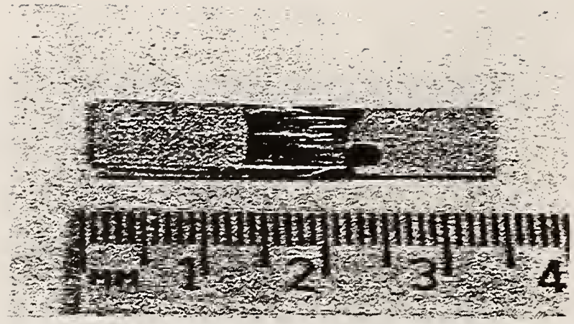

Fig. 4(*a*) Tensile specimen after failure. The black drops are conductive paste, which electrically grounds the specimen surface to the grips.

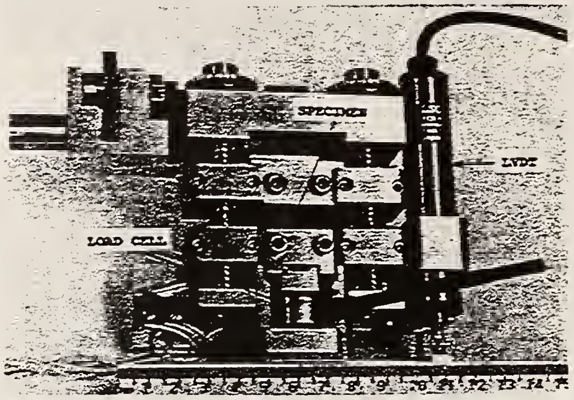

Fig. 4(*b*) Tensile testing stage for the scanning electron microscope

trenches in the PMMA resist formed by etching the regions exposed by the electron beam. The wider light lines are ridges in the resist. The dark lines on a diagonal are due to a malfunction in the e-beam control during the exposure of the resist. Fortunately, the primary lines, which are horizontal and on 100 nm centers, are dominant since they cover about 85 percent of the area. Although the grating was flawed, it produced well-defined moiré fringes with good contrast.

Moiré fringe patterns are formed by scanning the grating lines with the electron beam in a scanning electron microscope. The pitch p_r of the raster scan in the SEM can be controlled by adjusting either the magnification M or the number of scan lines used to form the image. In these experiments the number of scan lines was held constant at 500 and the reference pitch p_r was adjusted with the magnifications setting. At a magnification of 1900×, p_r = 98 nm and is nearly equal to the pitch p_s of the specimen grating. The signal from the secondary electrons which is sensed by a detector in the scanning electron microscope is strongly affected by the difference in frequencies, $f_s - f_r = 1/p_s - 1/p_r$ of the two line arrays. When this frequency difference is small, a pattern of light and dark bands corresponding to moiré fringes is formed. Since these fringes are formed by electrons, the method is not limited by the wavelength of light, and microscale measurements at high magnification are possible.

Specimen and Load Fixture

The composite material investigated is a glass fiber reinforced epoxy known as 52/3501-6. The panels were laid up by hand and cured in an autoclave. The lay-up included 48 layers, of prepreg oriented $[0_2/90]_s$. The lay-up was symmetrical, with a surface to midplane sequence of 0/0/90/0/0/90 . . . . 0/0/90|. The finished panels were 6.22 mm thick, with a void content of less than one percent.

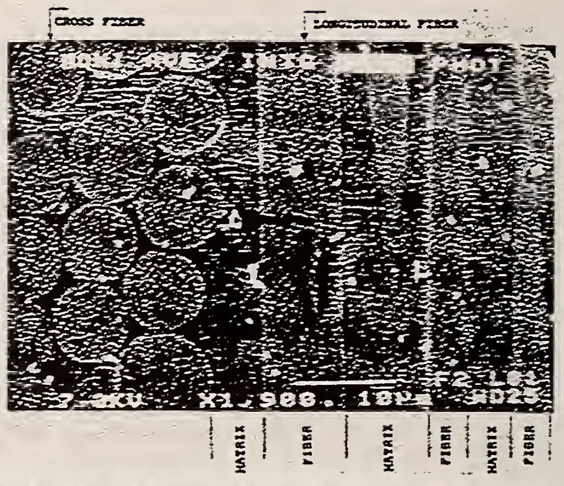

Fig. 5 Moiré fringe pattern at an interface between a longitudinal ply and a cross ply, at initial load

A thin strip 2 mm thick and 33 mm long oriented in the longitudinal 0-deg direction was cut from the composite panel by using an abrasive cutoff wheel flooded with water. The strip was turned on its side to show the cross-section of the laminate and adhesively bonded to a polishing block. The strip was reduced to a thickness of 0.406 mm by sanding and polishing with standard metallographic polishing equipment. The high-density gratings were written on the specimen surface at the sites defined in Fig. 2.

The ends of the specimen were reinforced by bonding aluminum plates to both surfaces as shown in Fig. 4(*a*). The specimen was placed in a small universal testing machine that was designed to fit into the vacuum chamber of a scanning electron microscope. This testing machine, shown in Fig. 4(*b*), employs clamped wedge grips for specimen attachment. Both spur and worm gears are used to turn a pair of lead screws that drive both loading platens at equal speeds. The applied load and platen displacement were measured with a load cell and a LVDT, respectively.

Strain Field Development With Load

Before Cross Ply Cracking. The glass fiber reinforced plastic tensile specimen was mounted on a scanning electron microscope loading machine, and a small initial load of 75 N was applied. The moiré pattern at site 9 was brought into focus at a magnification of 1900×. At this magnification, the pitch of the specimen gratings p_s and the pitch of the scanning electron beam p_r, which serves as the reference grating, were nearly equal. The electron beam raster lines and the specimen grating lines were aligned. The small difference between p_r and p_s produced the mismatch fringes presented in Fig. 5. This figure shows the interface between a 90-deg or cross ply and a 0-deg or longitudinal ply. The three columns of circles are fiber ends in the 90-deg ply that range in diameter from 8 to 10 μm. The resin-rich area at the interface varies in thickness from 3.5 to 5.3 μm. Portions of five different fibers and two resin regions from the 0-deg ply can be identified in Fig. 5.

The next moiré fringe pattern, presented in Fig. 6, corresponds to a nominal tensile stress of 347 MPa. The fringes are continuous across the interface, indicating that the deformations are continuous from the 90-deg to the 0-deg ply. The continuity of the displacements across the interface is consistent

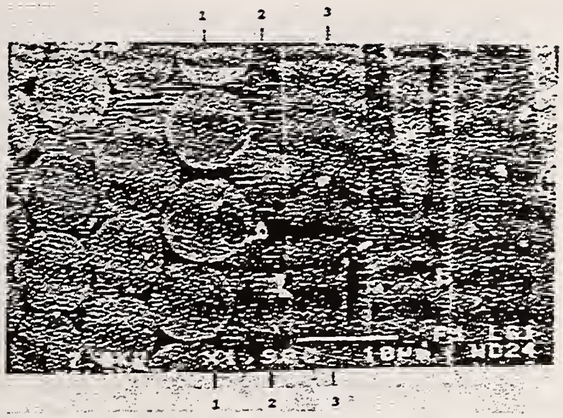

Fig. 6 Moiré fringe pattern prior to cross-ply cracking, at a stress of 347 MPa

Table 1 **Strain distribution across an interface in a $0_2/90$ glass fiber reinforced plastic composite prior to 90-deg ply failure**

σ = 347 MPa

Ply	Strain ϵ_y
90 deg	8.6×10^{-3}
Interface	9.5×10^{-3}
0 deg	10.1×10^{-3}

with elementary laminate theory. However, the gradient dN/dy of the fringe field differs among the 90-deg ply, the interface, and the 0-deg ply, indicating a strain gradient $d\epsilon_y/dx$ across this interface. This strain gradient is not consistent with the plane section assumption of elementary laminate theory.

The strain at any location in the field is given by

$$\epsilon_y = \frac{v}{L} = \frac{\Delta N p_r}{L} \qquad (1)$$

where v is the displacement along the axis of the specimen and normal to the grating lines, p_r = 98.3 nm is the reference pitch at 1900×, and L is a gage length.

The fringe order difference ΔN is

$$\Delta N = N_p - N_0 \qquad (2)$$

where N_p is the number of fringes at load P and N_0 is the number of fringes at initial load.

Combining Eqs. (2) and (3) gives

$$\epsilon_y = (N_p' - N_0')p_r \qquad (3)$$

where N_p' and N_0' are fringe gradients $\Delta N/\Delta y$ at load P and the initial load.

The fringe gradients N_p' and N_0' were determined over a gage length Δy of 25 to 30 μm along the lines 1, 2, and 3 defined in Fig. 6. These lines refer to the first column of fibers in the 90-deg ply, the resin-rich interface, and the first longitudinal fiber in the-deg ply. The results are given in Table 1.

The distance between lines 1 and 3 was 12.9 μm and the strain difference across the interface was 1.5×10^{-3}. Thus, the strain gradient from fiber center line to fiber center line across the interface was $d\epsilon_y/dx = 0.12 \times 10^{-3}$ $(\mu\text{m})^{-1}$.

Next, a local elastic modulus E_l was determined from

$$E_l = \sigma/\epsilon_{\text{ave}} \qquad (4)$$

where the applied tensile stress σ = 347 MPa, and the average strain is

$$\epsilon_{\text{ave}} = (2\epsilon_0 + \epsilon_{90})/3 = 9.6 \times 10^{-3}. \qquad (5)$$

The form of the numerator in Eq. (5) was employed because the laminate was fabricated with two 0-deg plies for every 90-deg ply.

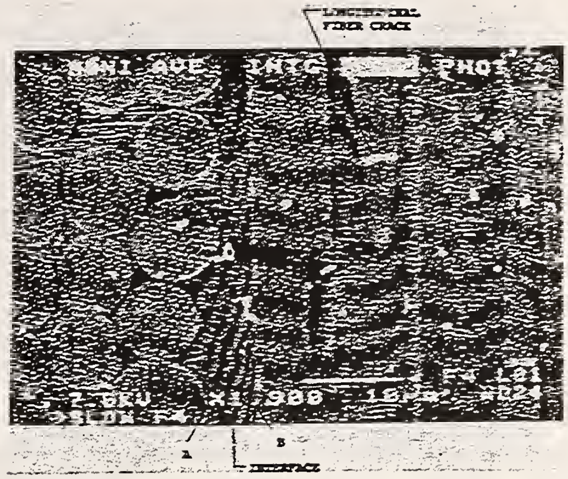

Fig. 7 Moiré fringe pattern after cross-ply cracking, at a stress of 524 MPa

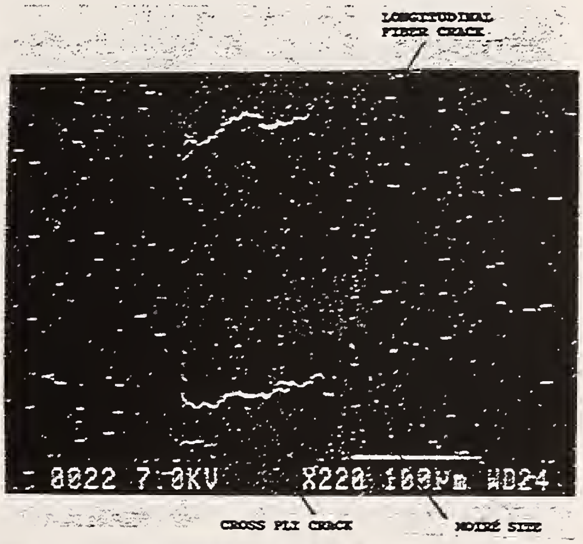

Fig. 8 Cross-ply cracking near the grating and longitudinal fiber cracks over the whole field, at a stress of 700 MPa

The value of the local modulus was 36.1 GPa, which is within five percent of the expected global modulus of 37.9 GPa.

After Cross-Ply Cracking. The moiré fringe pattern presented in Fig. 7 shows a dramatic change in the deformations across the same interface. A cursory inspection of the fringe pattern shows that (a) the strain in the 90-deg ply has decreased, (b) the strain in the 0-deg ply has increased, and (c) significant shearing strain has occurred over the resin-rich area at the interface. Failures in the 90-deg ply above and below the grating area are shown in Fig. 8. This cross-ply cracking markedly degraded the contribution of the 90-deg ply to the tensile stiffness of the composite.

Analysis of Fig. 7 gives the results presented in Table 2. The strains in the 90-deg ply have decreased to about ten percent of their former value, although the global stress on the specimen increased from 347 to 524 MPa. Clearly, the cross-ply cracking has nearly eliminated the load-carrying capability of

Table 2 Strain distribution across an interface in a $0_2/90$ glass fiber reinforced plastic composite after 90-deg ply failure

σ = 524 MPa	
Ply	Strain, ϵ_y
90 deg	8.9×10^{-4}
0 deg	10.9×10^{-3}

Table 3 Strains at several locations near the interface

σ = 700 MPa		
Location	Strain	
	ϵ_y	γ_{xy}
Cross ply	-3.9×10^{-4}	—
Interface	13.5×10^{-3}	0.093
First longitudinal fiber	13.5×10^{-3}	—
Second longitudinal fiber	16.7×10^{-3}	—
Resin between first and second fiber	17.6×10^{-3}	0.014
Resin by crack in dagger fiber	—	0.133

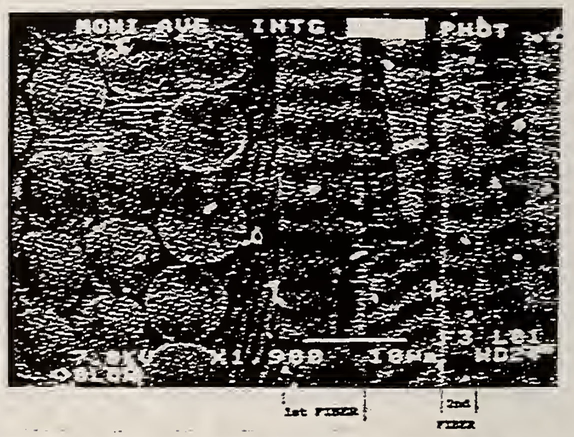

Fig. 9(*a*) Moiré fringe pattern showing development of shear at the interface between the longitudinal ply and the cross ply, at a stress of 700 MPa

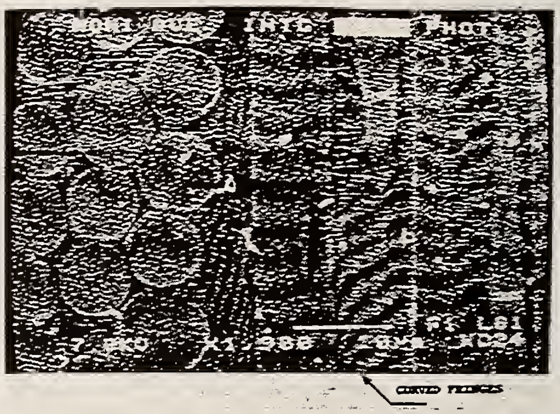

Fig. 9(*b*) Moiré fringe pattern showing extending shear deformation into the longitudinal ply, at a stress of 828 MPa

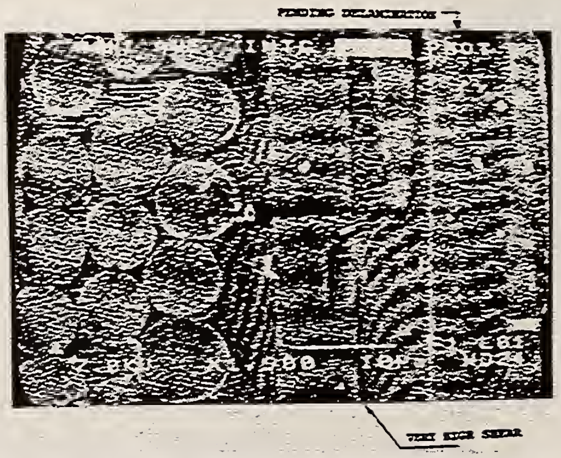

Fig. 9(*c*) Moiré fringe pattern prior to delamination cracking at the location marked, at a stress of 933 MPa

the 90-deg plies. The strain in the first fiber of the 0-deg ply varies over its length in the field of view. Over the bottom portion of this fiber, the strain is 13.5×10^{-3}, but over the top portion of this fiber, the strain is only 8.7×10^{-3}. The average strain over both the top and the bottom portions is 10.9×10^{-3}, which represents an increase of eight percent over strains due to the previous load. Because the globally applied stress was increased by 51 percent, the damage in the cross plies and other fractures of individual fibers has affected the strain distribution in the local region being analyzed.

The effect of damage is most evident at the interface, where moiré fringes that are inclined 17 deg to the vertical indicate significant shear in the resin-rich region between the 0-deg and 90-deg plies. The engineering shear strain is defined as

$$\gamma_{xy}=\left(\frac{\partial v}{\partial x}+\frac{\partial u}{\partial y}\right). \tag{6}$$

If we assume that $\partial u/\partial y$ is small enough relative to $\partial v/\partial x$ to be neglected in the interface region, the engineering shear strain can be approximated as

$$\gamma_{xy}\cong\frac{\Delta v}{\Delta x}. \tag{7}$$

The assumption that $\partial u/\partial y \approx 0$ is reasonable because the longitudinal fibers adjacent to the interface are observed to remain straight under axial tensile stresses. Using Eq. (7), γ_{xy} is determined by noting a shift of five fringe orders across the interface from point A to point B in Fig. 7. This shift due to shear gives $\Delta v = \Delta N p_r = 0.49$ μm. The thickness of the resin-rich area at the lower fiber, corresponding to Δx in Eq. (7), is 5.29 μm. The resulting engineering shear strain $\gamma_{xy} = 9.3$ percent. Clearly, a very large shearing strain is supported by the matrix material, preventing delamination.

A final feature, evident in Fig. 7, is a crack in one of the longitudinal fibers. This fiber was not perfectly planar in the lay-up and appears with a dagger shape after polishing. One observes rotation of the moiré fringes to the left of the crack, indicating another localized shear strain. Measurements of Δv and Δx indicate that γ_{xy} in the matrix material just above and to the left of the crack was about 4.5 percent.

Extension of Shearing into the 0-deg Ply. Moiré patterns in Figs. 9(*a*), 9(*b*), and 9(*c*) show the effect of increasing the tensile stress in the presence of 90-deg ply damage. A cursory inspection of Fig. 9(*a*), which corresponds to σ = 700 MPa, shows the unloading of the 90-deg ply and the extension of the shearing strains from the interface into the resin-rich areas of the 0-deg ply. Measurements were made of the normal strains ϵ_y in the fibers and the shear strains γ_{xy} in the regions of epoxy between the fibers. The results are presented in Table 3.

Table 4 Strains at several locations near the interface

σ = 828 MPa

Location	Strain ϵ_y	γ_{xy}
Cross ply	9.8×10^{-4}	—
Interface	16.0×10^{-3}	0.119
First longitudinal fiber	16.0×10^{-3}	—
Second longitudinal fiber	22.8×10^{-3}	—
Resin between first and second fibers		
adjacent first fiber	—	0.084
center of region	21.4×10^{-3}	0.055
adjacent second fiber	—	0
Resin near crack in dagger-like fiber	—	0.133

Table 5 Strains at several locations near the interface

σ = 993 MPa

Location	Strain ϵ_y	γ_{xy}
Cross ply	3.93×10^{-4}	—
Interface	12.4×10^{-3}	0.072
First longitudinal fiber	12.4×10^{-3}	—
Second longitudinal fiber	25.4×10^{-3}	—
Resin between first and second fibers		
adjacent first fiber	—	0.167
center of region	25.7×10^{-3}	—
adjacent second fiber	—	0

The compressive strain indicated in the cross ply is not real. The magnitude of this strain, $\epsilon_y = 3.9 \times 10^{-4}$, shows the esolution of the method. It is believed that the cross ply is otally unloaded at this load increment. The shear strain at the nterface did not change as the applied tensile stress increased from 524 to 700 MPa. The strain ϵ_y in the first longitudinal iber has increased but not in proportion to the loading. The strains in the second longitudinal fiber and the resin between he first and second fibers are nearly the same, and both are higher than the strain in the first longitudinal fiber.

Shearing strains of 1.36 percent were measured between the first two fibers in the resin region below the dagger-shaped ongitudinal fiber. Shearing strains near the crack in the dagger-shaped fiber were 13.3 percent on the left side and higher than this value on the right side.

The moiré fringe pattern shown in Fig. 9(*b*) corresponds to a tensile stress of 828 MPa. The normal and shear strains at several locations are shown in Table 4.

The strains in the longitudinal fibers and the shear strains at the interface all increased on this increment of the load. However, the increases in strains were not all proportional to the increase in the load. The strain in the second longitudinal fiber exceeds two percent and the strain in the first longitudinal fiber is 1.6 percent. Another crack in a longitudinal fiber to the far right in Fig. 9(*b*) is evident. The curvature of the fringes in the resin region between the first and second fibers is due to a decrease in the value of the shearing strain across the region. The shearing strain is a maximum adjacent to the first fiber and is nearly zero adjacent to the second fiber.

The final moiré pattern in this series, Fig. 9(*c*), corresponds to a tensile stress of 993 MPa, an increase of 20 percent from 828 MPa. The strains at several locations are shown in Table 5. While the applied stress increased 20 percent from Fig. 9(*b*) to Fig. 9(*c*), the shearing strains at the interface and the normal strains in the first longitudinal fiber decreased markedly, because these regions were beginning to unload. The interface has shifted to the right side of the first longitudinal fiber. This shift is apparent from the sharp increase in the shear strain (to 16.7 percent) in the resin region adjacent to and to the right of the first fiber. The normal strain in the resin region and in the second longitudinal fiber has increased to 2.5 percent. The shifting of load from the first to the second fiber is due to extensions of the cross-ply cracks, above and below the moiré grating, that cut across the first longitudinal fiber (see Fig. 11).

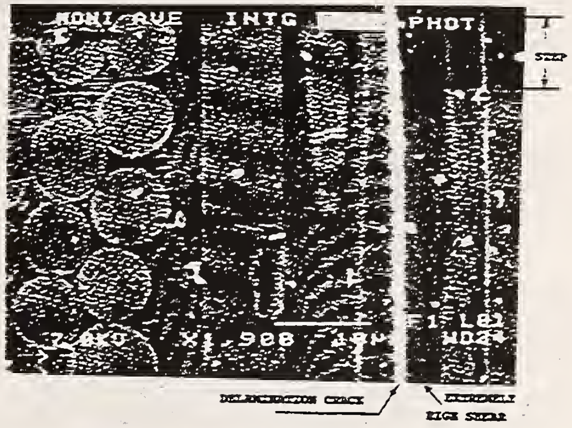

Fig. 10(*a*) Fringe pattern after 0-deg ply delamination cracking, at a stress of 1075 MPa

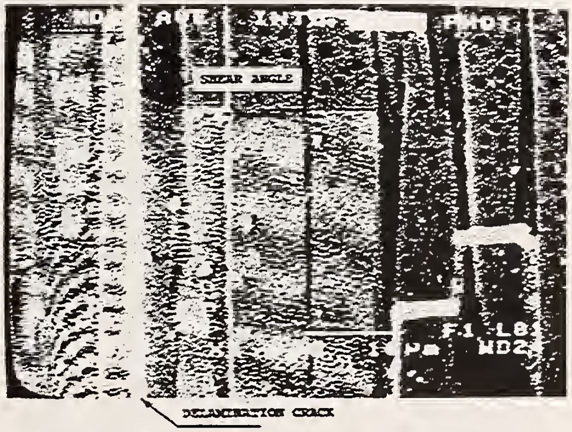

Fig. 10(*b*) Moiré pattern to the right of the delamination crack, at a stress of 1075 MPa

Finally, a pending delamination plane is marked in Fig. 9(*c*), just to the right of the second complete longitudinal fiber. At this interface, continuous moiré fringes are observed that indicate high normal strain (2.5 percent) but relatively small shearing strains.

Longitudinal Ply Failure by Delamination. On the next load increment, to σ = 1075 MPa, a delamination crack appeared in the moiré grating as shown in Fig. 10(*a*). The delamination produced a step-like deformation of the top edge of the moiré grating as illustrated in Fig. 10(*b*), although the specimen continued to support the applied load. An analysis of the regions to the left of the delamination crack gave the strains presented in Table 6.

The delamination did not markedly affect the trends under way at locations to the left of the longitudinal crack. The cross ply at the site is essentially free. The interface and the first longitudinal fiber continue to unload. The strains in the region between the first and second fibers and in the second fiber continue to increase, exceeding 3.2 percent. The shear strain adjacent to the first longitudinal fiber is so high that it was

Table 6 Strains at several locations after delamination

$\sigma = 1075$ MPa

Location	Strain ϵ_y	Strain γ_{xy}
Cross ply	1.96×10^{-4}	—
Interface	7.66×10^{-3}	0.067
First longitudinal fiber	7.66×10^{-3}	—
Second longitudinal fiber	33.4×10^{-3}	—
Resin between first and second fibers		
adjacent first fiber	—	~0.2*
center of region	32.3×10^{-3}	—
adjacent second fiber	—	**

* too large to resolve
** small

not possible to resolve the fringes. It is believed that the shear strain is in excess of 20 percent.

The moiré pattern to the right of the delamination crack is shown in Fig. 10(*b*). The normal strains in the longitudinal fibers are nearly zero. A very high shearing strain exists to the right of the delamination crack. Measurements of the angle of top boundary of the grating across the 2.35 μm wide shear band adjacent to the delamination crack give a shear strain of 41.4 percent.

A photograph at 160× in Fig. 11 shows the different types of damage developed during the monotonic loading to a global tensile stress of 1075 MPa. The cross-ply cracks near the measurement site and in an adjacent 90-deg ply are evident. Extension of the cross-ply cracks into the 0-deg ply and the failure of the first longitudinal fiber explains its unloading at the higher stress levels. Transverse cracks in the longitudinal fibers occur at many locations. These cracks in the longitudinal fibers are to be expected because local strains in the fibers of 3.3 percent give local uniaxial fiber stresses of about 2400 MPa. Delamination cracks have formed between the 0-deg and 90-deg plies and at several locations in the 0-deg plies. These delaminations produce step discontinuities as large as 7.5 μm in the v displacement field.

The distribution of strain ϵ_y across the measurement site is shown in Fig. 12. This graph shows that the strain in the second fiber and the adjacent resin region increased monotonically with the applied stress. Tensile strain in the transverse ply increased at first, then decreased because of cracking in that ply. The resin between the longitudinal and transverse plies had a similar history.

The shear strains measured locally in the epoxy resin were very large. Before delamination, shear strains of 16.7 percent were measured. After delamination, the shear strains were 41.4 percent in a shear band 2.35 μm wide adjacent to a longitudinal crack in the 0-deg ply. Neglecting biaxial effects, the normal stresses in the epoxy in resin-rich areas between fibers are estimated to be at least 1100 MPa.

Following this delamination, the specimen was unloaded and found to be intact. It was then reloaded until failure occurred at a nominal tensile stress of $\sigma = 1220$ MPa.

Discussion and Conclusions

The e-beam moiré method with a high-frequency line grating (10,000 lines/mm) enabled an examination of a small region about 45 μm square at an interface of a $[O_2/90]_s$ glass fiber reinforced plastic. The examination, performed at 1900×, permitted measurement of normal and shearing strains in the cross ply, in the resin-rich region between plies, in the longitudinal fibers, and in resin regions between these longitudinal fibers. The specimen was loaded in uniaxial tension until failure occurred at 1220 MPa. Local strain measurements were made by interpreting the moiré fringe patterns over gage lengths ranging from 10 to 30 μm.

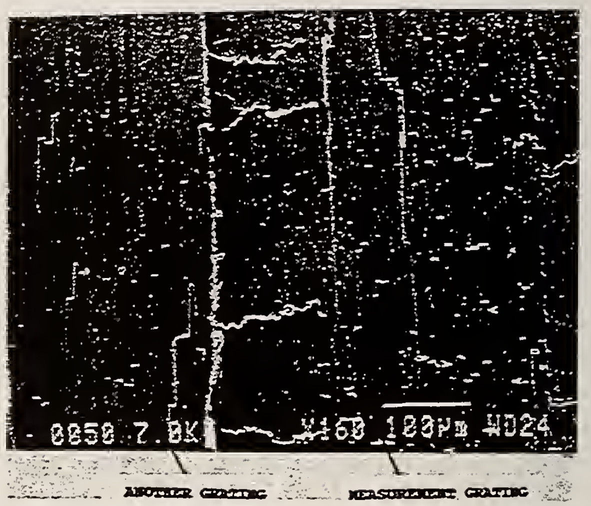

Fig. 11 Cross ply, longitudinal fiber, and longitudinal ply cracking. Also, intraply delamination.

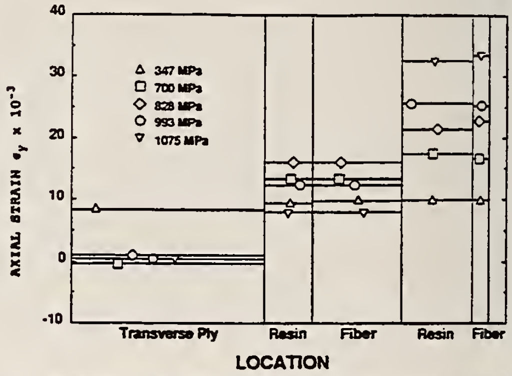

Fig. 12 Strain distribution across the grating for several different applied stress levels

The magnitude and the distribution of the strains depended on the damage that occurred in the specimen as the load was increased and on the location of the damage. From several local strain measurements at a number of locations the following conclusions have been drawn:

(1) Before the failure of the 90-deg ply, there was a difference of 14 percent in ϵ_y across the interface between 0-deg and 90-deg plies with the higher strains in the 0-deg ply. At a nominal stress of 347 MPa, the gradient $d\epsilon_y/dx = 1.2 \times 10^{-4}$ μm^{-1}. Higher strains in the 0-deg ply may indicate that very isolated 90-deg cracking occurred at even lower global stress.

(2) Before failure of the 90-deg ply, we measured a local modulus $E_1 = 36.1$ GPa over a gage length of about 25 μm.

(3) When the 90-deg ply failed by transverse cracking, its load-carrying capability effectively vanished.

(4) Failure of the 90-deg ply produced shearing strains in the resin-rich area between the 0-deg and 90-deg plies. These shearing strains were large and increased with load to 11.9 percent before they were relieved by fracture of adjacent fibers in the 0-deg ply.

(5) Isolated transverse cracks occurred in large numbers in longitudinal fibers at nominal stresses as low as 347 MPa. These cracks produced shearing strains in the epoxy which increased with load to about 13 percent.

(6) After failure of the 90-deg ply, the strain increments at different locations were not proportional to the increments

of the applied (global) stress. The increasing numbers of cracks in the 90-deg plies and in the longitudinal fibers produced a new local geometry at each load increment. This progressive damage by cracking resulted in strain redistribution.

(7) Cross-ply cracks extended into the 0-deg ply and effectively shifted the interface between plies. This shift produced shear strains as large as 16.7 percent in the matrix between longitudinal fibers.

(8) Local delamination occurred due to cracking between 0-deg and 90-deg plies and cracking between longitudinal fibers in the 0-deg ply. However, the specimen remained intact and supported the applied load.

(9) After delamination in the 0-deg ply at $\sigma = 1075$ MPa, fiber strains of 3.34 percent were measured. The corresponding fiber stress, neglecting biaxial effects, was 2400 MPa, which was 2.23 percent larger than the global applied tensile stress.

(10) A delamination crack passing through the moiré grating produced a step discontinuity of 7.5 displacement field. This slippage is consistent with crack-opening displacements associated with transverse cracks in the adjacent 90-deg ply.

(11) A localized shear band was evident in the epoxy matrix material adjacent to the delamination crack. This band was 2.35 μm wide and was produced by an average shearing strain of 41.4 percent.

(12) The epoxy matrix between longitudinal fibers supported normal strains as large as 3.23 percent, which corresponds to a local tensile strength in excess of 1100 MPa if biaxial effects are neglected.

(13) While these experimental results are typical, they are not unique. The strain distributions at each load are clearly dependent on the many different types of damage and the location of each damage site relative to the measurement position.

(14) It is always difficult to specify the accuracy of a measurement and this statement is particularly true when the experimental method is as new as e-beam moiré. The results were obtained from Eq. (3) and involved measuring fringe gradients. It is estimated that the gradients could be determined to ± 4 (± 0.2 fringes in a count of five percent over a gage length of 20 to 30 μm). A second source of error is in the reference pitch p_r. The value of p_r depends on the magnification which was fixed at 1900× to produce all of the moiré fringe patterns. Variations in the magnification due to electronic instabilities in the scanning electron microscope are known to occur, but they have not been studied to date.

(15) Measurements of the strain ϵ_y in the cross ply at high loads after the region was essentially stress-free indicate that the resolution of the measurements was about $\pm$ 1000 $\mu\epsilon$ or $\pm$ 0.1 percent.

Acknowledgments

Thanks are due to R. E. Harris and J. Martinis for the use of the lithographic facility in the Electromagnetic Technology Division at NIST, and to Greg Zimmerli for introducing us to electron beam lithography.

References

Anastasi, R. F., Serabian, S. M., Shuford, R. J., and Das-Gupta, D., 1987, "Nondestructive Detection of Simulated Delaminations in Composite Laminates by Laser-Speckle Shearography," *Experimental Techniques*, Vol. 11, No. 6, June, pp. 28–31.

Bandyopadhyay, S., Gellert, E. P., Silva, V. M., and Underwood, J. H., 1989, "Microscopic Aspects of Failure and Fracture in Cross-Ply Fibre Reinforced Composite Laminates," *Journal of Composite Materials*, Vol. 23, Dec., pp. 1216–1231.

Chamis, C. C., 1974, "Micromechanics Strength Theories for Composite Materials," *Fracture and Fatigue*, Vol. 5, L. J. Broutman, ed., Academic Press, New York, pp. 93–151.

Dally, J. W., and Read, D. T., 1993, "Electron Beam Moiré," *Experimental Mechanics*, Vol. 33, No. 4, Dec., pp. 270–277.

Galiotis, C., Melanitis, N., Batchelder, D. N., Robinson, I. M., and Peacock, J. A., 1988, "Residual Strain Mapping in Carbon Fibre/PEEK Composites," *Composites*, Vol. 19, No. 4, July, pp. 312–324.

Halpin, J. C., 1984, *Primer on Composite Materials: Analysis*, Technomic, Lancaster, PA.

Kishimoto, S., Egashir, M., Shinya, N., and Carolan, R. A., "Local Micro-Deformation Analysis by Means of Microgrid and Electron Beam Moiré Fringe Method," *Proceedings of the Sixth International Conference on Mechanical Behavior of Materials*, M. Jono and T. Inoue, eds., Kyoto, Japan, Vol. 4, pp. 661–666, pp. 1991.

Lee, J-W., Allen, D. H., and Harris, C. E., 1989, "Internal State Variable Approach for Predicting Stiffness Reductions in Fibrous Laminated Composites with Matrix Cracks," *Journal of Composite Materials*, Vol. 23, Dec., pp. 1273–1291.

Post, D., Czarnek, R., Joh, D., Jo, J., and Guo, Y., 1987a, "Experimental Study of Metal-Matrix Composite," *Experimental Mechanics*, Vol. 27, No. 2, June, pp. 190–194.

Post, D., Czarnek, R., and Joh, D., 1987b, "Shear Strains in a Graphite/PEEK Beam by Moiré Interferometry," *Experimental Mechanics*, Vol. 27, No. 3, Sept., pp. 246–249.

Post, D., and Wood, J. D., "Determination of Thermal Strains by Moiré Interferometry," *Experimental Mechanics*, Vol. 29, No. 3, Sept., pp. 318–322.

Post, D., Dai, F. L., Guo, Y., and Ifju, P., 1989, "Interlaminar Shear Moduli of Cross-ply Laminates: An Experimental Analysis," *Journal of Composite Materials*, Vol. 23, No. 3, pp. 264–279.

Tsai, S. W., and Hahn, H. T., 1980, *Introduction to Composite Materials*, Technomic, Lancaster, PA, 1980.

Vinson, J. R., and Sierakowski, R. L., 1986, *The Behavior of Structures Composed of Composite Materials*, Martinus Nijhoff, Boston, MA.

A4

Local Deformation of Plated Through Holes under Thermomechanical Loading

by Read and Drexler (1994)

AMD-Vol. 187, Mechanics and Materials for Electronic Packaging:
Volume 2 – Thermal and Mechanical Behavior and Modeling
ASME 1994

LOCAL DEFORMATION OF PLATED THROUGH HOLES UNDER THERMOMECHANICAL LOADING

David T. Read and Elizabeth S. Drexler
Materials Reliability Division
Boulder Laboratories
National Institute of Standards and Technology
Boulder, Colorado

ABSTRACT

We have studied the thermomechanical deformation of plated through holes in commercial-grade printed wiring board (PWB) made from FR-4 resin reinforced with glass cloth. We used a novel experimental technique, electron-beam moiré. On cross sections through the PWB thickness, line gratings were observed in the scanning electron microscope (SEM). Moiré patterns could be observed when the spatial frequency of the scanning electron beam matched the spatial frequency of the line grating. These patterns were analyzed to obtain local deformation and strain data. We gradually heated the specimens up to near the melting point of their Sn-Pb 63-37 solder and observed thermomechanical deformations. Here we report observations made at SEM magnifications of 110–550X.

INTRODUCTION

Motivation: Verification of finite element analysis of electronic packaging and interconnect structures

This study is motivated by the need to improve the understanding and predictability of the reliability of electronic packaging and interconnect structures. The mechanical sophistication of these structures and their importance to the costs, manufacturability, and reliability of electronic devices have been described by many authors. The treatment of manufacturability and reliability of packaging and interconnect structures (Guo, et al., 1993, Choi, et al., 1993, Lau and Erasmus, 1993) is reaching a high level of sophistication, utilizing finite element analysis. It has been reported that savings in cost and time-to-market have been achieved through the use of finite element analysis of mechanical behavior to streamline and focus procedures in design, inspection, and test (Corbin, 1993).

Finite element analyses are only valuable to the extent that they are known to be accurate. Usual issues affecting their accuracy are the assumed boundary conditions, the failure modes, and the appropriateness of the material behavior models and mesh design for the problem at hand. The use of experimental mechanics to validate finite element analyses is common for analyses of macrostructures (McNeill *et al.*, 1885). It is expected that microscale experimental mechanics studies will contribute significantly to the value of finite element analyses of electronic packaging and interconnect structures, by providing guidance regarding the assumptions needed to begin such analyses, and by adding to the credibility of the analyses by providing verification of some of the results.

Background: Electron Beam Moiré

Electron-beam moiré has much in common with geometric optical moiré. A review of this classic experimental mechanics technique is beyond the scope of this paper; excellent references are Weller (1948), Parks (1987), and Theocaris (1969). Since 1980, most of the development has involved moiré interferometry, where a virtual reference grating is produced by interference of two plane beams from a coherent light source. Examples include Post (1980), McDonach, et al. (1980), Post and Wood (1989), and Post (1991). Moiré interferometry represented a major advance because the density of the specimen grating was increased by a factor of about 50, to 4 000 lines/mm. This increase improved the sensitivity of the method and extended the applicability of the moiré method to a wider range of problems (Post, 1991, and Han, *et al.*, 1994).

TABLE 1. HANDBOOK THERMAL EXPANSION COEFFICIENTS FOR MATERIALS OF CONSTRUCTION OF PTH SPECIMENS.

Material	Coefficient of thermal expansion, ppm/°C
SnPb eutectic solder[1]	23
Cu[2]	17
Glass-fiber–reinforced FR-4 x and y directions[1]	16
Glass-fiber–reinforced FR-4 z (out-of-plane) direction[1]	80

[1] Minges (1989)
[2] Lide (1993)

Electron-beam moiré takes advantage of the higher magnification and depth-of-focus possible with scanning elecron microscopy as compared to optical microscopy. Electron-beam moiré offers two specific advantages relative to optical: finer grating pitch, and higher magnification that does not interfere with the fringe formation process (Kishimoto *et al.*, 1991a and b). The disadvantages of this new technique include: the difficulty of electron-beam lithography, which is needed to produce precise, high-density line gratings and crossed gratings; the lack of developed techniques to record displacements in both x and y directions from the same field (although this seems possible); the need to place the specimen within the vacuum chamber of the SEM; and the general lack of stability of the formation of the SEM image compared to optical images, because the SEM employs electronic components where the optical systems employ lenses and mirrors.

The recent development of electron-beam moiré with high density gratings has been described in the literature. Kishimoto *et al.* (1991a and b) were the first to introduce electron-beam moiré and to demonstrate its application to study microdeformation. In these studies, relatively coarse gratings with pitches between 3.7 and 7.1 µm were used. We have used line gratings with a pitch of 100 nm to demonstrate the ability to produce electron-beam moiré (Dally and Read, 1993), and in a study of mechanical deformation of a composite (Read and Dally, 1993, and Read and Dally, 1994).

Background: Plated through holes (PTH)

The use of PTH as a support and interconnect system for electronic components predates the beginnings of semiconductor electronics. These material systems are described in detail in Minges (1989), and Tummala and Rymaszewski (1989). Modern PWBs may have 18 or more layers, and may have closed and buried vias, as well as PTH. The most popular material for commercial-grade PWB is a resin type known as FR-4, which is reinforced with glass fibers.

The most common reliability problem with PTH on GFRP (glass-fiber–reinforced plastic) PWB arises from out-of-plane thermal expansion. The volume ratio of glass fibers to resin is chosen so that the PWB as a whole has an in-plane coefficient of thermal expansion of about 17 ppm/ °C, matching that of Cu. This choice minimizes the thermomechanical stresses on the Cu interconnect traces. However, the resin and the glass interact to produce an out-of-plane thermal expansion coefficient much larger than the in-plane value. Values of thermal expansion coefficients from Minges (1989) and Lide (1993) are listed in Table 1. Furthermore, the thermal-expansion coefficient of these PWBs has been reported to increase dramatically at the glass transition temperature, around 125 °C (Guo *et al.*, 1993). The expansion of the GFRP PWB in the through-thickness or z-direction, applies tensile strains to the Cu barrels of the PTH. This loading is a known threat to the manufacturability and reliability of glass-reinforced FR-4 PWB with PTH (Davidson, 1991). Tensile strains along the Cu barrels of the PTH occur every time the PWB is heated. These strains are reversed when the PWB is cooled. This strain cycling can produce fatigue cracks in the Cu, which in turn can interrupt the electrical connection along the PTH, resulting in functional failure of the device. Careful quality control of the manufacturing operations involved in producing the PTH is necessary in order to avoid reliability problems.

EXPERIMENT

Technique

Preparation of line gratings on cross sections of PWB was accomplished using electron-beam lithography. Because of the novelty of the technique, a brief summary is given. We used a series of SiC-coated papers with grit sizes ranging from 260 to 5 µm to grind the specimen to a thickness of 3 mm or less, to produce smooth a surface containing the mid-planes of several PTH. Final polish was obtained with 3 and 1 µm natural diamond aerosol spray. The surface of the specimen was swabbed with methanol. The specimen was cleaned in a methanol ultrasonic bath for 30 s, and, finally, the surface was scrubbed with acetone on a soft polishing cloth. Within 2 h of the final polish and cleaning, the specimen was sputter-coated with AuPd.

Two percent polymethyl methacrylate (PMMA) in chlorobenzene solution was used as a positive electron-sensitive resist (Haller, 1968). The specimens were spin-coated with

PMMA at rates of 2000 to 3000 rpm, and baked for 90 min at 170 °C to cure the PMMA. To prevent degradation of the resist, patterns were written on the specimens within a few hours of the curing of the PMMA.

The SEM has been used to write line gratings ranging in size from 60 to 1200 μm. We started with gratings of 512 lines, and progressed to 1024 lines. Three different sized gratings were used in this study—1200, 600, and 240 μm. The line pitches range from 200 to 1000 nm. For writing the line gratings, the SEM was operated with an accelerating voltage of 20 kV and a working distance of 13–14 mm. The lines were exposed with beam currents between 50 and 750 pA. The time required to write each grating varied from 4 to 22 min.

After exposure, the specimen was developed in a 3:1 solution of isopropanol (IPA) and methyl isobutyl ketone (MIBK) for 40 s. This was followed by a 20 s rinse in IPA and a 30 s rinse in deionized water. Finally, the specimen was sputter-coated with AuPd, to provide a thin (5 nm) conductive layer.

Figure 1 is a photomicrograph of the lines written on a sample of metal. These lines have a pitch of 160 nm. We always wrote lines parallel to the PWB surface, to enable us to measure the z-direction (out-of-plane) deformation. The dark stripes are trenches in the PMMA, produced where the electron-beam exposure causes unlinking of the PMMA molecules, so they are preferentially dissolved by the IPA:MIBK solution. The brighter regions adjacent to the dark trenches are ridges. Figure 1 shows that the line profile as imaged by the SEM is not a simple square wave. The line corners show up more intensely than the line centers or the spaces. This complex profile reappears in the moiré fringes.

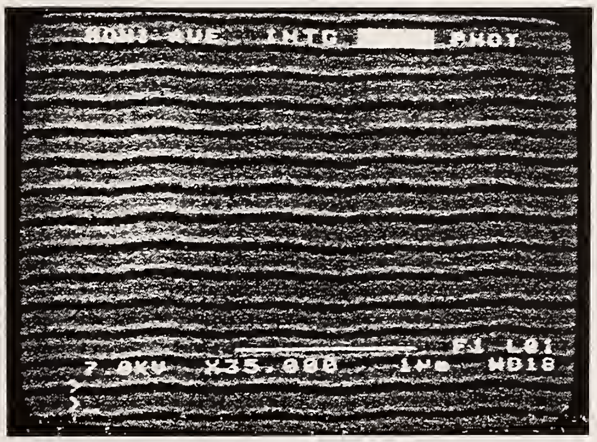

FIGURE 1. SEM MICROGRAPH OF A LINE GRATING WITH A PITCH OF 0.16 μm, ON METAL.

To observe thermally-induced displacements, we mounted the specimen on a heating stage within the SEM, as shown in figure 2. The stage is rated for temperatures up to 1000 °C, but we have used it only up to 180 °C. One thermocouple was mounted on the heater chip, and a second was attached between the specimen clamp and the specimen. We focussed the microscope on the selected line grating, at a magnification that produced moiré fringes. Because the magnification of our microscope is adjustable only in discrete steps, we were unable to produce a null field (an exact match between the line pitch and the pitch of the rastered electron beam). We started our experiments with 3 to 10 carrier fringes present. The stepwise-adjustable magnification and the possible initial rotation of the specimen can only produce straight, regularly spaced fringes, which may be horizontal or may be slanted if rotation is present. Depending on whether the magnification was above or below the value that would produce null field, the fringe density increased or decreased with extensional strain. We took photographs of the SEM display, and we also recorded the images digitally. The computer sdores the images as 480 lines of 512 8-bit pixels.

The electrical power to the heater is manually controlled. We heated the specimen to temperature, waited for equilibrium, and recorded the moiré fringe pattern. The recording of an image required about 30 s. Two problems were discovered with the heating stage. First, the heater produced an electric field, which caused the images to be distorted. To avoid such problems, we used a non-inductively wound ceramic heater chip, we placed magnetic shielding between the heater and the specimen, and we grounded the heater circuit to the microscope chamber. The second problem was that as the stage and specimen heat, the specimen moved relative to the position of the electron beam.. Because the moiré fringe spacing would be affected if the specimen were moving during the recording of the image, we recorded images only after making sure that the motion had stopped, by observing an individual line of the grating at high magnification. Changing temperature sometimes required 30 min or more.

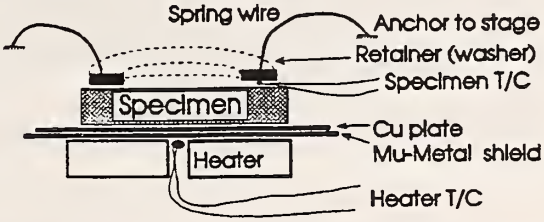

FIGURE 2. SCHEMATIC DRAWING OF THE HEATING STAGE USED WITH THE SEM.

Data reduction was accomplished by manually tracing the fringes, to produce a list of x,y pairs for each fringe. Subsequent calculations of displacement and strain as functions of position were automated. Spline fitting was used to interpolate from the traced points to a regular grid, and to calculate strains from displacements. We can obtain the y-direction displacement v as a function of x and y. From these data we can calculate ε_{yy}, the normal strain in the y direction, as $\varepsilon_{yy} = \partial v/\partial y$. This strain is available as a function of x and y. Because we were able to measure only v, the displacement in the y-direction, we were

TABLE 2. DIMENSIONS OF PTH USED IN THIS STUDY.

PWB thickness	1.56 mm (1/16 in)
Hole spacing, center-to-center	2.54 mm (1/10 in)
Diameter, drilled hole in GFRP	1.11 mm (0.044 in)
Cu thickness, in PTH	45 μm (0.002 in)

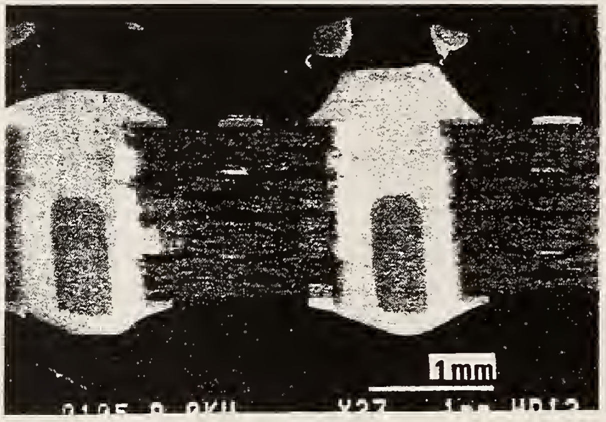

FIGURE 3. SEM MICROGRAPH OF A CROSS-SECTION PTH SPECIMEN.

unable to properly calculate shear strain, since the engineering shear strain γ_{xy} is given as $\gamma_{xy} = \partial v/\partial x + \partial u/\partial y$. Similarly, the rotation ω is given by $\omega = \partial v/\partial x - \partial u/\partial y$. However, these equations suggest a way to estimate the shear strain. If the -- direction displacement u is either constant or small, the shear strain can be estimated as $\gamma_{xy} \approx \partial v/\partial x$. On our moiré fringe images, slanted fringes correspond to significant values of $\partial v/\partial x$. We try to avoid slanted fringes in our initial conditions. When slanted fringes are present, we know that either shear strain or rotation has occured. If we can eliminate the likelihood of rotation, or show that u is small or constant, then we can estimate the shear strain.

Plated-Through-Hole Specimens

We studied cross sections of PTH extracted from an FR-4 commercial grade PWB, that had been soldered with eutectic SnPb. Our PWB had 4 layers of copper conductors, one on each surface and 2 within the PWB. Table 2 gives the dimensions of the PWB and the PTH.

Figure 3 shows a photograph of a typical cross-section. The printed circuit board with its reinforcing glass fibers is visible between the through holes. The narrow rim (~0.05 mm thick) at the edges of the through holes is the Cu plating. The lighter colored fill is the SnPb solder, and the darker oblongs within the PTH are Cu pins. The light squares are line gratings.

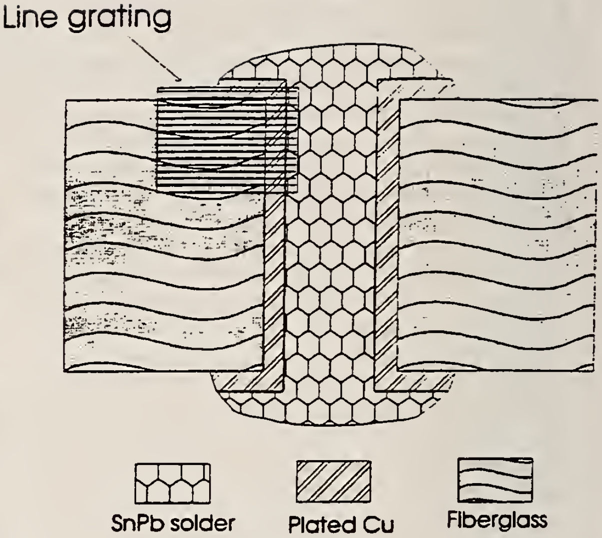

FIGURE 4. SCHEMATIC DIAGRAM OF THE PTH USED IN THIS STUDY.

Figure 4 shows the PTH schematically. A line grating placed at the corner of the PTH is indicated.

RESULTS AND DISCUSSION

This paper presents in detail the results of three experiments on three different specimens from the same PWB. Table 3 lists the basic conditions of these three experiments. In each of these cases, we present moiré fringe images and data from one grating. Additional gratings on these specimens and other specimens from this PWB were also studied. Those additional results contributed to our understanding and interpretation of the behavior of these PTH.

Extensive shear

In two experiments, we observed what appears to be extensive shear deformation allowing accommodation of the high out-of-plane thermal expansion of the GFRP with the lower expansion of the PTH by extensive shear deformation. Both examples were seen at PTH corners. The more striking example, from specimen number 1 is shown in figures 5a-c. Figure 5a shows schematically the location of the line grating. Figure 5b shows the condition at 35 °C, before heating. Figure 5c shows the condition after heating to 136 °C.

TABLE 3. LINE GRATINGS USED IN THIS STUDY.

Experiment	Purpose	Location	Magnification	Field Width, µm	Line Pitch, µm	Number of lines
PTH 1	Extensive shear	corner	250	405	0.40	1023
PTH 2	Extensive shear	corner	220	455	0.45	1023
PTH 3	Local shear	corner	550	180	0.35	511

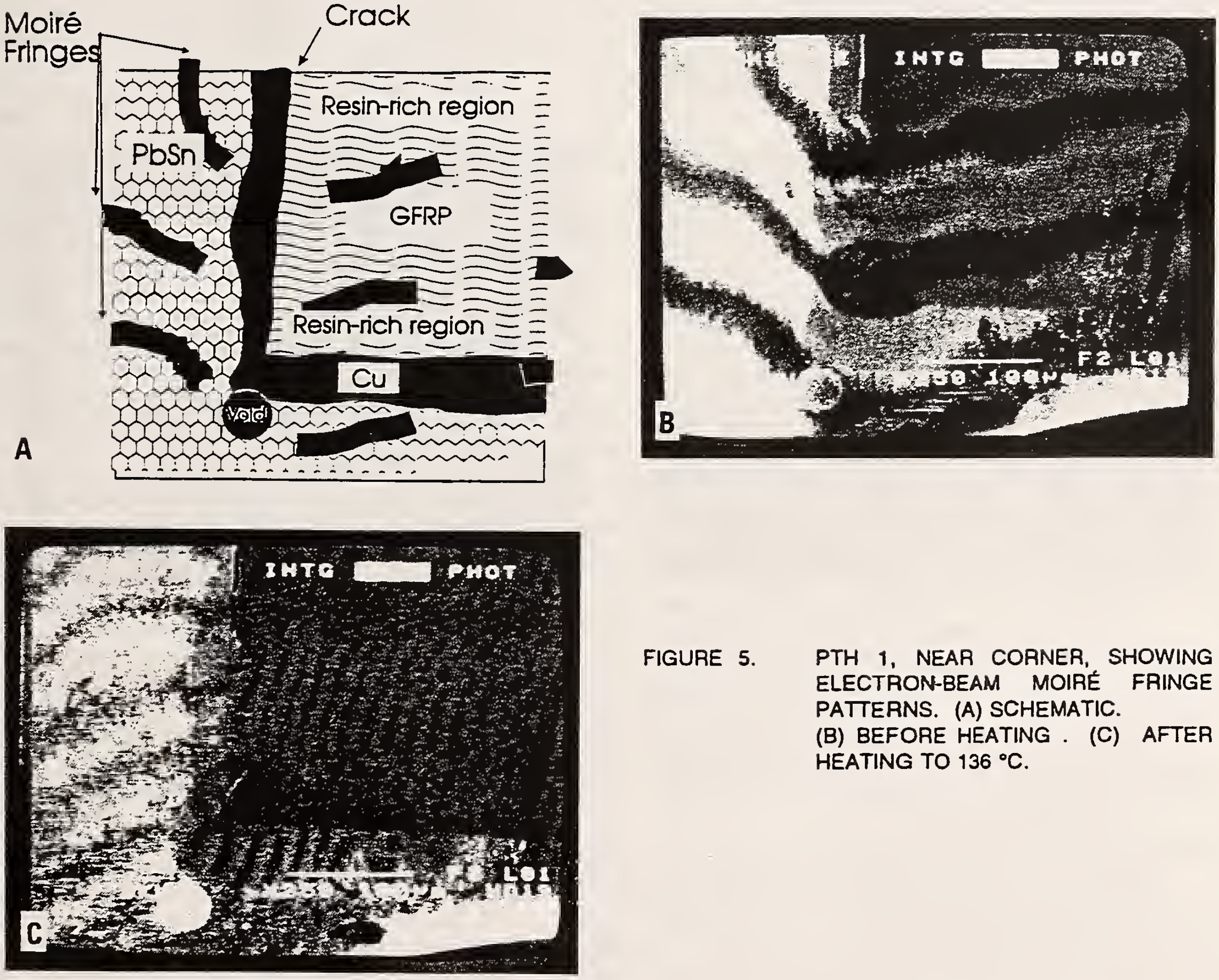

FIGURE 5. PTH 1, NEAR CORNER, SHOWING ELECTRON-BEAM MOIRÉ FRINGE PATTERNS. (A) SCHEMATIC. (B) BEFORE HEATING . (C) AFTER HEATING TO 136 °C.

In the SnPb and Cu, there are about 3 fringes in figure 5b, and about 5 in figure 5c. If we consider 20×10^{-6} / °C as a rough average thermal-expansion coefficient in the Cu and Sn, we calculate a thermal strain of about 2×10^{-3}. Since this grating has 1023 lines, this strain should add 2 fringes, as observed in figure 5c. More detailed measurements of thermal strains, discussed below, will show that we can indeed measure thermal strains in SnPb and Cu using the electron-beam-moiré technique, but that the agreement in this case between the observation and the coefficient of free thermal expansion is only coincidental. The

TABLE 4. LOCATIONS OVER WHICH THERMOMECHANICAL STRAINS WERE AVERAGED FOR FIGURE 6c.

Specimen	Location	Material	Distance from:	X1, µm	X2, µm	Y1, µm	Y2, µm
2	PWB corner	GFRP	Cu	25	200	25	100
		SnPb	Cu	0	20	25	100

In figure 5c, note the many fringes at a steep angle to the horizontal. These tilted fringes are suggestive of shear strain. Because we have measured only the y-direction deformation in this experiment, we cannot distinguish, on the basis of the local fringe angles alone, between shear and rotation, as discussed above. But in these patterns the fringes bend sharply at the interface between the Cu and the GFRP, so rigid body rotation can be excluded. The bent fringes indicate a shear or a rotation of the fiberglass relative to the metal parts of the PTH. We favor shear over rotation because an extensive region of rotation would require impossibly large displacements within the body of the PWB. The fringes in the GFRP in figure 5c indicate that, at this PTH, the out-of-plane displacement of the PWB surface increased rapidly with distance from the PTH.

Based on the free thermal-expansion coefficients of GFRP and of SnPb solder, we would expect a strain difference, from solder to fiberglass, of 0.0058 between figure 5b and figure 5c, at 35 and 136 °C, respectively. Over the distance from the PWB centerline to the surface, this would produce a displacement difference of 4.6 µm. Because the fringe pitch in this grating was 0.40 µm, such a displacement would produce a total climb of 11 1/2 fringes from SnPb to GFRP. The strain difference between SnPb and GFRP would also produce a difference in fringe density of 6 fringes over the frame height. Figures 5b and 5c clearly show fringe climb of at least 6 fringes across the frame. This is consistent with expectation, because the remaining climb could occur outside the region shown in figure 5, further away from the PTH. At first glance the density difference appears large also, but closer examination shows that the density in the vertical direction is about 7 fringes per frame height in the center of the frame, compared to about 5 in the SnPb. This indicates that the GFRP next to the PTH is not expanding freely, but is partially restrained by the PTH structure.

The striking deformation portrayed in figures 5b and 5c is consistent with expected behavior for PTH. Figures 5a-c provide one unexpected finding, the highly localized strain in the GFRP, at the regions where the fringes curve. These localized strains occurred in the resin-rich regions of the PWB. Although generally similar deformation to that shown in figures 5a-c was observed on other PTH, the deformation gradient near the PTH was much less intense in other specimens. This is discussed further below.

Figures 6a-e display the use of moiré fringe data to obtain thermal strains. Figures 6 are from specimen 2 near the PTH corner. Figure 6a indicates the locations of the PTH components relative to the line grating. Figures 6b-6d show the moiré fringe patterns at 22, 78, and 125 °C. The thermal strains are plotted against temperature in figure 6e. In figure 6e, we show handbook values for thermal strain for GFRP calculated for free expansion. These "handbook" strains are not expected to actually predict the behavior of the PTH structure, but they provide a baseline for comparison. Table 4 gives the locations of the specific regions over which the strains were averaged.

The behavior at the PTH corner shown in figures 6 was also seen in other specimens. The data indicate a low rate of expansion near room temperature, followed by an increasing rate of expansion as the temperature rises above about 75 °C. The big drop in the strain in the GFRP in figure 6 at ~120 °C was accompanied by a local failure of the GFRP, indicated by a complex fringe pattern. The thermal expansion continued after this disturbance. As the temperature was increased further, the expansion took on its expected positive value. The deviation of these strains from handbook values are indicative of the thermomechanical interaction among the different materials in this composite structure.

Precedent exists for the highly non-linear, and somewhat counter-intuitive, behavior indicated by the present results. Hall (1984), in a well-known experiment on the thermomechanical behavior of structures including solder and PWBs, reported nonlinear deformation with temperature, hysteresis, and, over a small range, deformation of the opposite sign than predicted by a linear bimaterial model.

From the present results we would expect that much greater damage at the corners of PTH structures should occur when they are cycled to temperatures above 75 °C than when temperatures are restricted to 75 °C or less. The one observation we have of the behavior in the middle of the PWB indicates that at this location, thermal strains are high from the beginning.

Shear near the fiberglass-SnPb-Cu interface

Specimen 3 provided moiré images that displayed shear strain near the fiberglass-SnPb-Cu interface, figures 7a-7c. Figure 7a is the schematic indicating the location relative to a PTH.. Figure 7b shows a typical fringe pattern taken near a PTH corner cooled to 40 °C after the specimen had been heated to 143 °C. This image shows shear deformation in the SnPb of the PTH. As noted above, shear strain can only be estimated from our moiré fringe images. In this image, local rotation can be ruled out, so the slanted fringes are attributed to shear. Figure 7c shows the dependence of the shear deformation on distance into the SnPb from the plated Cu. Some shear deformation was present near the

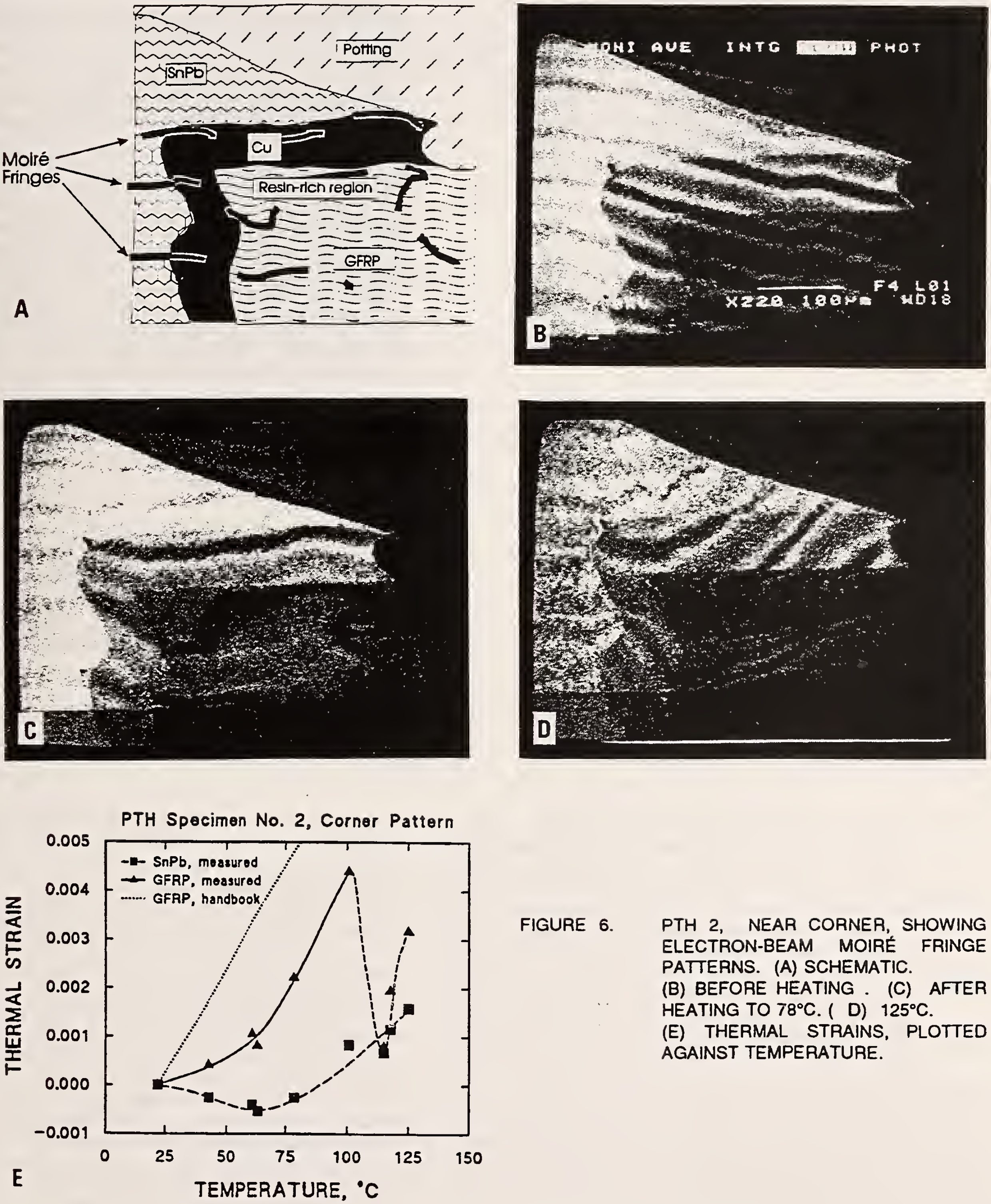

FIGURE 6. PTH 2, NEAR CORNER, SHOWING ELECTRON-BEAM MOIRÉ FRINGE PATTERNS. (A) SCHEMATIC. (B) BEFORE HEATING . (C) AFTER HEATING TO 78°C. (D) 125°C. (E) THERMAL STRAINS, PLOTTED AGAINST TEMPERATURE.

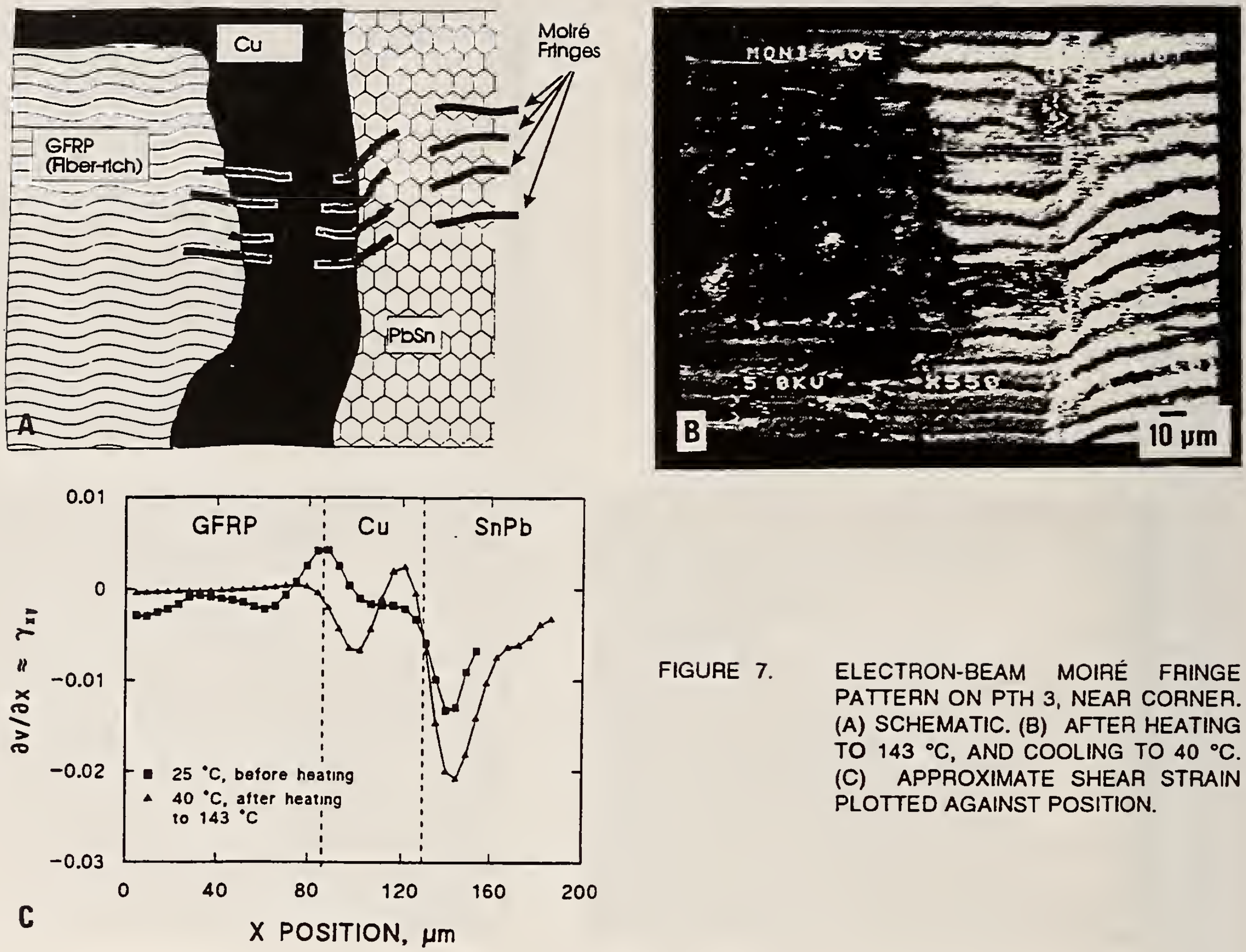

FIGURE 7. ELECTRON-BEAM MOIRÉ FRINGE PATTERN ON PTH 3, NEAR CORNER. (A) SCHEMATIC. (B) AFTER HEATING TO 143 °C, AND COOLING TO 40 °C. (C) APPROXIMATE SHEAR STRAIN PLOTTED AGAINST POSITION.

PTH corner when the specimen was first observed before heating, as indicated in Figure 7c. We atttribute this deformation to the recovery of residual deformations introduced during the curing of the PMMA coating on the specimen. We have observed other instances of deformation present in PTH specimens upon initial examination. We interpret this deformation as follows. The specimens are baked at 150 °C to harden the PMMA that is used as the electron resist in writing the line gratings. This heating introduces thermomechanical deformations, some portion of which remain as residual deformation after the specimen is cooled. This residual deformation recovers gradually, over a period of days or longer. Over the time between the writing of the grating and initial observation, this recovery process progressed. The deformation indicated by the initial fringes is part of this recovering residual deformation. This indicates that the PTH structures are somewhat fragile as regards microdeformations.

These initial shear deformations were not present in every location imaged, but they were seen more than once. The present study is not intended to provide accurate statistics, but we have probably looked at a total of 20 locations on 5 PTH specimens. Shears as shown in figures 7a-7c were seen 2 or 3 times.

SUMMARY CONCLUSIONS

(1) Line gratings with pitches down to 160 nm can be fabricated by electron-beam lithography on cross sections of PTH, and can be used to form electron-beam–moiré patterns at magnifications of 110 to 550X. These patterns carry information about local deformations in the surface.

(2) By heating such specimens in the SEM and recording the changing moiré patterns, thermomechanical deformations can be measured. Even though we could only record digitally scans of 500 lines, we obtained better results with 1023-line gratings than we did with 511-line gratings. The phenomenon of fringes of division, which is related to fringe multiplication, allows us to utilize the full grating density. These moiré patterns were formed on unstressed specimens and on specimens heated up to 150 °C.

(3) The moiré fringe images obtained allowed us to make separate measurements of local thermomechanical behaviors in the

three materials within our PTH specimens: the PWB, the Cu plating, and the SnPb solder. We observed several thermomechanical deformation phenomena: shear that appeared both before the specimen was heated and during heating; differences between the strains in GFRP and nearby SnPb solder, with low deformation on initial heating followed by an increasing deformation rate with temperature above 75 °C at the PTH corners; and extensive shear at the top of PTH to accommodate the greater expansion of the GFRP.

(4) We observed considerable variability in the behaviors of our PTH specimens—variability from location to location on individual specimens, and variability from specimen to specimen. Because the PTH specimens used here were commercial-grade PWB made with SnPb eutectic solder and GFRP, the variability is understandable. We had no way of testing our PTH to failure. However, some of these variable behaviors appeared to be possible precursors to failure of the PTH. These include local shear and slip at SnPb-Cu interfaces, and extensive shear in the GFRP near PTH corners. We don't list fiberglass breakup as a variable behavior because it seemed to occur in at least one location in every test.

The fact that slip and shear were variable behaviors indicates the possibility that they can be avoided. The local shear and slip at the Cu-SnPb interface seem related to the solderability of the plating; this is a well-known issue in PTH reliability. The extensive shear deformation of the GFRP near the PTH is related to the documented difference in out-of-plane thermal expansion of the GFRP relative to Cu and SnPb solder. The surprise was that this deformation does not always manifest itself right up to the PTH barrel. Perhaps, through the use of thick solder fillets or extra-well-reinforced GFRP, the PTH barrels can be protected from the through-thickness, thermally-induced strains.

ACKNOWLEDGEMENTS

The assistance of J. W. Dally in revising this paper is appreciated.

REFERENCES

Choi, H.-C., Guo, Y, LaFontaine, W., and Lim, C.K., 1993, "Solder Ball Connect (SBC) Assemblies under Thermal Loading: II. Strain Analysis Via Image Processing, and Reliability Considerations," *IBM Journal of Research and Development*, Vol. 37, pp. 649–659.

Corbin, J.S., 1993, "Finite Element Analysis for Solder Ball Connect (SBC) Structural Design Optimization," *IBM Journal of Research and Development*, Vol. 37, pp. 585–596.

Dally, J.W., and Read, D.T., 1993, "Electron Beam Moiré," *Experimental Mechanics*, Vol. 33, pp. 270–277.

Davidson, D.L., 1991, "Stereoimaging Determination of Strains in Surface Mounted Components and Plated Through Holes Resulting from Thermal Cycling," *Materials Research Society Symposium Proceedings, Vol. 226, Mechanical Behavior of Materials and Structures in Microelectronics*, E. Suhir, R.C. Cammarata, D.D.L. Chung, and M. Jono, Eds, Materials Research Society, Pittsburgh, pp. 357–361.

Guo, Y., Lim, C.K., Chen, W.T., and Woychik, C.G., 1993, "Solder Ball Connect (SBC) Assemblies under Thermal Loading: I. Deformation Measurement Via Moiré Interferometry, and Its Interpretation," *IBM Journal of Research and Development*, Vol. 37, pp. 635–648.

Hall, P.M., 1984, "Forces, Moments, and Displacements During Thermal Chamber Cycling of Leadless Ceramic Chip Carriers Soldered to Printed Boards," *IEEE Transactions on Components, Hybrids, and Manufacturing Technology*, Vol. CHMT-7, pp. 314–327.

Haller, I., Hatzakis, M. and Srinivasan, R., 1968, "High Resolution Positive Resists for Electron-Beam Exposure," *IBM Journal Research and Development*, Vol. 12, pp. 251–256.

Han, B., Guo, Y., and Lim, C.K., 1994, "Applications of Moiré and Microscopic Moiré Interferometry to Electronic Packaging Product Development," *Conference Proceedings of the 4th Annual IEEE Dual-Use Technologies and Application Conference*, Rome, NY (in press).

Kfouri, A.P., Wong, H.D., and Miller, K.J., 1992, "Elastic–Plastic Finite Element Analyses of Cracked Notches in Plates under Mixed-Mode Loading," *Fatigue and Fracture of Engineering Materials and Structures*, Vol. 15, pp. 743–762.

Kishimoto, S., M. Egashira, Shinya, N. and Carolan, R.A., 1991, "Local Micro-Deformation Analysis by Means of Microgrid and Electron Beam Moiré Fringe Method," *Proceedings of the Sixth International Conference on Mechanical Behavior of Materials*, Vol. 4, M. Jono and T. Inoue, Eds., Kyoto, Japan, pp. 661–666.

Kishimoto, S., Egashira, M. and Shinya, 1991, "Measurement of Grain Boundary Sliding and Observation of Microgrids for High Temperature Use," *Journal of the Society for Materials Science Japan*, Vol. 40, pp. 637–641 (in Japanese).

Lau, J., and Erasmus, S., 1993, "Review of Packaging Methods to Complement IC Performance," *Electronic Packaging and Production*, Vol. 33, No. 6, pp. 50–56.

Lide, D.R., Ed., 1993, Handbook of Chemistry and Physics, CRC Press, Boca Raton, FL, pp. 12-134.

McDonach, A., McKelvie, J., and Walker, C.A., 1980, "Stress Analysis of Fibrous Composites Using Moiré Interferometry," *Optics and Laser Engineering*, Vol. 1, pp. 85–105.

McNeill, S. R. , Sutton, M. A., and Turner, J. L., 1985, "Stress Analysis of a Reversed Dish Head of a Cylindrical Pressure Vessel, *International Journal of Pressure Vessels and Piping*, Vol. 18, pp. 81-90.

Minges, M.L., Technical Chairman, 1989, *Electronic Materials Handbook, Vol. 1: Packaging*, ASM International, Materials Park, OH.

Parks, V.J., 1987, "Geometric Moiré," *Handbook on Experimental Mechanics*, A.S. Kobayashi, Ed., Prentice-Hall, Englewood Cliffs, N.J., pp. 282–313.

Post, D., 1980, "Optical Interference for Deformation Measurements—Classical, Holographic and Moiré Interferometry," *Mechanics of Nondestructive Testing*, W.W. Stinchcomb, Ed., Plenum Press, New York, pp. 1–53.

Post, D., 1991, "Moiré Interferometry: Advances and Applications," *Experimental Mechanics*, Vol. 31, pp. 276–280.

Post, D. and Wood, J. D., 1989, "Determination of Thermal Strains by Moiré Interferometry," *Experimental Mechanics*, Vol. 29, pp. 318–322.

Read, D.T., and Dally, J.W., 1993, "Local Strain Measurement by Electron Beam Moiré," in *Advances in Electronic Packaging 1993, EEP-Vol. 4-1, Proceedings of the 1993 ASME International Electronics Packaging Conference*, P.A. Engel and W.T. Chen, Eds., ASME, New York, pp. 163–169.

Read, D.T., and Dally, J.W., 1994, "Electron-Beam Moiré Study of Deformation of a GFRP Composite," *Journal of Applied Mechanics*, Vol. 61, pp. 402-409..

Theocaris, P.S., 1969, *Moiré Fringes in Strain Analysis*, Pergamon Press, Elmsford, N.Y.

Tummala, R.R., and Rymaszewski, E.J., Eds., 1989, *Microelectronics Packaging Handbook*, Van Nostrand Reinhold, New York, NY, 1194p.

Weller, R. and Shepard, B.M., 1948, "Displacement Measurement by Mechanical Interferometry," *Proceedings of the Society for Experimental Stress Analysis*, Vol. 6, pp. 35–38.

A5

Thermomechanical Behavior of a High Density Polymer Overlay MCM Interconnect Structure: Experiments and Analysis

by Read, et al. (1995)

EEP-Vol. 11/MD-Vol. 64, Application of Fracture Mecha in
Electronic Packaging and Materials
ASME 1995

THERMOMECHANICAL BEHAVIOR OF A HIGH DENSITY POLYMER OVERLAY MCM INTERCONNECT STRUCTURE: EXPERIMENTS AND ANALYSIS[1]

D. Read and E. Drexler
National Institute of Standards and Technology
U. S. Dept. of Commerce, Boulder Laboratories
Boulder, Colorado

E. Bernard
General Electric Corporate Research and Development
Schenectady, New York

I. Grosse, J. Benoit, and J. DiTomasso
Department of Mechanical Engineering
University of Massachusetts
Amherst, Massachusetts

D. Holzhauer, P. Rocci, and M. Stoklosa
Rome Laboratories/ERDS
Griffis Air Force Base, New York

ABSTRACT

Thermomechanical strains in a high density polymer overlay multichip module (MCM) interconnect structure have been studied experimentally with electron-beam moiré and numerically using finite element analysis (FEA). The interconnect structure includes micron-thickness copper traces and laminated dielectric layers with a thermoplastic adhesive to bond the first layer and a polyimide-epoxy blend for the other layers. Copper vias connect the layers. On heating from ambient to 150 C, the experimentally measured out-of-plane strains inside the vias approached 1 percent, and the strain in the polyimide away from vias reached about 1.5 percent.

A two-dimensional plane stress analysis was used for this comparison. The finite element model utilized predetermined temperature-dependent material properties and nonlinear elastoplastic material behavior. Comparison of the analysis and the experiment was carried out using total out-of-plane strain, which includes both a free thermal expansion component and a structural, or thermomechanical component. Good quantitative agreement was found in some regions of the interconnect structure, while in other regions the measured strain values were a factor of two or higher than predicted by finite element analysis. Possible sources for the large differences are discussed.

INTRODUCTION

Motivation: Verification of finite element analysis of electronic packaging and interconnect structures

This study is motivated by the need to improve the understanding and predictability of the reliability of electronic packaging and interconnect structures. The mechanical sophistication of these structures and their importance to the costs, manufacturability, and reliability of electronic devices have been widely documented, *e.g.*, in the National Technology Roadmap for Semiconductors (1994). The treatment of manufacturability and reliability of packaging and interconnect structures (Guo *et al.*, 1993, Choi, *et al.*, 1993, Lau and Erasmus, 1993) is reaching a high level of sophistication, utilizing finite element analysis. It has been reported that savings in cost and time-to-market have been achieved through the use of finite element analysis of mechanical behavior to streamline and focus procedures in design, inspection, and test (Corbin, 1993).

Finite element analyses are only valuable to the extent that they are known to be accurate. Usual issues affecting their accuracy are the assumed boundary conditions, the failure modes, and the appropriateness of the material behavior models and mesh design for the problem at hand. The use of experimental mechanics to validate finite element analyses is common for analyses of macrostructures (McNeill *et al.*, 1985). It is expected that microscale experimental mechanics studies will contribute significantly to the value of finite element analyses of electronic packaging and interconnect structures. Such studies provide guidance regarding the assumptions needed to begin such analyses, and add to the credibility of the analyses by providing verification of some of the results.

An important difference between macroscale experimental mechanics studies and the present study is that in most macroscale studies the applied stress has been produced by the application of force or pressure. In electronic interconnect structures, the significant stresses are thermomechanical. These stresses arise from the presence of materials with different thermal expansion coefficients in structures that are subjected to temperature changes. The techniques used here have been specially adapted to the observation of thermomechanical strains.

---

[1] Contribution of the U.S. National Institute of Standards and Technology, not subject to copyright in the U. S. A.

Background: Electron Beam Moiré

Electron-beam moiré has much in common with geometric optical moiré. A review of this classic experimental mechanics technique is beyond the scope of this paper; excellent references are Weller (1948), Parks (1987), and Theocaris (1969). Since 1980, most of the development has involved moiré interferometry, where a virtual reference grating is produced by interference of two plane beams from a coherent light source. Examples include Post (1980), McDonach, *et al.*(1980), Post and Wood (1989), and Post (1991). Moiré interferometry represented a major advance because the density of the specimen grating was increased by a factor of about 50, to 4 000 lines/mm. This increase improved the sensitivity of the method and extended the applicability of the moiré method to a wider range of problems (Post, 1991, and Han, *et* al., 1994).

Electron-beam moiré takes advantage of the higher magnification and depth-of-focus possible with scanning electron microscopy (SEM) as compared to optical microscopy. Electron-beam moiré offers two specific advantages relative to optical: a wider range of grating pitch, and higher magnification that does not interfere with the fringe formation process (Kishimoto *et al.*, 1991a and b). The disadvantages of this new technique include: the difficulty of electron-beam lithography, which is needed to produce precise, high-density line gratings and crossed gratings; the lack of developed techniques to record displacements in both x and y directions from the same field (although this seems possible); the need to place the specimen within the vacuum chamber of the SEM; and the general lower stability of the SEM image as compared to optical images, because the SEM employs electronic components where the optical systems employ lenses and mirrors.

Kishimoto *et al.* (1991a and b) were the first to introduce electron-beam moiré and to demonstrate its application to study microdeformation. In these studies, relatively coarse gratings with pitches between 3.7 and 7.1 μm were used. We have used line gratings with a pitch of 100 nm to demonstrate the ability to produce electron-beam moiré (Dally and Read, 1993), and in a study of mechanical deformation of a composite (Read and Dally, 1993, and Read and Dally, 1994).

Specimen versus Device-in-Service Comparisons

The purpose of this paper is to compare finite element analysis and high resolution experimental mechanics results for a specific case relevant to advanced electronic interconnect structures. Because the experimental mechanics technique requires access to a cross section, the behavior examined here is not identical to the behavior in a working device with its structure intact. However, both the analysis and the experiment can treat the cross-sectioned specimen. In this way the analysis can be verified or adjusted if need be. The analysis can then be recast to eliminate the cross-section surface and thus treat the actual structure as it exists in the application. During the course of this study, certain observations were made which revealed additional issues regarding prepared-specimen *versus* intact-device comparisons. These observations and issues are discussed below.

SPECIMENS

The structure evaluated in this study was designed to be an economical, high-performance packaging and interconnect structure for multichip modules. The structure is designated as high density interconnect (HDI), and it has several distinguishing features (Fillion *et al.*, 1994). A schematic diagram is shown in Figure 1. Pockets are milled in the alumina substrate to accommodate the chips. An initial sputtered TiAl metallization layer forms the substrate input-output connections. The first overlay layer is polyimide, bonded to the underlying metallization layer with a thermoplastic resin. After the formation of via holes in the polyimide, a TiCuTi metallization layer is added. This tri-metal layer forms connections to the underlying metallization by covering the via holes and is patterned to provide in-layer connections. Subsequent layers repeat this design. The subsequent dielectric overlays are also polyimide, bonded to their underlayers by a polyimide/epoxy thermoset adhesive. The subsequent metal layers are TiCuTi. The nominal layer thicknesses are given in Table 1.

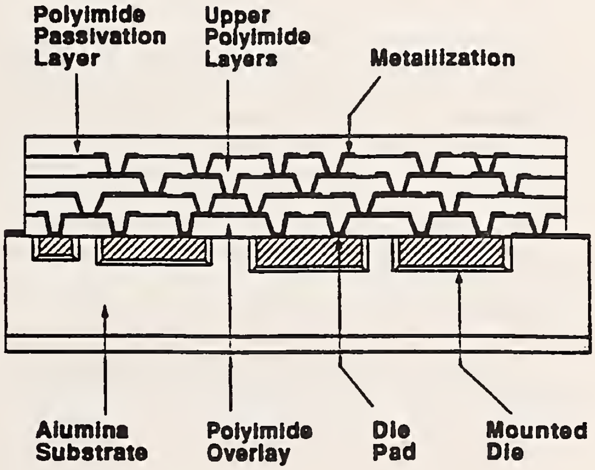

FIGURE 1. HIGH DENSITY POLYMER OVERLAY MULTICHIP MODULE INTERCONNECT STRUCTURE STUDIED HERE.

EXPERIMENT

Specimen preparation

The first step in the specimen preparation was to produce a very flat cross-section. It was anticipated from studies of other similar structures that the highest deformations would be perpendicular to the plane of lamination of the structure, that is, in the global z direction. Accordingly, the specimen device was sectioned perpendicular to the substrate. The section was potted in epoxy and prepared using metallographic-style procedures with extremely careful handling. At the end of the specimen preparation procedure, the epoxy was removed from 1

TABLE 1. NOMINAL THICKNESSES OF THE LAYERS IN THE HDI STRUCTURE TESTED HERE.

Layer	Thickness, μm
Substrate metallization (Al)	4
Interlayer adhesives	11
Polyimide	21
Upper-layer metallization:	
Ti	0.1 - 0.15
Cu	4
Ti	0.1 - 0.15

or more sides of the specimen, so that neither specimen was completely encased in epoxy. We used a series of SiC-coated papers with grit sizes ranging from 260 to 5 μm to grind the specimen to a thickness of 3 mm or less to produce a smooth surface with vias visible. Final polish was obtained with 3- and 1-μm natural diamond aerosol spray. The surface of the specimen was swabbed with methanol. The specimen was cleaned in a methanol ultrasonic bath for 30 s, and, finally, the surface was scrubbed with acetone on soft sterile cotton. Within 2 h of the final polish and cleaning, the specimen was sputter-coated with AuPd.

Preparation of line gratings on cross sections of HDI was accomplished using electron-beam lithography. Because of the novelty of the technique, a brief summary is given. Two percent polymethyl methacrylate (PMMA) in chlorobenzene solution was used as a positive electron-sensitive resist (Haller, 1968). The specimens were spin-coated with PMMA at 2000 rpm and baked for 60 min at 170 °C to cure the PMMA. The final thickness of the PMMA was 150 nm or less. To prevent degradation of the resist, line gratings were written on the specimens within a few hours of the curing of the PMMA. After exposure the specimen was developed in a 3:1 solution of isopropanol (IPA) and methyl isobutyl ketone (MIBK) for 40 s. This was followed by a 20 s rinse in IPA and a 30 s rinse in deionized water. Finally, the specimen was sputter-coated with AuPd, to provide a thin (5 nm) conductive layer.

The SEM has been used to write line gratings ranging in size from 60 to 1200 μm. Figure 2 is a photomicrograph of lines written on a sample of silicon. These lines have a pitch of 160 nm. The dark stripes are trenches in the PMMA, produced where the electron-beam exposure causes unlinking of the PMMA molecules, so they are preferentially dissolved by the developing solution. The brighter regions adjacent to the dark trenches are ridges. Figure 2 shows that the line profile as imaged by the SEM is not a simple square wave. The line corners show up more intensely than the line centers or the spaces. This complex profile reappears in the moiré fringes.

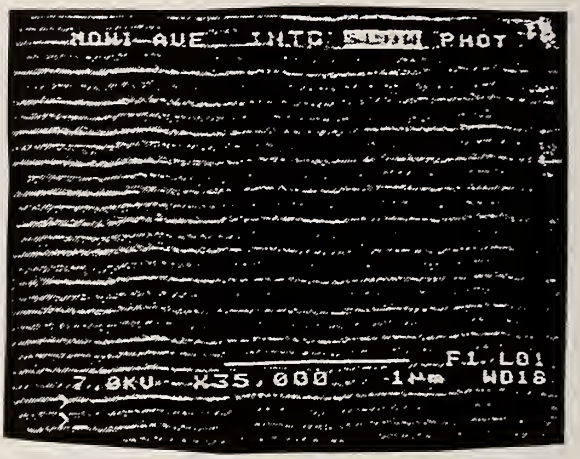

FIGURE 2. SEM MICROGRAPH OF A LINE GRATING WITH A PITCH OF 160 NM, ON SILICON.

In this study we used gratings of 512 lines with pitches of 175 and 350 nm. We always wrote lines parallel to the HDI surface to enable us to measure the z-direction (out-of-plane) deformation. The two directions in the cross-section plane are x and z. The time required to write each grating varied from 4 to 22 min. The parameters for these line gratings are listed in Table 2. Specimen HDI 1 has one via starting on the substrate, and specimen HDI 2 has two vias on higher layers of the structure. Figures 3 and 4 show the configuration of the regions studied.

Recording of Moiré Fringe Patterns

To observe thermally-induced displacements, we mounted the specimen on a heating stage within the SEM, as shown in Figure 5. The stage is rated for temperatures up to 1000 °C, but we have used it only up to 180 °C. The stage and heater were carefully grounded to avoid distortion of the SEM image. One thermocouple was mounted on the heater chip, and a second was attached between the specimen clamp and the specimen. We focussed the microscope on the selected line grating at a magnification that produced moiré fringes. Because the magnification of our microscope is adjustable only in discrete steps, we were unable to produce a null field (an exact match between the line pitch and the pitch of the rastered electron beam). We started our experiments with about 3 carrier fringes present. Figures 6 and 7 show the initial moiré fringe patterns. For the specimens in this paper, thermal expansion corresponded to increased fringe density. We took photographs of the SEM display, and we also recorded the images digitally. The computer stores the images as 480 lines of 512 8-bit pixels.

The electrical power to the heater was manually controlled. We heated the specimen to temperature, waited for equilibrium, and recorded the moiré fringe pattern. The recording of an image required about 30 s. Because the moiré fringe spacing would be affected if the specimen were moving during the recording of the image, we recorded images only after making sure that the motion had stopped by observing an individual line of the grating at high magnification. Reaching equilibrium sometimes required 30 minutes or more.

.BLE 2. EXPERIMENTAL CONDITIONS.

Specimen	HDI 1	HDI 2
Magnification	1100	550
Grating lines in frame	480	480
Grating pitch, nm	175	350
Temperatures studied, C	23, 51, 87, 122, 151	22, 41, 70, 98, 123, 144
Maximum temperature change, C	128	122
Vias in frame	1	2

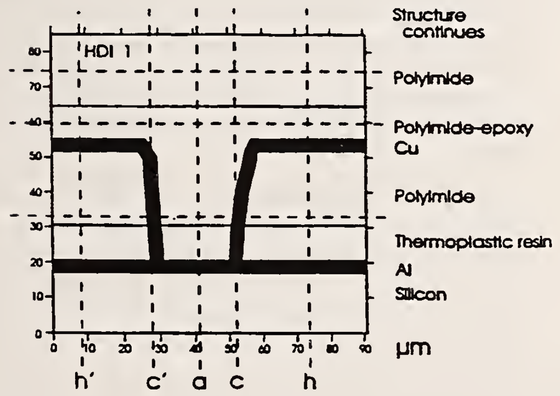

GURE 3. TRACING OF VIA ON SPECIMEN HDI 1, HOWING SIZE SCALE, STRUCTURAL FEATURES, ND PATHS AND LOCATIONS FOR STRAIN RESULT .OTS.

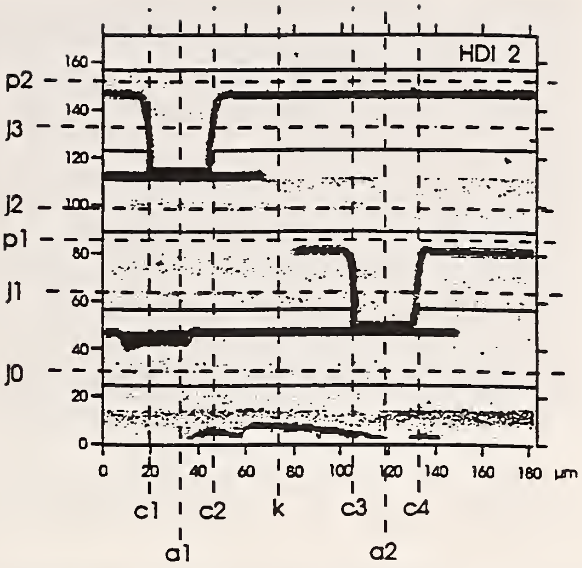

FIGURE 4. HIGH-CONTRAST RENDERING OF SEM MICROGRAPH OF VIA ON SPECIMEN HDI 2, SHOWING SIZE SCALE, STRUCTURAL FEATURES, AND PATHS AND LOCATIONS FOR STRAIN RESULT PLOTS.

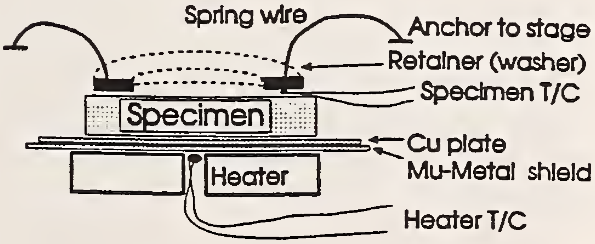

FIGURE 5. SCHEMATIC DRAWING OF THE HEATING STAGE USED WITH THE SEM.

ta Reduction

)ata reduction was begun by manually tracing the fringes to duce a list of (x, z) pairs giving the locus of each fringe.)sequent calculations of displacement and strain as functions of ;ition were automated. Spline fitting was used to interpolate ge numbers from the traced points to a regular grid and to :ulate strains from displacements. At each temperature we ained the z-direction displacement w as a function of x and z hin the field of observation. From these data we calculated the normal strain in the z direction, as $\varepsilon_{zz} = \partial w/\partial z$. This ;in is available as a function of x and z.

)btaining displacement information between moiré fringes uires either some way to measure partial fringes or interpolation. Partial fringes could not be measured here, so interpolation was used. Fractional fringe number was interpolated from about 10 actual fringes in the frame at the highest strains to a total of 25 positions. The strain was tabulated at the same number of positions in the X-direction. The results would not have changed significantly had a different level of detail been chosen. Therefore, the experimental results consisted of a set of 625 total z-direction strain values at each temperature. The starting temperature, 22 or 23 C, was considered to be a zero-strain temperature, so all strains reported here are the difference between the strain at temperature and the strain at room temperature.

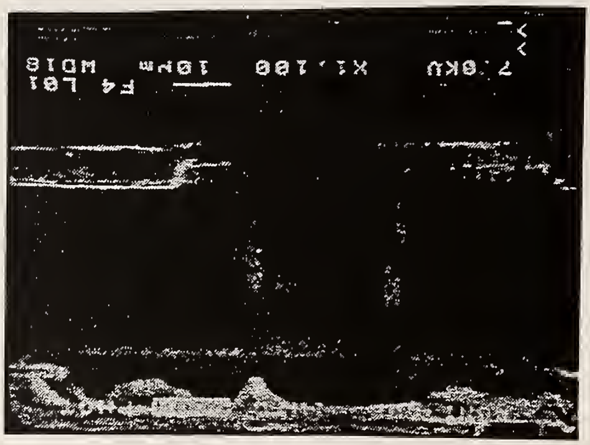

FIGURE 6. MOIRÉ FRINGE PATTERN OF VIA HDI 1. INITIAL CONDITION AT 24 °C, BEFORE HEATING. THE VIA IS SHOWN RIGHT-SIDE-UP.

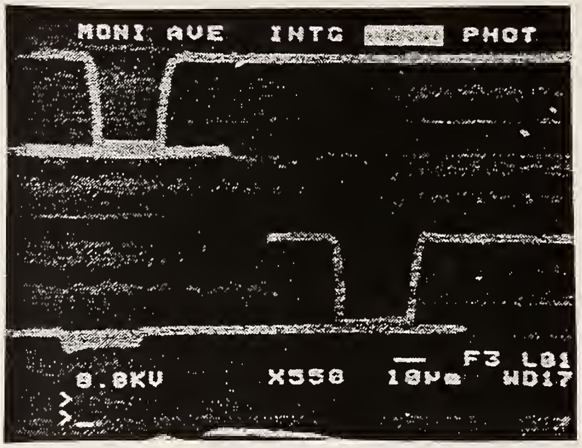

FIGURE 7. MOIRÉ FRINGE PATTERN OF VIA HDI 2. INITIAL CONDITION AT 22 °C, BEFORE HEATING.

MODELING

Two-dimensional Plane Stress Finite Element Model of HDI Via

A two-dimensional plane stress finite element model of the tested via structure was developed to compare with the axial strain results derived from the electron beam moiré data. The sectioned or cut surface of the via structure on which in-plane displacements were measured is a free surface. Therefore near-plane-stress conditions exist on the cut surface.

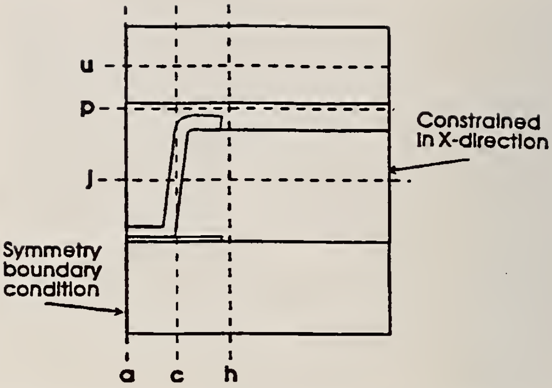

FIGURE 8. VIA AS MODELED BY FINITE ELEMENT ANALYSIS, SHOWING PATHS FOR STRAIN RESULT PLOTS.

The finite element model geometry was constructed to match as closely as possible to specimen HDI 1. Although the via in specimen HDI 1 appears slightly asymmetric about its center, symmetry was assumed through the application of symmetry boundary conditions at the left side of the finite element model of the via as shown in Figure 8. The right side of the via was constrained to have zero displacement in the x-direction. This boundary condition is consistent with the fact that the HDI layer is in reality attached to a rigid ceramic substrate with a low thermal expansion coefficient which constrains the motion of this surface.

The mesh consisted of mainly eight-noded, quadratic quadrilateral isoparametric elements with some transition six-noded quadratic triangular elements. The copper barrel (the near-vertical side wall of the via) where yielding was expected was modeled by only undistorted eight-noded quadrilateral elements. The model consists of approximately 1000 elements and 6000 total degrees of freedom. A mesh convergence study indicated convergence in the total strain range in the copper barrel with this mesh which consists of four elements through the thickness of the copper barrel.

Temperature-dependent, nonlinear elastoplastic material properties were employed for the copper and polymers. The same set of property values documented by Prabhu *et al.* (1995) was used here, except that the copper properties were provided separately (Johnson, 1995). The titanium passivation layer in the trilayer metallization was assumed not to affect the mechanical properties. The basic properties used are listed in Table 3. Additional details were given by Prabhu *et al.* (1995).

Perfect adhesion was assumed at all material interfaces. Note that orthotropic coefficient of thermal expansion (CTE) properties were used to model the polymer materials. However, since no orthotropic material property data could be found for the various modulus of elasticity and Poisson's ratio for the copper and polymers, isotropic conditions were assumed for these properties. However, the values used were "thin-film" in-plane values. This leads to the possibility of errors introduced due to incorrect values for these properties in the out-of-plane direction.

TABLE 3. MATERIAL PROPERTIES USED IN ANALYSIS OF HDI STRUCTURE.

Material	Young's Modulus, GPa	Coefficient of thermal expansion, 10^{-6} / C	
		In-plane	Out-of-plane
Alumina	275	7.0	7.0
Silicon	190	2.5	2.5
Copper	43	17.0	17.0
Thermo-plastic resin At 23 C At 100 C	 4.0 2.9	 56.0 56.0	 29.0 29.0
Polyimide At 23 C At 100 C	 5.0 4.0	 20.0 20.0	 112.0 112.0
Thermoset adhesive	4.0	40.0	85.0

Loading consists of multiple uniform-temperature load steps beginning at 23 C and increasing to 122 C. The application of a uniform temperature at each load step implies that the transient effects that produce temperature gradients in the via structure are negligible. Previous work has shown this to be indeed true for the relatively slow thermal cycling loading conditions due to the large surface/volume ratio for the HDI layer and MCMs in general (Prabhu *et al.*). The automatic load stepping algorithm required nine load steps to reach 120°C beginning at 23°C and using an initial load substep of 20 °C.

RESULTS and DISCUSSION

Moiré fringe patterns taken at 150°C are shown in Figures 9 and 10. Comparison with the initial fringe patterns, shown earlier, indicate that the fringe patterns have clearly changed. The strains as measured by electron beam moiré are displayed as contour plots in Figures 11 and 12.

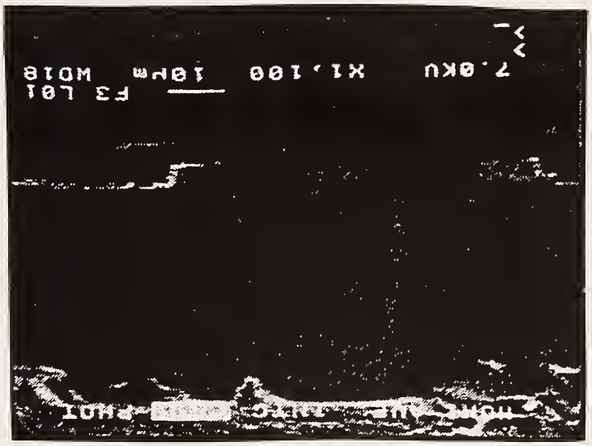

FIGURE 9. MOIRÉ FRINGE PATTERN OF VIA HDI 1. AT 151 °C, THE HIGHEST TEMPERATURE REACHED IN THIS EXPERIMENT.

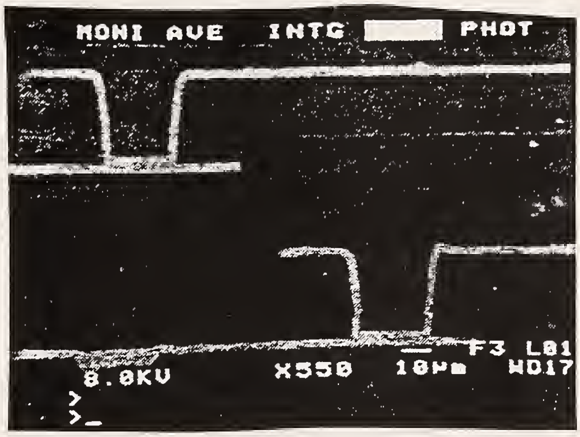

FIGURE 10. MOIRÉ FRINGE PATTERN OF VIA HDI 2. AT 144 °C, THE HIGHEST TEMPERATURE REACHED IN THIS EXPERIMENT.

The analysis focussed on the strains near 120°C, because this was the highest temperature where material property data for the polyimide-epoxy adhesive layer have been reported. A contour plot showing the total out-of-plane strain as a function of position is displayed in Figure 13.

The experiment and analysis are compared in plots of strain *versus* position along selected paths, and in plots of strain *versus* temperature at selected locations. Figures 3, 4, and 8 show the paths and locations used. Plots of strain against position are shown in Figures 14-18; plots of strain against temperature, for the experiment only, are shown in Figures 19 and 20.

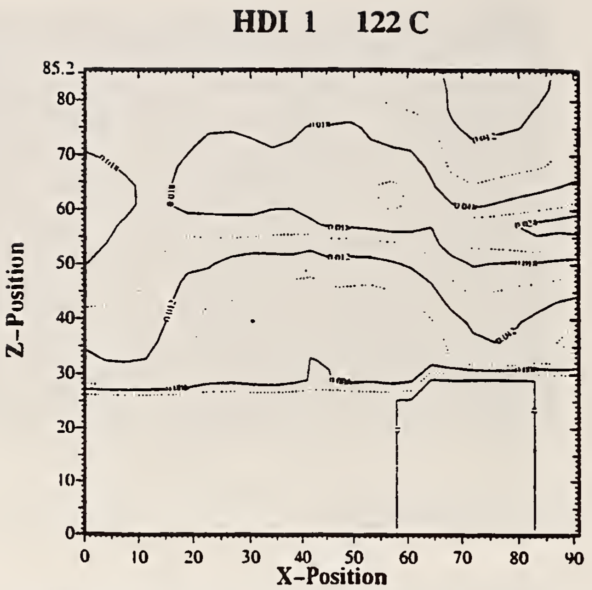

FIGURE 11. CONTOUR PLOT OF MEASURED OUT-OF-PLANE STRAINS AROUND VIA HDI 1 AT 122 °C.

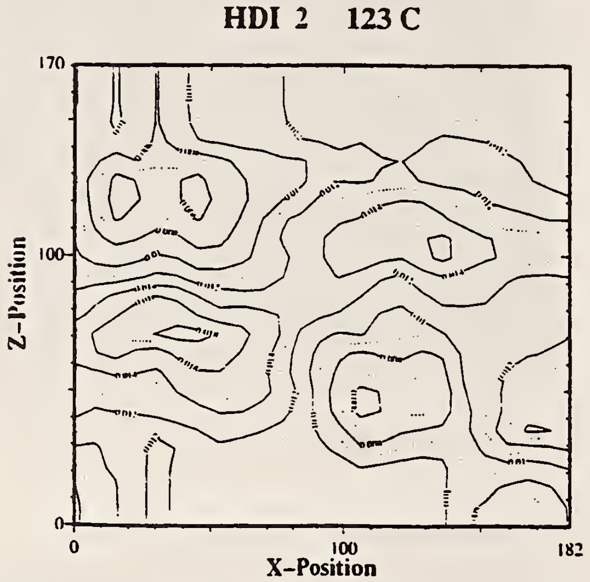

FIGURE 12. CONTOUR PLOT OF MEASURED OUT-OF-PLANE STRAINS AROUND VIAS IN SPECIMEN HDI 2 AT 123 °C.

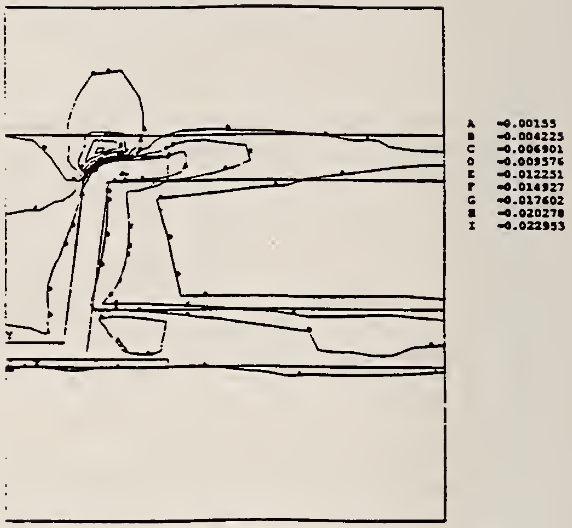

FIGURE 13. CONTOUR PLOT OF OUT-OF-PLANE STRAINS CALCULATED BY FINITE ELEMENT ANALYSIS, CORRESPONDING TO 120 °C

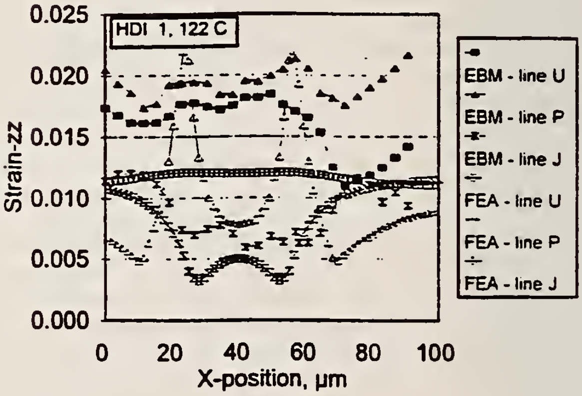

FIGURE 14. MEASURED AND PREDICTED OUT-OF-PLANE STRAINS AROUND VIA HDI 1 PLOTTED ALONG PATHS j, p, AND u AT 122 °C.

The general character of the total z-direction strain in this interconnect structure is that the strain within the vias and in the via walls is lower than the strain in the polyimide away from the vias. Both the experimental mechanics results and the analysis showed this general character. In the polyimide layers at 120°C, away from the vias and away from delaminations discussed below, the total normal strain in the z-direction averaged about 1.2 percent in the experiment, while the analysis gave a value of 1.1 percent. This experimental value can be seen in the plots of Figure 14 (EBM-line j), Figure 15 (all lines, at the highest z-

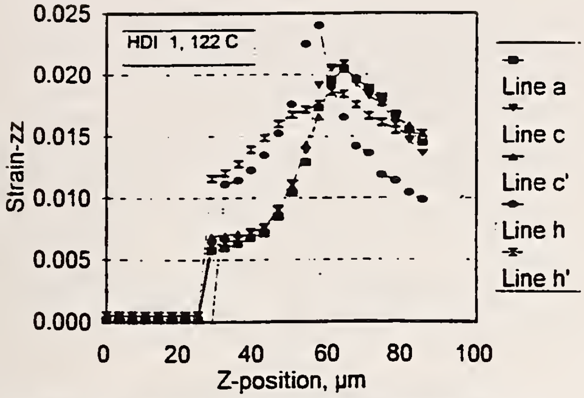

FIGURE 15. OUT-OF-PLANE STRAINS AROUND VIA HDI 1 PLOTTED ALONG PATHS a, c, c', h, AND h' AT 122 °C.

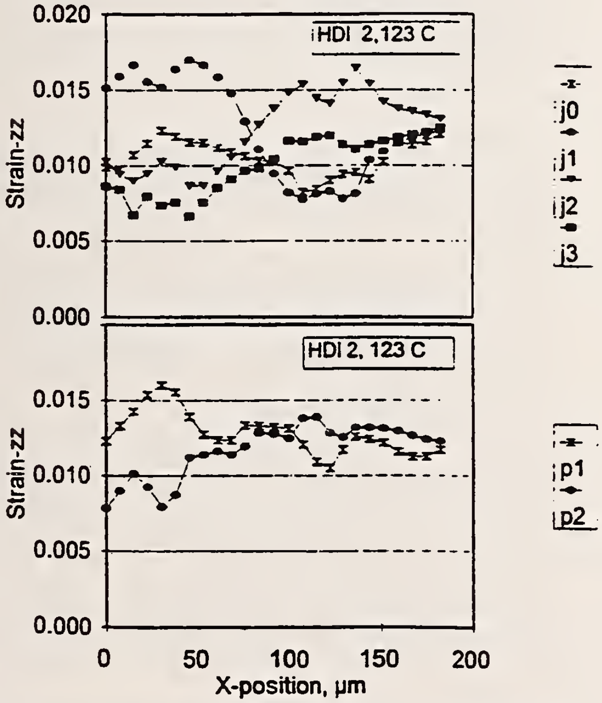

FIGURE 16. OUT-OF-PLANE STRAINS AROUND VIA HDI 2 PLOTTED ALONG PATHS HORIZONTAL PATHS p1 AND p2 AND j0, j1, j2, AND j3 AT 123 °C.

values), Figure 16a (at the highest x-values), and Figure 18 (outside the vias). The model value can be seen in Figure 14 (FEA-u and j) and Figure 17 (highest z-values). This excellent agreement is taken as evidence for two points: first, that the material properties used for the polyimide layers are correct; and second, the strains were being measured correctly.

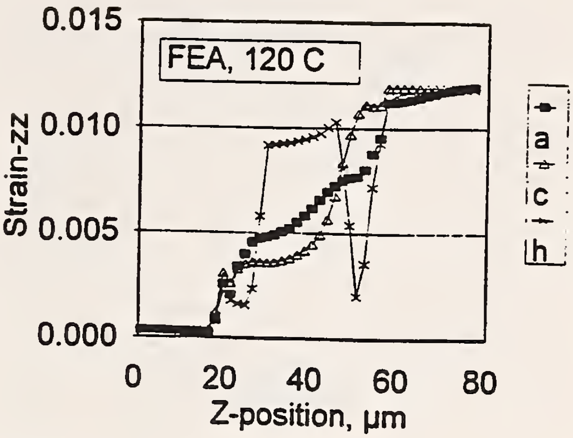

FIGURE 17. OUT-OF-PLANE STRAIN PREDICTED BY THE REFERENCE FINITE ELEMENT MODEL, PLOTTED ALONG PATHS a, c, AND h, FOR A TEMPERATURE OF 120 °C.

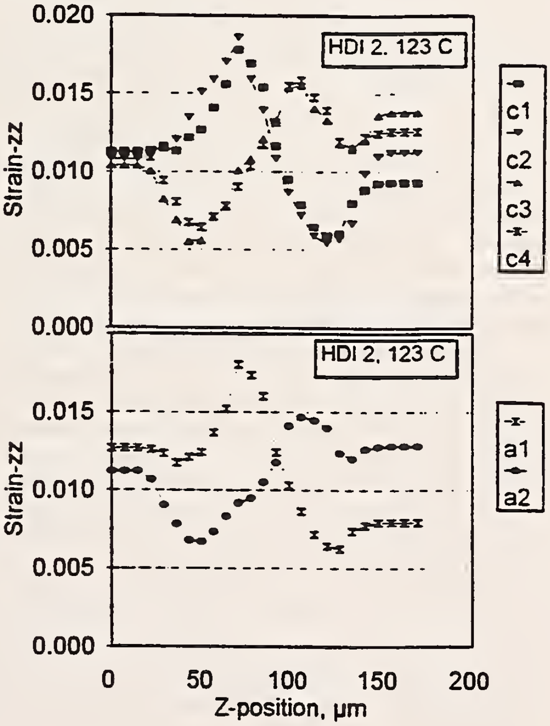

FIGURE 18. EXPERIMENTALLY MEASURED OUT-OF-PLANE STRAINS AROUND VIA HDI 2 PLOTTED ALONG VERTICAL PATHS a1 AND a2 AND c1, c2, c3, AND c4 AT 123 °C.

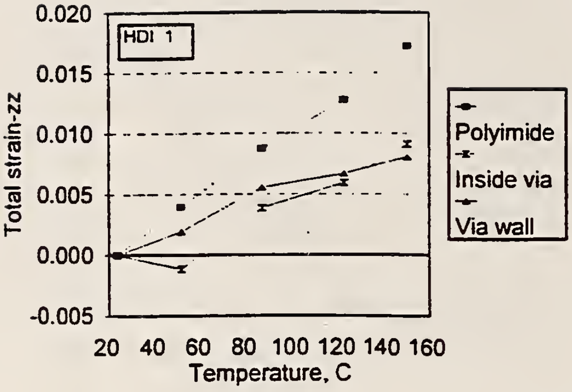

FIGURE 19. OUT-OF-PLANE STRAIN PLOTTED AGAINST TEMPERATURE AT THREE LOCATIONS FOR SPECIMEN HDI 1.

It was initially suspected that the use of isotropic elastic stiffnesses for the thin polymer layers in this structure might introduce incorrect values for these properties in the out-of-plane direction. In particular, one would expect a significantly smaller modulus of elasticity in the out-of-plane direction for the polymers due to the alignment of the long molecules in the plane of the thin polymer layers. In essence, one would expect the alignment of long polymer molecules in the plane to produce the opposite effect in Young's modulus as in the coefficient of thermal expansion: larger in-plane E, smaller out-of-plane E value. Thus, our finite element model based on in-plane E .values would have been elastically too stiff in the out-of-plane direction.

Fairly good quantitative agreement between analysis and experiment was found regarding the strain inside the vias. In Figure 14 in the center of the via (lines j) the strain was measured at 0.6%, while the FEA model predicted the strain to be 0.5%. However, the analysis predicted a sharp dip in the strains across the copper via wall thickness to a value of 0.3% at the wall. This was not observed in the experimental results. The predicted low strain in the copper arose from the much higher stiffness and lower thermal expansion coefficient of the copper compared to the surrounding polymers. The results from HDI 2, in figure 16, show the same results as HDI 1, that is, the predicted low strains in the copper were not found. It is possible that the discrepancy is due to the difficulty of detecting local regions of low strain with the electron beam moiré technique. Additional experiments may clarify this point. This is an important issue, because the strain in the copper has a significant effect on the lifetime. Other possible causes of this discrepancy include problems with the material properties of the copper and three-dimensional effects on the actual via structures not included in the two-dimensional analysis considered here.

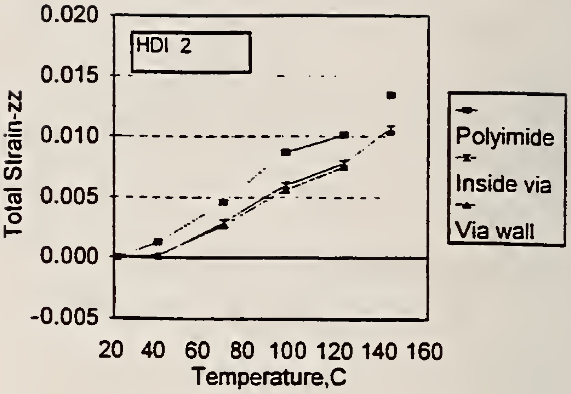

FIGURE 20. OUT-OF-PLANE STRAIN PLOTTED AGAINST TEMPERATURE AT THREE LOCATIONS FOR SPECIMEN HDI 2.

Laminations

The experimental data showed some regions of high strains at the adhesive lamination between polyimide layers. The highest strains observed were 0.036 in HDI 1 at 151°C and 0.028 in HDI 2 at 144°C. These regions of high strain are also evident in the moiré fringe patterns, Figures 11 and 12. However, the specimens were cross-sections. The cross-sectioning process could have damaged the interconnect structure, leading to the high observed strains. High strains were not seen near vias which pass through the lamination region. The high strains show the capability of the technique to detect localized regions of high strain.

The situation for localized regions of low strain is different. For the conditions of these experiments, regions of low strains are regions of low fringe density, which means that a region of low strain that is localized in the z-direction, but lies along the x-direction, may be difficult to detect. This is believed to be the case with the Cu traces away from the vias. In Figure 17, line h shows a significant dip in the strain at the Cu trace. The comparable experimental plots, such as figure 15, lines h and h', do not show the dip. Here the conclusion is that the experiment was incapable of resolving the localized low strains in the Cu layer.

There are two remaining significant discrepancies between the experiment and the analysis beyond the strains in the vias discussed above. First, the analysis does not have regions of high strains along the laminations; these were observed in both experiments. They are evident in all the traces in Figure 15, at around z = 60 μm. Second, the analysis has very local regions of high tensile strain, up to 0.023 at 120 °C, just above the via wall (Figure 14). Only very attenuated hints of these "strain spikes" could be found in the experimental data. This difference is interpreted as follows. The delamination strains are the result of some damage or imperfection in the structure; this damage was not considered in the analysis. The possibility that this damage was created during specimen preparation was noted above. It is believed that the "strain spikes" seen in the analysis are a correct result for the configuration analyzed, but are not present in the experimental data because they have been relieved by the delamination strains. The effect of this is that the highest strains seen in the experiment at 120 °C, which were 0.027 in HDI 1 and 0.019 in HDI 2, seem to bracket the highest strains in the analysis, which were 0.023, from Figure 14, FEA-line p. However, in the analysis these strains occur in a very small area, right above the via wall, whereas in the experiment the high strains are spread along the lamination, and the highest experimental values occur away from vias, rather than over the via wall.

Is There a "Worst Case"?

The highest strains observed in this experiment were 0.036 in HDI 1 at 150 °C and 0.028 in HDI 2 at 144 °C. These strains occurred locally along the polyimide-epoxy bond between polyimide layers, where no metallization was present. Clearly, these high strains may have been the result of damage done to the structure during specimen preparation. Much lower strains, around 0.006 experimentally and 0.003 analytically, were seen at the via walls, where the bond between the polyimide layers is reinforced by the copper via wall.

Prabhu *et al.* derived "worst case" strains by postulating a stress concentration of 3 in a plastic region and applying Neuber's rule. Their "worst case" strains were about 0.015 for a temperature change of 130°C. Using these strain levels, they derived a predicted fatigue life ranging from 1000 cycles during severe temperature cycling to over 100,000 in typical application environments.

The significance for complete devices of the highest strain values seen in the present experiment cannot be assessed based on the experiments and analysis in this study, because the strains might have resulted from damage during specimen preparation and because near-plane-stress behavior is being observed on the free surface, while the actual structure is subject to full three-dimensional stress fields. In a subsequent paper we will show that both axisymmetric and three-dimensional finite element models predict a significant concentration of strain in the via barrel for a via completely embedded in the surrounding structure. Therefore, "worst case" strains cannot be derived directly from the present results. The present results do suggest that high strains can occur at the laminations between polyimide layers. However, no information can be deduced concerning the mode or degree of damage which might occur in other types of tests, such as thermal cycling of intact devices. The present results do suggest that nondestructive examinations of the bonding between layers of the HDI structure at intervals during thermal cycling tests may be useful in understanding the observed device lifetimes.

Lessons Learned

Experimental analyses of advanced electronic interconnect structures offers some opportunities and challenges not present in analogous experiments on macroscopic structures. Whole advanced interconnect structures can be placed under an optical microscope, or within the chamber of a SEM. Loading can be done using a heating stage.

The most obvious challenge is the need for strain observation in very small regions. This challenge was met by the choice of electron beam moiré as the experimental technique. The additional important challenge revealed by this study was the difficulty of accounting for the effects of specimen preparation on the measurement results. Ideally, finite element analysis can account for the direct geometrical effect of cross-sectioning on the stresses and strains. However, undetectable local damage may be produced during specimen preparation. The prepared cross-section may not behave exactly like the intact device. Additional examinations, beyond those customary in experimental mechanics studies of macroscopic structures, may be needed in order to verify the condition of the specimen after cross-sectioning and surface preparation.

SUMMARY and CONCLUSIONS

There was sufficient agreement, both qualitative and quantitative, between the experiments and the analyses done in this study to allow the conclusion that both the experimental results and the analytical results are generally correct. That is, the analysis correctly simulates the model via, and the experiment correctly describes the behavior of the specimens. A convincing point of agreement was that the strain in the polyimide layers away from all other features was about 0.012 in the experiment and 0.011 in the analysis.

A qualitative discrepancy between experiment and analysis was that, while both gave nearly the same maximum strain, this strain was found in different locations. In the experiment regions of high strains extend along approximately one third of the total length of lamination between polyimide layers; in the analysis, the high strains are localized above the via walls. This discrepancy was attributed to damage or incipient delaminations in the specimen cross-sections, possibly but not necessarily produced during specimen preparation.

Quantitative agreement was found regarding the strains inside the vias. In both the experiment and the analysis, the strains in the vias are half or less of the strains in the surrounding polyimide. The values were 0.005 in the analysis and 0.006 in the experiment. However, in the analysis the lowest strains are in the Cu via walls, at about 0.003, while in the experiment the strains in the via walls, are about 0.006. The possibility that the experimental technique was inadequate to spatially resolve these strains remains, along with two additional possibilities: problems with the material property values used in the analysis, and three-dimensional effects not considered in the two-dimensional model used here. Increasing the model value of out-of-plane stiffness of the polymer layers would also reduce this discrepancy.

Two big problems with the experimental technique were related to specimen preparation. One was the difficulty of producing perfect line gratings, which is related to the difficulty of producing flat surfaces on this heterogenous HDI structure that includes both very hard ceramic and much softer polymers. The other problem was the difficulty of avoiding damaging the delicate interconnect structure, especially when it is laminated to a hard alumina substrate. Additional non-destructive examination of structures of this sort during thermal cyeling might be capable of resolving the issue of what degree of delamination, if any, is found in the intact structures. Another problem with the experiment was found to be inability to detect small regions of low strains. Use of a higher density of initial fringes, as carrier fringes, might solve this problem, but might also make data reduction more difficult.

REFERENCES

Choi, H.-C., Guo, Y., LaFontaine, W., and Lim, C.K., 1993, "Solder Ball Connect (SBC) Assemblies under Thermal Loading: II. Strain Analysis Via Image Processing, and Reliability Considerations," *IBM Journal of Research and Development*, Vol. 37, pp. 649–659.

Corbin, J.S., 1993, "Finite Element Analysis for Solder Ball Connect (SBC) Structural Design Optimization," *IBM Journal of Research and Development*, Vol. 37, pp. 585–596.

Dally, J.W., and Read, D.T., 1993, "Electron Beam Moiré," *Experimental Mechanics*, Vol. 33, pp. 270–277.

Fillion, Ray, Wojnarowski, Robert, Gorcyzca, Tom, Wildi, Erie, and Cole, Herb, 1994, "Development of a Plastic Encapsulated Multichip Technology for High volume, Low Cost Commercial Electronics," *1994 Proceedings, 44th Electronic Components & Technology Conference*, edited by Iwona Turlik and Rao Tummala, Institute of Electrical and Electronics Engineers, New York, pp. 805-809.

Guo, Y., Lim, C.K., Chen, W.T., and Woyehik, C.G., 1993, "Solder Ball Connect (SBC) Assemblies under Thermal Loading: I. Deformation Measurement Via Moiré Interferometry, and Its Interpretation," *IBM Journal of Research and Development*, Vol. 37, pp. 635–648.

Haller, I., Hatzakis, M. and Srinivasan, R., 1968, "High Resolution Positive Resists for Electron-Beam Exposure," *IBM Journal Research and Development*, Vol. 12, pp. 251–256.

Han, B., Guo, Y., and Lim, C.K., 1994, "Applications of Moiré and Microscopic Moiré Interferometry to Electronic Packaging Product Development," *Conference Proceedings of the 4th Annual IEEE Dual-Use Technologies and Application Conference*, Rome, NY (in press).

Johnson, Erie, 1994, private communication.

Kishimoto, S., M. Egashira, Shinya, N. and Carolan, R.A., 1991, "Local Micro-Deformation Analysis by Means of Microgrid and Electron Beam Moiré Fringe Method," *Proceedings of the Sixth International Conference on Mechanical Behavior of Materials*, Vol. 4, M. Jono and T. Inoue, Eds., Kyoto, Japan, pp. 661–666.

Kishimoto, S., Egashira, M. and Shinya, 1991, "Measurement of Grain Boundary Sliding and Observation of Microgrids for High Temperature Use," *Journal of the Society for Materials Science Japan*, Vol. 40, pp. 637–641 (in Japanese).

Lau, J., and Erasmus, S., 1993, "Review of Packaging Methods to Complement IC Performance," *Electronic Packaging and Production*, Vol. 33, No. 6, pp. 50–56.

MeDonach, A., McKelvie, J., and Walker, C.A., 1980, "Stress Analysis of Fibrous Composites Using Moiré Interferometry," *Optics and Laser Engineering*, Vol. 1, pp. 85–105.

MeNeill, S. R. , Sutton, M. A., and Turner, J. L., 1985, "Stress Analysis of a Reversed Dish Head of a Cylindrical Pressure Vessel, *International Journal of Pressure Vessels and Piping*, Vol. 18, pp. 81-90.

National Technology Roadmap for Semiconductors, Semiconductor Industry Association, 1994, pp. 20-21.

Parks, V.J., 1987, "Geometric Moiré," *Handbook on Experimental Mechanics*, A.S. Kobayashi, Ed., Prentice-Hall, Englewood Cliffs, N.J., pp. 282–313.

Post, D., 1980, "Optical Interference for Deformation Measurements—Classical, Holographic and Moiré Interferometry," *Mechanics of Nondestructive Testing*, W.W. Stinehcomb, Ed., Plenum Press, New York, pp. 1–53.

Post, D., 1991, "Moiré Interferometry: Advances and Applications," *Experimental Mechanics*, Vol. 31, pp. 276–280.

Post, D. and Wood, J. D., 1989, "Determination of Thermal Strains by Moiré Interferometry," *Experimental Mechanics*, Vol. 29, pp. 318–322.

Prabhu, Ashok S., Barker, Donald B., Pecht, Miehael G., Evans, John W., Grieg, William, Bernard, Edward S., and Smith, Eric, 1995, "A Thermo-Mechanical Fatigue Analysis of High Density Interconnect Vias," *Advances in Electronic Packaging 1995*, Vol. 1, American Society of Mechanical Engineering, New York, pp. 187-216.

Read, D.T., and Dally, J.W., 1993, "Local Strain Measurement by Electron Beam Moiré," in *Advances in Electronic Packaging 1993, EEP-Vol. 4-1, Proceedings of the 1993 ASME International Electronics Packaging Conference*, P.A. Engel and W.T. Chen, Eds., ASME, New York, pp. 163–169.

Read, D.T., and Dally, J.W., 1994, "Electron-Beam Moiré Study of Deformation of a GFRP Composite," *Journal of Applied Mechanics*, Vol. 61, pp. 402-409..

Theocaris, P.S., 1969, *Moiré Fringes in Strain Analysis*, Pergamon Press, Elmsford, N.Y.

Weller, R. and Shepard, B.M., 1948, "Displacement Measurement by Mechanical Interferometry," *Proceedings of the Society for Experimental Stress Analysis*, Vol. 6, pp. 35–38.

A6

Theory of Electron Beam Moiré

by Read and Dally (1996)

Volume 101, Number 1, January–February 1996
Journal of Research of the National Institute of Standards and Technology

[J. Res. Natl. Inst. Stand. Technol. 101, 47 (1996)]

Theory of Electron Beam Moiré

Volume 101 Number 1 January–February 1996

David T. Read

National Institute of Standards and Technology,
Boulder, CO 80303

and

James W. Dally

Mechanical Engineering Department, University of Maryland,
College Park, MD 20742

When a specimen surface carrying a high-frequency line grating is examined under a scanning electron microscope (SEM), moiré fringes are observed at several different magnifications. The fringes are characterized by their spatial frequency, orientation, and contrast. These features of the moiré pattern depend on the spatial frequency mismatch between the specimen grating and the raster scan lines, the diameter of the electron beam, and the detailed topography of the lines on the specimen.

A mathematical model of e-beam moiré is developed that expresses the spatial dependence of the SEM image brightness as a product of the local intensity of the scanning beam and the local scattering function from the specimen grating. Equations are derived that give the spatial frequency of the moiré fringes as functions of the microscope settings and the spatial frequency of the specimen grating. The model also describes the contrast of several different types of moiré fringes that are observed at different magnifications. We analyze the formation of these different fringe patterns, and divide them into different categories including natural fringes, fringes of multiplication, fringes of division, and fringes of rotation.

Key words: contrast; division; experimental mechanics; fringe; multiplication; pitch; rotation; spatial frequency; stress analysis.

Accepted: September 26, 1995

1. Introduction

When a specimen surface that carries a regular array of lines is examined under a scanning electron microscope (SEM), moiré fringes can be observed at several different magnifications. Some confusion can arise in the interpretation of the different fringe patterns, because the spatial frequency of the moiré fringes changes with mismatch, rotation, a multiplication phenomena, and a division phenomena. In this paper we first demonstrate these different fringe patterns, and then explain their formation based on a Fourier series representation.

Optical moiré fringes, either geometric or interferometric, are widely employed in experimental mechanics. The classical treatments of geometric moiré by Parks [1], Durelli and Parks [2], and Theocaris [3], and the descriptions of interferometric moiré by Post [4], Graham [5], and McKelvie [6] are most helpful in interpreting fringe pattern formation in e-beam moiré. However, certain features of the phenomenon of electron beam moiré were not anticipated in these classic treatments of optical moiré. These features result from the fact that in electron beam moiré, no actual reference grating exists. Instead, the electron beam raster scan replaces the reference grating.

The e-beam raster scan is similar in may respects to the video raster scan employed by Morimoto [7] in forming moiré fringes using low frequency specimen gratings. Kishimoto [8] recognized the similarity between the video and SEM raster scans and was the first to report the use of e-beam moiré fringes for experimental mechanics. However, neither Morimoto or Kishimoto discussed the many fringe patterns that may be observed when scanning lines are employed as the reference grating. With the controls available on a typical SEM it is possible to vary the e-beam diameter, the pitch of the raster scan, and the angle between the scan lines and the grating lines. All affect the fringe pattern.

We develop a mathematical model of e-beam moiré fringe formation that allows us to reproduce and extend certain results previously derived for optical moiré. The model is based on two postulates used in treatments of optical moiré [5]:

1. The spatial dependence of the pattern of the scan lines, and the spatial dependence of specimen grating, can be described using Fourier series.
2. The SEM image can be represented numerically as a set of intensity values given by the product of the scattering power of the specimen grating and the intensity of the scanning lines. Spatially extended interaction of the beam with the near-surface region of the specimen is incorporated as a contribution to the width of the scanning lines.

Based on these postulates, a model is derived that concisely describes natural moiré fringes, fringes of multiplication, and fringes of division. Experimental examples are demonstrated. The model is well-suited to determine the fringe contrast and the fringe shape as functions of the raster scan pitch, the scan line width, and specimen grating parameters.

2. Observation of Specimen Gratings and e-beam Moiré Fringes

Several high-density gratings, with spatial frequencies f_g^r of 2.5 μm^{-1} to 10 μm^{-1}, were written on a brass specimen using the methods described in [9]. A macroscopic view of the small areas written with different frequencies and different e-beam exposures is presented in Fig. 1. Examination of a grating with $f_g^r = 5\ \mu m^{-1}$ at high magnification, Fig. 2, shows the appearance of the grating lines on the specimen. Depending on the effectiveness of the process used to fabricate such lines, they may appear in the SEM display as high-contrast stripes of black and white, as shown in Fig. 2, or as low contrast stripes represented by intensity modulations in a gray field. Local imperfections in the specimen surface and in the grating produce irregularities in the brightness of the image. Additional imperfections are generated by the imaging process, even though the SEM image is recorded at a slow scan rate.

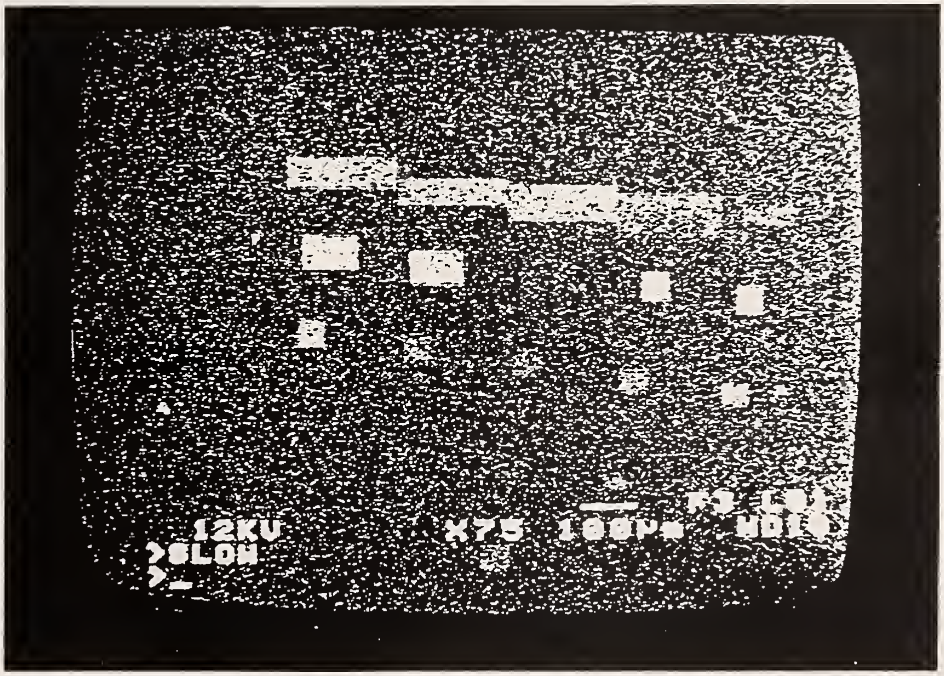

Fig. 1. Several line gratings written with different frequencies and exposures, on a brass specimen.

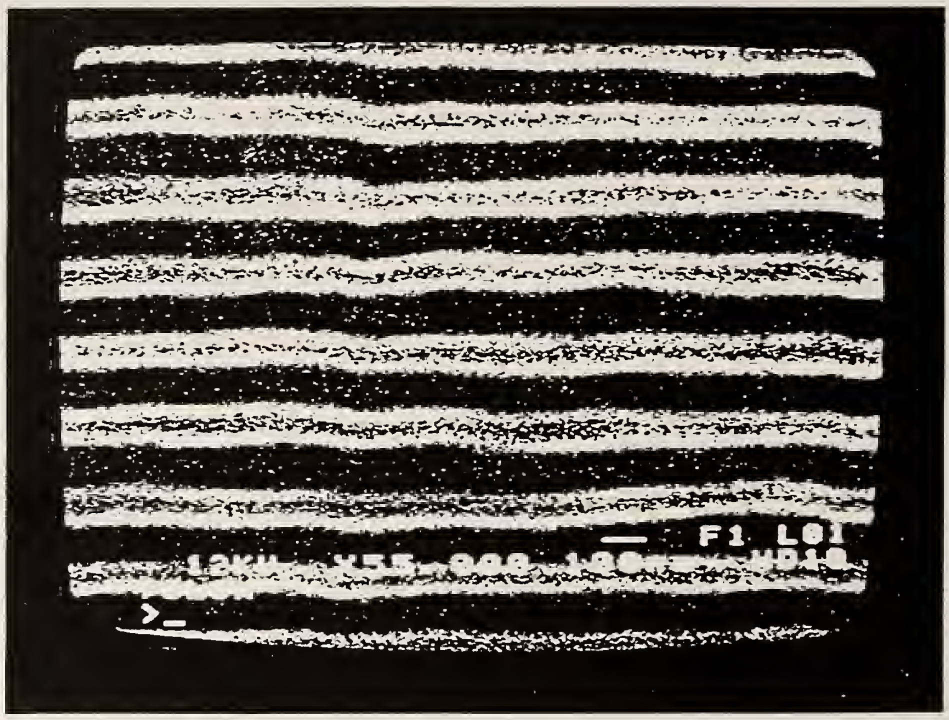

Fig. 2a. SEM image of a line grating with $p_g = 220$ nm, at a magnification of 55 000.

When a grating with $f_g^* = 5\ \mu\text{m}^{-1}$ is observed, moiré fringes appear at several different magnifications over the range 300 to 3000. Typical moiré patterns are illustrated in Figs. 3 to 5. We have divided these fringe patterns into three categories, based on the relative sizes of f_g^*, the spatial frequency of the specimen grating, and f_b, the spatial frequency of the raster scan. Moiré fringes of division, where $f_g^* > f_b$, are presented in Figs. 3a and 3b. Natural moiré fringes where f_g^* and f_b are nearly equal are shown in Figs. 4a to 4e. Most of these fringe patterns represent a slight mismatch between the pitch of the raster scan and the pitch of the grating; however, Fig. 4c represents nearly a perfect match. Moiré fringes of multiplication, first observed optically by Post [8], are also observed with e-beam moiré when $f_b > f_g^*$. Multiplication by two and three is illustrated in Figs. 5a and 5b.

3. Theory of e-beam Moiré Fringe Formation

We introduce a theory to describe the formation of the several different types of moiré fringes that are observed in an SEM. The theory is similar to that introduced to describe the formation of fringes in optical geometric moiré. Fourier series representations are used to describe the SEM raster scan, the specimen line grating, and the moiré fringes. The results are interpreted to explain the occurrence of fringes classified as natural, multiplied, and divided. The description of fringes of rotation is adapted directly from optical moiré.

3.1 The SEM Raster Scan System

The image observed in an SEM is produced by scanning the specimen grating with an e-beam raster scan. We locate a point in this image by its coordinates (x, y). The e-beam is scanned continuously across the imaged field in the x direction. The e-beam scan lines are equally spaced, with pitch p_b in the y direction. The magnified image, viewed on the CRT display, has a nominal size of 90 mm in the y direction. This dimension is related to a common photomicrograph size. The design of the SEM is such that the raster pattern is always aligned with the viewing screen and the camera frame, so in all the SEM images the x-axis is horizontal and the y-axis is vertical.

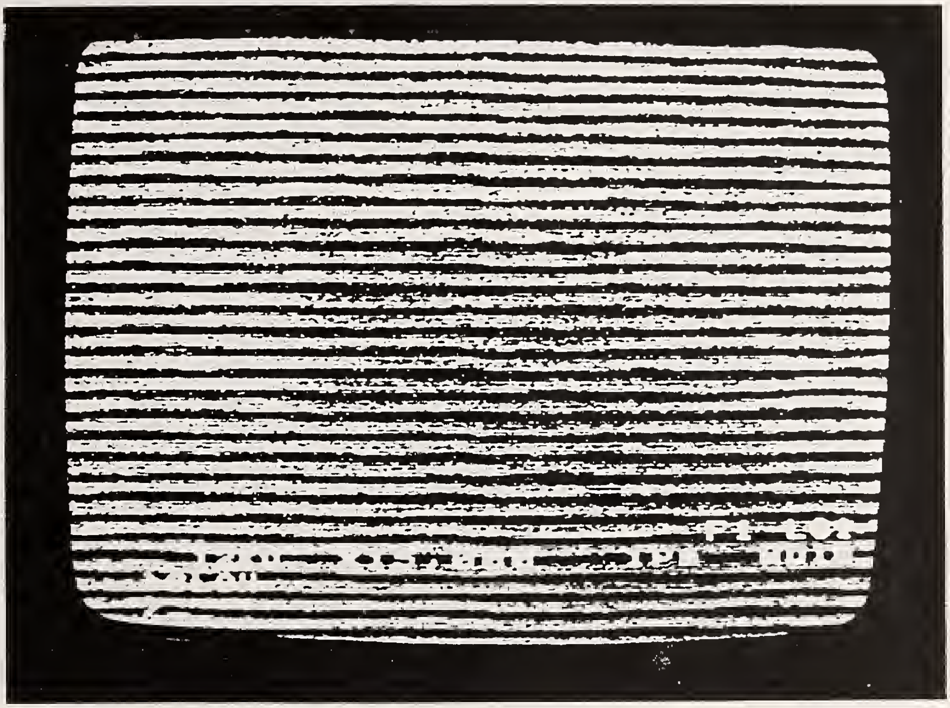

Fig. 2b. As in Fig. 2a, except at a magnification of 15 000.

Fig. 3a. Moire fringes of division on a 200 nm line grating, at a magnification of 330.

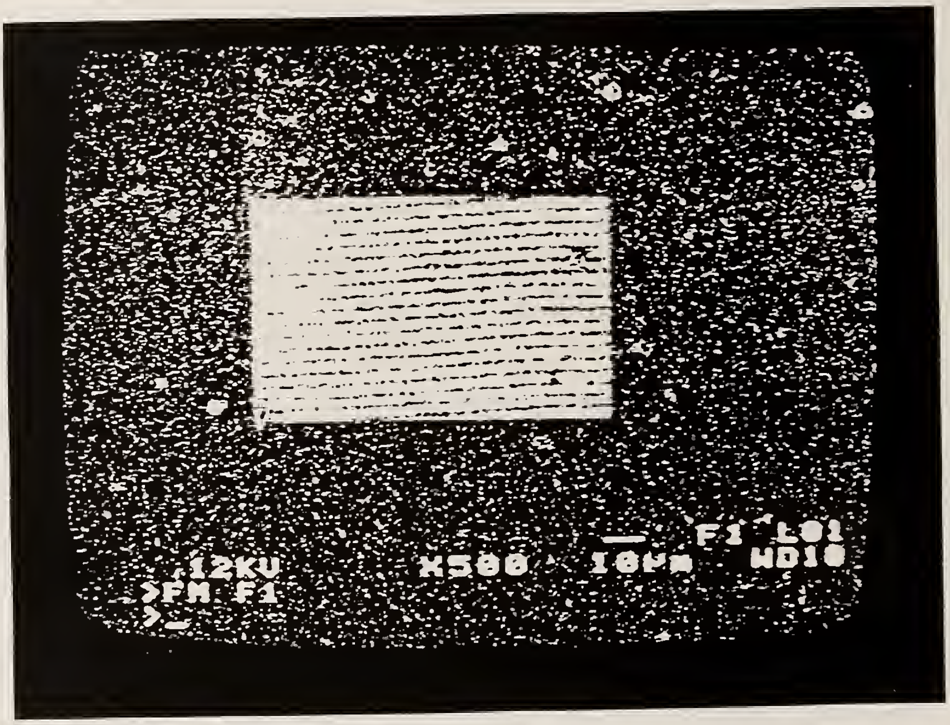

Fig. 3b. As in Fig. 3a except at a magnification of 500.

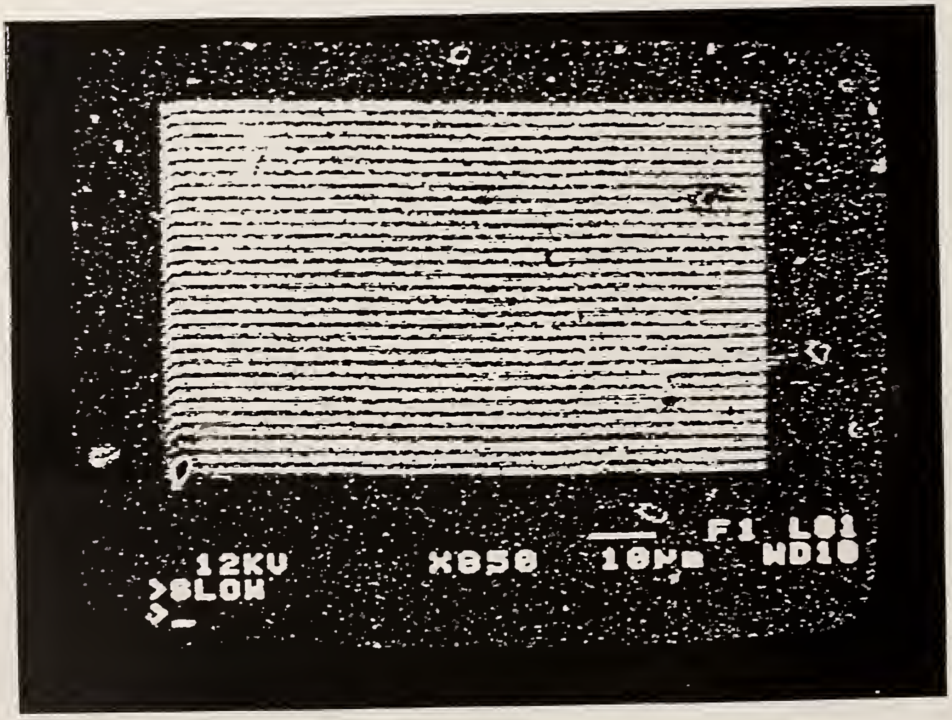

Fig. 4a. Natural moiré fringes with $p_f = 200$ nm, at a magnification of 950.

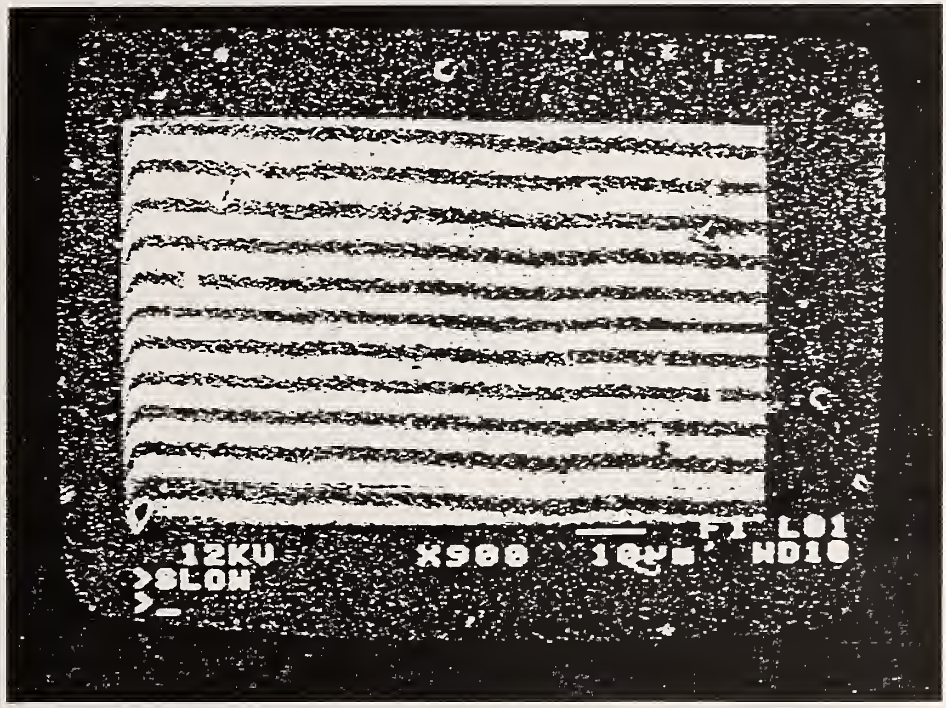

Fig. 4b. As in Fig. 4a except at a magnification of 900.

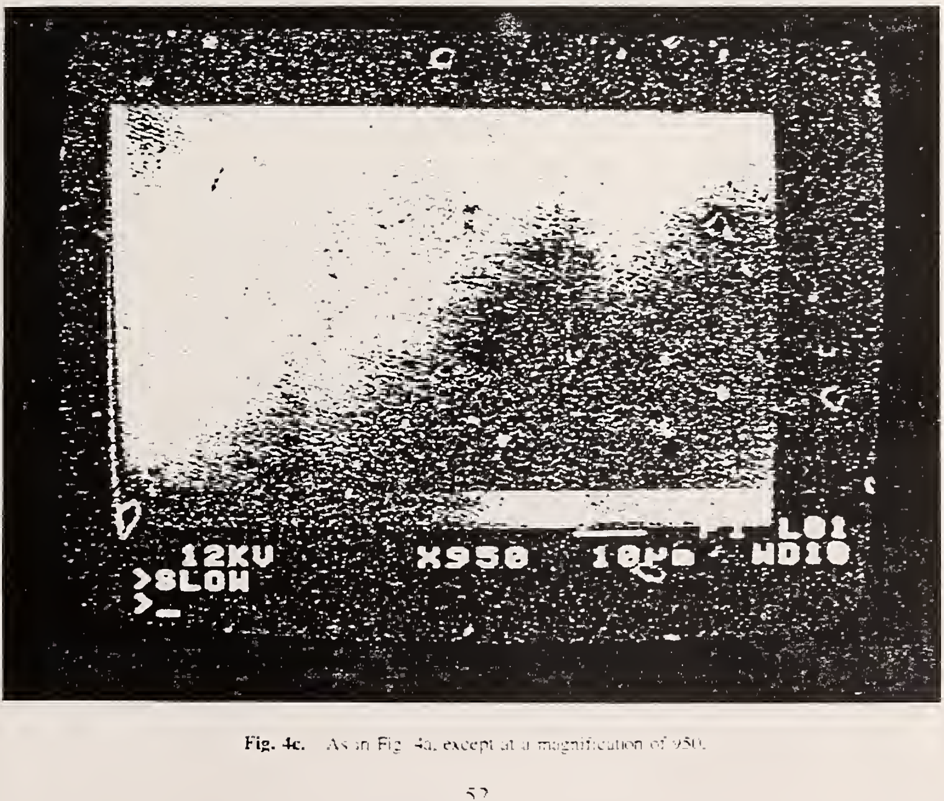

Fig. 4c. As in Fig. 4a, except at a magnification of 950.

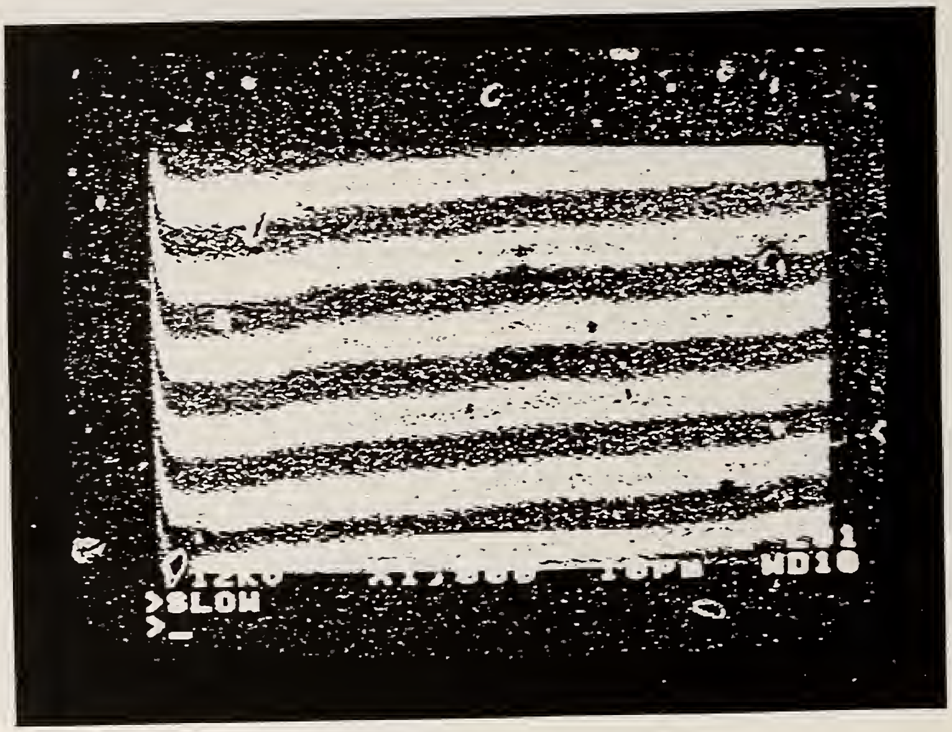

Fig. 4d. As in Fig. 4a, except at a magnification of 1000.

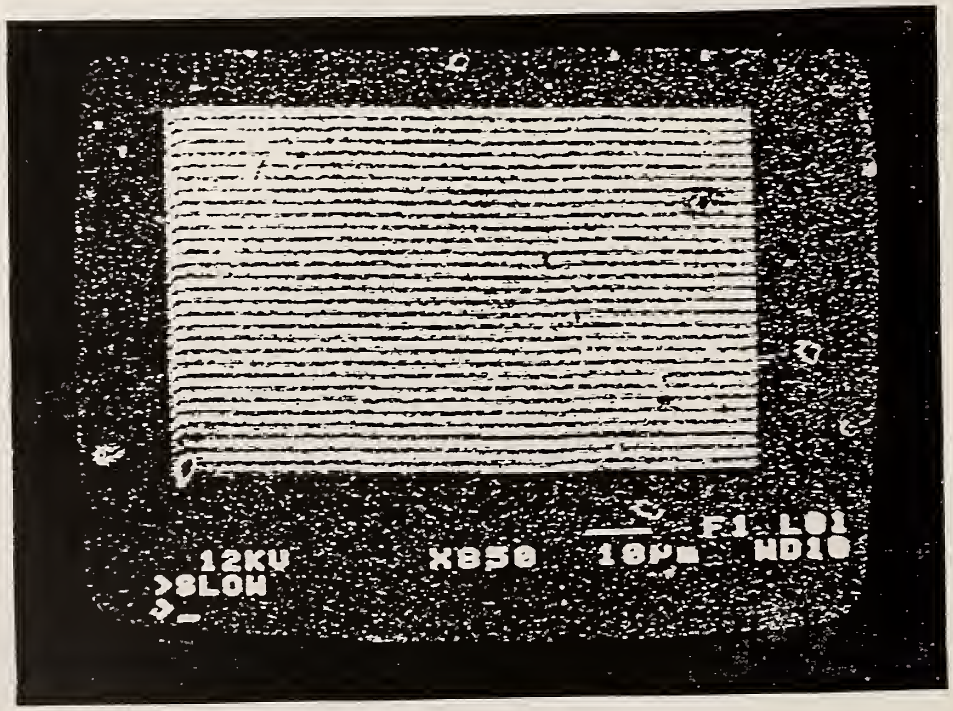

Fig. 4e. As in Fig. 4a, except at a magnification of 1100.

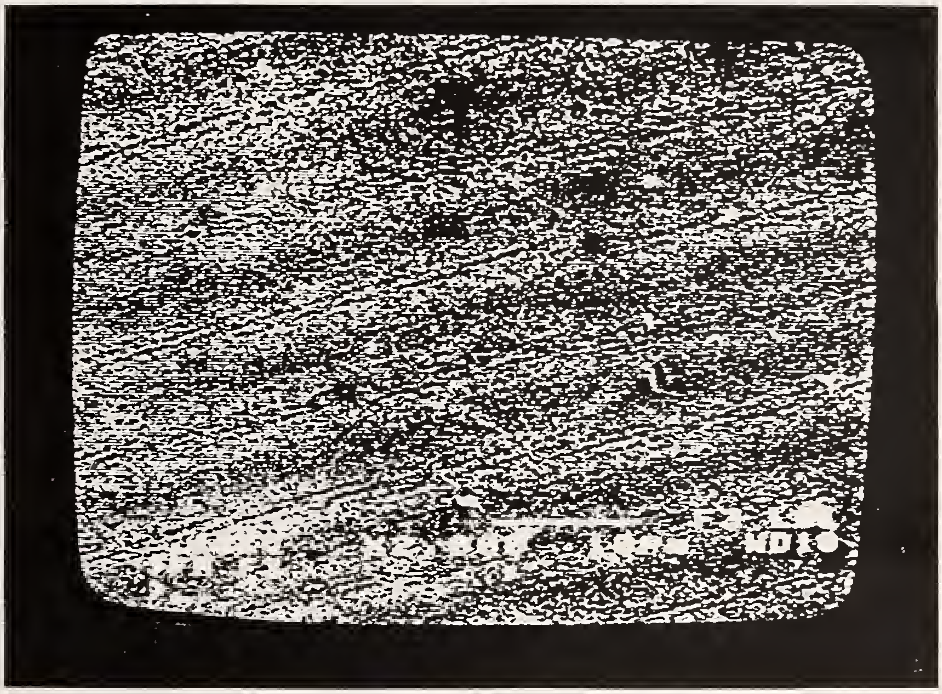

Fig. 5a. Moiré fringes of multiplication with p_t = 200 nm at a magnification of 2000.

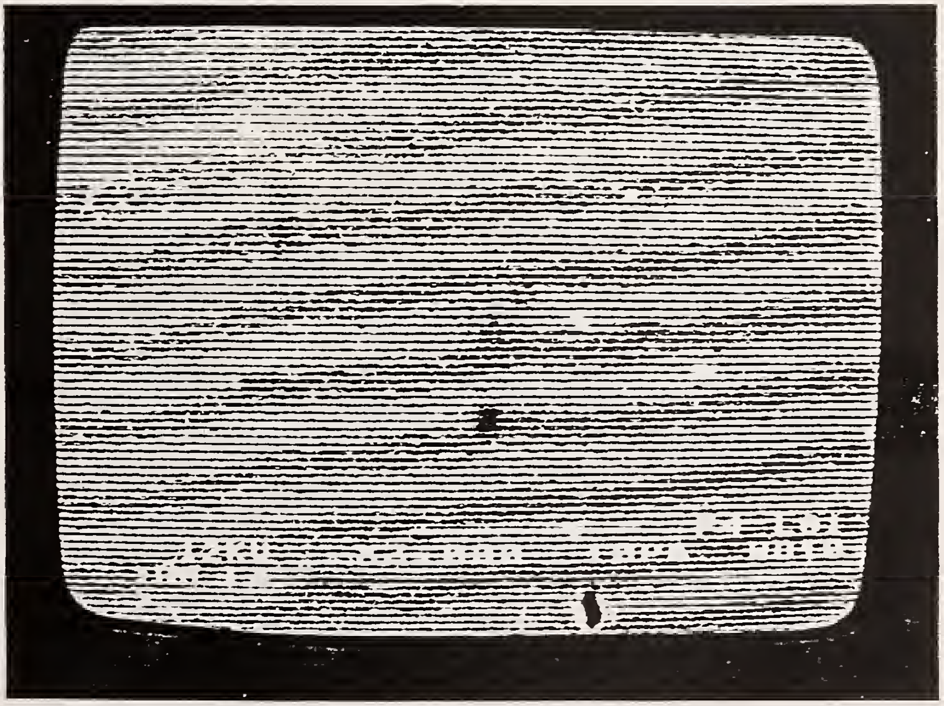

Fig. 5b. As in Fig. 5a, except at a magnification of 3000.

The specimen carries a line grating that consists of an array of lines extending in the $\pm x'$ direction, spaced equally with pitch p_g' in the y'-direction. The reciprocal of p_g' is f_g', the spatial frequency of the specimen grating. The beam and specimen coordinates may be rotated with respect to one another by a control on the SEM. The angle between the x and x' axes is θ.

The number of scan lines used to form the image can be set at various values. Typical nominal settings are 500, 1000, or 2000 scans to produce an image. The images in Figs. 3 to 5 were made with 500 lines. Possible magnification values range from 10 to 300 000. Because of the design of our microscope, only certain discrete values of the magnification are available. As a consequence, it is very unusual for us to achieve a null-field moiré fringe pattern.

The pitch of the electron beam raster scan lines, p_b, depends on the magnification, M, the nominal image size, S, and the number of raster scans used to make the image, R, as

$$p_b = S/MR. \tag{1}$$

For example, with 500 lines per image, a nominal image height of 90 mm, and a magnification of 1900, the scan pitch p_b is 95 nm.

The effective width of the electron beam scan lines depends on the actual e-beam diameter and the interaction of the beam with the specimen surface. Beam diameters of 5 nm to 20 nm are reported in the literature and in the specifications for our SEM. Attainment of very small beam diameters (10 nm) requires very low beam currents, a well-aligned microscope, a small aperture, and extremely sharp focussing. The interaction zone diameter depends on the specimen material and the electron beam energy (accelerating voltage). We believe a value of 15 nm to 30 nm is typical for the effective width of the raster scan lines used in this study.

The specimen gratings are formed by etching thin troughs in a polymeric film about 100 nm thick. The frequencies obtained vary from 2.5 μm^{-1} to 10 μm^{-1}. The lines (troughs) appear as dark stripes in the image and the ridges between the troughs appear as light stripes. In our densest gratings, the width of the troughs and the ridges is approximately equal. A y'-direction trace of the image intensity shows a profile with gradual, rather than abrupt, changes in the image intensity.

3.2 Fourier Representations of the Grating and Scanning Lines

We follow the approach introduced by Sciamarella [8] for optical moiré: we assume that the local intensity (brightness) of the image is proportional to the product of the local scattering power of the specimen grating and the local intensity of the e-beam scan line. The scattering function $G(y')$ for the specimen grating is represented by a Fourier series:

$$G(y') = \frac{g_0}{2} + \sum_{n=1}^{\infty} g_n \cos(2\pi n f_g' y') \tag{2}$$

where the g_n are Fourier coefficients and f_g' is the spatial frequency of the grating lines. After deformation, the specimen grating frequency f_g' can vary with position over the specimen. However, in this treatment we simplify the analysis by considering only deformation fields that produce constant strain over the local region of interest. The frequency f_g' represents the current value at the time of image formation, which is usually different from the original value.

The intensity of the e-beam scan lines $B(y)$ is also represented by a Fourier series:

$$B(y) = \frac{b_0}{2} + \sum_{m=1}^{\infty} b_m \cos(2\pi m f_b y) \tag{3}$$

where the b_m are Fourier coefficients and f_b is the spatial frequency of the raster lines. In both Eqs. (2) and (3), the cosine representation is sufficiently general because somewhere in the image an origin can be found such that the sine terms vanish.

In the simplest case, the y and y' axes coincide. But the raster scan lines can be rotated at an angle θ relative to the grating axes to produce angular misalignment. When $\theta \neq 0$, we will transform $G(y')$ into the coordinates of the raster scan and the image. Since $G(y')$ is a periodic function y' with no dependence on x', the Fourier representation is valid in the transformed coordinates. However, for $\theta \neq 0$ the dependence of the grating scattering function on x' cannot be ignored, and we will consider the specimen grating to be represented by $G(x', y')$. It is convenient to measure the moiré fringe spatial frequency f_i along the y-direction, which is vertical in the SEM images. The spatial frequency of the e-beam raster scan pattern is naturally measured along the y-direction. It is convenient to have all spatial frequencies referred to the same axis, so for calculations we transform the value of the grating frequency into a new value, f_g, the effective grating frequency in the raster scan coordinate system. We take $f_g = f_g' \cos(\theta) = \cos(\theta)/p_g'$, where p_g' is the physical grating pitch, measured in the y' direction. In practice, θ is usually adjusted to be 0 when moiré fringe patterns are being recorded, so in such cases $f_g = f_g' = 1/p_g'$.

The moiré pattern intensity $I(x, y)$ is represented as the product of the raster function and the grating function:

$$I(y) = B(y)\ G(y). \tag{4}$$

Substituting Eqs. (2) and (3) into Eq. (4) and arranging the products of the cosine terms into sum and difference cosine functions gives a relation of the form

$$I(y) = C + F(y) + S(y) + D(y), \tag{5}$$

where $C = g_0 b_0/4$ is a constant. The function

$$F(y) = \left(\frac{b_0}{2}\right) \sum_{n=1}^{\infty} g_n \cos\,(2\pi n f_g y) + \left(\frac{g_0}{2}\right) \sum_{m=1}^{\infty} b_m \cos(2\pi m f_b y)$$

exhibits a frequency that is too high to be observed. The sum function

$$S(y) = \sum_{m=1}^{\infty} \sum_{n=1}^{\infty} \left(\frac{g_n b_m}{2}\right) \cos 2\pi(nf_g + mf_b)y$$

also exhibits a frequency that is too high to be observed. The difference function

$$D(y) = \sum_{m=1}^{\infty} \sum_{n=1}^{\infty} \left(\frac{g_n b_m}{2}\right) \cos 2\pi(nf_g - mf_b)y$$

is the term in the double series expansion that produces the image observed and identified as the moiré fringe pattern.

We simplify Eq. (5) to give

$$I(y) = C_1 + \sum_{m=1}^{\infty} \sum_{n=1}^{\infty} \left(\frac{g_n b_m}{2}\right) \cos 2\pi(nf_g + mf_b)y \tag{6}$$

where $C_1 = C + F(y) + S(y)$ is the intensity of the background.

The result is similar to that obtained in optical moiré. When the magnification yields moiré fringes, neither the grating lines nor the scan lines can be clearly imaged.

The coefficients g_n in the specimen grating function $G(y')$ fall off rapidly with n because of the topography of the grating. The coefficients b_m of the scanning beam raster function $B(y)$ do not decay as rapidly with increasing order m of the expansion. The reason for the persistence in b_m is described later.

3.3 Natural Moiré Fringes

The simplest condition for fringe formation in optical moiré is when f_g is approximately equal to f_b ; this is the near-match condition. Similarly in e-beam moiré we refer to fringes formed under this near-match condition as natural fringes. Because only discrete values of magnification are available on our SEM, we have never been able to achieve a perfect null field, where $f_g = f_b$ and the pitch of the moiré fringes p_m becomes infinite.

Considering the first term in the sum in Eq. (6) ($n = m = 1$) for the near match condition where $f_b \approx f_g$ gives the frequency f_i of the moiré fringe intensity function $I(y)$:

$$f_i = f_g - f_b. \tag{7}$$

In Eq. (7), negative values of the moiré fringe frequency are allowed, because moiré fringes are formed both for $f_g > f_b$ and for $f_g < f_b$. Because the cosine is a symmetric function of its argument, it is impossible to determine from Eq. (6) whether f_b or f_g is greater. This is important in measurements, because it represents the difference between expansion and contraction of the specimen. In practice this ambiguity is resolved by changing the magnification which in turn changes f_b in a known sense. The result is a change in f_i that can be observed and interpreted to determine if f_b is higher or lower than f_g.

Consider small uniform longitudinal strains along the y direction, relative to the ideal null condition where $f_g = f_b$ and $\theta = 0$. Equation 7 implies that the tensile strain ε is given by

$$\varepsilon = -\frac{f_i}{(f_b + f_i)}\,. \tag{8}$$

The periodic form of Eqs. (2) to (6) makes it possible to adopt a vast body of previous developments to interpret e-beam moiré fringes. Some familiar wave phenomena have analogs in SEM images of line gratings. For example, it is clear from Eq. (7) that the moiré fringes are analogous to the beat frequency due to two pure sound tones of slightly different frequencies. Another example is the Doppler phenomena. We observed a changing frequency of the moiré fringe pattern when the specimen was moved under the scanning electron beam.

The contrast of the natural moiré fringes is determined primarily by the amplitude term $g_1 b_1/2$, although higher order terms also affect the contrast. Higher order harmonics of the fringe frequency occur for $m = n = 2$, 3, . . . etc. These harmonics distort the pure sinusoid of the fundamental. Other higher order terms that occur when $n \neq m$ produce signals with a very high frequency that can be disregarded except for their detrimental effect on contrast. Post [9] has used specially selected aspect ratios between bar and space widths in optical moiré to produce "fringe sharpening" effects. Equation (6) shows that the effect of bar and space widths on moiré fringe shape can be calculated by Fourier series techniques. This phenomenon is qualitatively observable in e-beam moiré as a resemblance between the appearances of the grating lines at high magnification and the moiré fringes at low magnification.

3.4 Fringes of Multiplication

Post [11] showed that fringe multiplication occurred in optical moiré when the spatial frequency of the reference grating was a near multiple of the spatial frequency of the specimen grating. The same fringe multiplication occurs in e-beam moiré. We express the spatial frequency of the scan lines, following the notation introduced by Post [11] as:

$$f_b = \beta(1+\lambda) f_g \tag{9}$$

where β is a positive integer and λ is a small fraction. Substituting Eq. (9) into Eq. (7) shows that the spatial frequency of the moiré fringe pattern intensity is:

$$f_i = [n - m\beta(1+\lambda)] f_g = [(n - \beta m) - m\lambda\beta] f_g. \tag{10}$$

Moiré fringes may be observed when $n = \beta m$; then f_i becomes

$$f_i = -m\lambda\beta f_g. \tag{11}$$

The amplitude of the moiré fringe terms in Eq. (6) is given by $g_n b_m/2$. Since β is typically an integer from 2 to 5, $n = \beta m$ is always greater than one, while maximum contrast requires m be fixed at 1. This fact means that fringes of multiplication occur when we match the fundamental frequency of e-beam raster scan with the second, third, etc., harmonics of the grating function. Difficulties in obtaining high contrast fringes of multiplication are due to the decreasing Fourier amplitudes of higher harmonics of the grating function. To illustrate this important result, let $\beta = 2$ and consider a specimen grating that is represented by a symmetric square wave (an amplitude grating with bar width equal to space width). Since g_2, the coefficient of the second harmonic for a square wave, is 0, the contrast goes to zero and these fringes of multiplication cannot be observed.

These results show the importance of the grating scattering function for the contrast of fringes of multiplication. A grating with narrow lines and wide spaces exhibits stronger even harmonics than a balanced grating with equally wide lines and spaces. However, for all shapes, except the periodic delta function, the general rule is that the coefficients g_n decrease rapidly with increasing order of the harmonic. Unfortunately, we have not been able to produce high-density specimen lines that scatter like delta functions by e-beam lithography. Our highest-density gratings scatter much like sinusoids.

Our experience with fringes of multiplication is that they are difficult if not impossible to observe, as is consistent with the preceding development. Examples of fringe multiplication by two and three, Fig. 5, show fringes with lower contrast than those in Figs. 3 and 4.

3.5 Fringes of Division

Moiré fringes of division also occur, but in this case the specimen grating frequency is a multiple of the scan line frequency. Fringes of division are commonly observed at low magnification settings on the SEM, where p_b is larger than p_g. The formation of the fringes of division and their contrast can be explained by using the Fourier representation. Consider an observation in the SEM with a frequency relation given by

$$f_g = \alpha(1+\gamma) f_b \tag{12}$$

where α is an integer and γ is a small fraction. The frequency of the resulting moiré fringe intensity is obtained from Eq. (7) as:

$$f_i = [(\alpha n - m) + \alpha\gamma n] f_b. \tag{13}$$

The moiré pattern can be observed when $\alpha n = m$ and Eq. (13) reduces to:

$$f_i = \alpha\gamma n f_b \tag{14}$$

Since α is an integer typically from 2 to 5, $m = \alpha n$ is always greater than one. This shows that moiré fringes of division are formed by combining the fundamental frequency component of the specimen grating with higher harmonics of the e-beam raster pattern. The e-beam scan lines that are produced at low magnification have relatively high coefficients b_n for n as large as 10.

To show the strength of the higher order harmonics associated with the e-beam scan lines, consider a magnification $M = 500$. With the number of raster lines $R = 500$, this setting on the SEM gives a pitch

$p_b = 360$ nm by Eq. (1). This value of p_b is about 20 times larger than the effective width of the scan line (18 nm). Since the raster scan is only sampling about 5 % of the specimen surface, it behaves like a periodic series of delta functions in y. We show the relative magnitude of the Fourier coefficients for a scan line width $w_b = 0.05\, p_b$ in Fig. 6. It is evident that the coefficients b_m decrease slowly with increasing m. For this reason fringes of division may be observed at many low magnifications with excellent contrast as illustrated by Fig. 3.

As the magnification is increased, p_b decreases and the portion of the field sampled by the scan lines increases. When the ratio w_b/p_b increases, the coefficients of the higher harmonics of $B(y)$ decrease more rapidly with order m. This phenomenon is illustrated in Fig. 6 where the coefficients are shown for $M = 2500$ and $w_b/p_b = 0.25$.

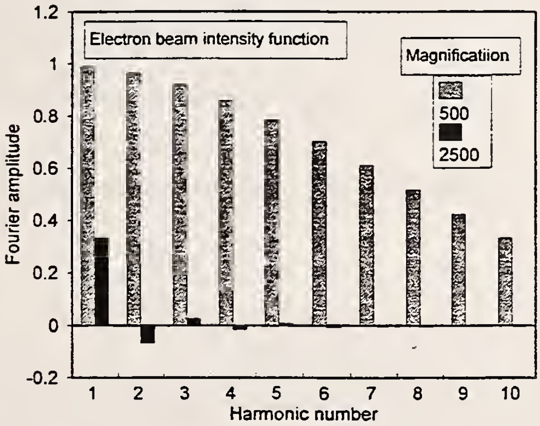

Fig. 6. Estimated relative amplitudes of terms in the Fourier expansion of the electron beam raster scan function $B(y)$, for magnifications of 500 and 2500.

3.6 Fringes of Rotation

Fringes of rotation occur in optical moiré when the pitch of the specimen and reference gratings are closely matched and one grating is rotated relative to the other [1]. Similar fringes of rotation also occur in e-beam moiré. We restate the relevant equation here because the phenomenon is quite commonly observed in e-beam moiré, and is useful. We consider the specimen grating lines to be along the x' axis and the scan lines along the x axis. The angle measured from the x axis to the x' axis is θ, which can be of either sign. When the rotation knob on the SEM is turned clockwise, the specimen's image also appears to rotate clockwise. Of course, the specimen is not actually rotating. The raster scan lines are rotating in the opposite sense. From alignment at $\theta = 0$, counterclockwise rotation of the SEM rotation control produces a clockwise rotation of the raster scan pattern, and thus a positive angle θ. We measure the fringe angle ϕ from the x axis. The moiré fringes of rotation make an angle of ϕ with the x axis, as shown in Fig. 7.

$$\tan\phi = \frac{\sin\theta}{\cos\theta - \frac{p_g}{p_b}} . \qquad (15)$$

At match conditions where $p_g = p_b$, Eq. (15) reduces to:

$$\phi = \frac{\pi}{2} + \frac{\theta}{2} . \qquad (16)$$

Equation (16) indicates that at match for small θ, the moiré fringes are nearly perpendicular to both the grating lines and the raster scan lines. For typical mismatch but small misalignment where $\sin\theta \approx \theta$, Eq. (15) reduces to:

$$\phi \approx \theta \left(\frac{f_g}{f_i}\right) . \qquad (17)$$

Equation (17) shows that small misalignments produce much larger fringe angles, because f_g/f_i is a large quantity whenever moiré fringes are visible. In Eq. (17), ϕ, θ, and f_i can be positive or negative, but f_g is always positive. The value of θ can easily be adjusted in the SEM by a control which rotates the direction of the raster scan pattern. This is helpful because Eq. (17) shows that the sense of the change of ϕ with θ gives the sign of f_i.

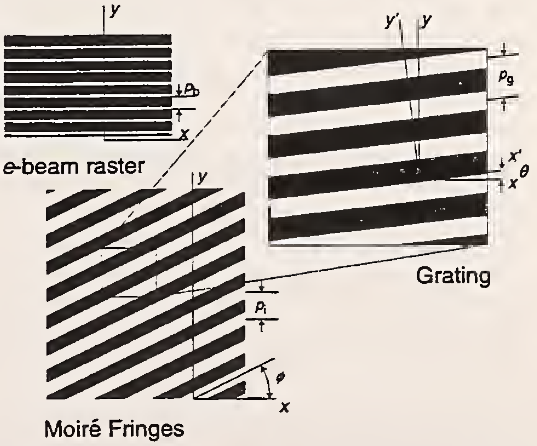

Fig. 7. Definition of geometry and signs of angles when the specimen grating and the electron beam raster scan are not aligned.

4. Magnification, Field Size, and Mismatch

We showed in Eq. (1) that the magnification M and the number R of lines in the SEM raster scan determine the pitch p_b of the scanning lines. As the settings on the SEM are changed, both the size of the field and the e-beam moiré fringe pattern change. A schematic illustration of the field size, the specimen grating, the scan line raster, and the moiré fringe pattern is presented in Fig. 8.

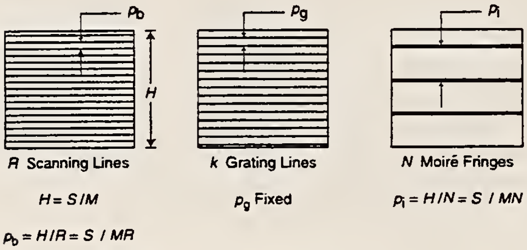

Fig. 8. Illustrations of raster scan lines, grating lines and moiré fringes when the grating area exceeds the field of view.

The field size or observation height H is given by:

$$H = \frac{S}{M}. \tag{18}$$

The pitch of the specimen grating is fixed at p_g for a given experiment. Here we assume that the specimen grating and the raster scan lines are perfectly aligned, so we do not need to differentiate between primed and unprimed coordinates. As long as the height of the grating, h exceeds the field size H, he number of grating lines in the field of observation, k, changes with M as:

$$k = \frac{S}{M p_g}. \tag{19}$$

The number N of moiré fringes across the field of view is:

$$N = R - k \tag{20}$$

and the pitch of the moiré fringes p_i is:

$$p_i = \frac{H}{N} = \frac{S}{MN}. \tag{21}$$

We have defined the fringe order N as positive when the number of specimen grating lines in the field of view exceeds the number of scan lines [(Eq. 7)]. With this definition, we admit both positive and negative fringe orders. By combining these equations, we can show the relation between the moiré fringe frequency and the SEM settings (R and M) as

$$f_i = \frac{1}{p_i} = \frac{1}{p_g} - \frac{RM}{S}. \tag{22}$$

Equation (22) derives from Eq. (7), which was $f_i = f_g - f_b$. At high magnifications, the spatial frequency of the electron beam raster scan is higher than that of the specimen grating, so the frequency of the moiré fringe pattern f_i is negative. The conventional usage [2] is that f_i, p_i, and N are all positive by definition. However, this choice gives rise to the ± in many equations. To avoid this awkward notation, we allow f_i, p_i, and N to be either positive or negative so that the relevant equations are single-valued.

The number of fringes N observed in the field of view is:

$$N = Hf_i = H(f_g - f_b) = H\left(f_g - \frac{MR}{S}\right) \tag{23}$$

when the grating height $h > H$, the field size. Otherwise

$$N = h\left(f_g - \frac{MR}{S}\right) \tag{24}$$

when the grating height $h < H$.

The match condition, which gives the null field, $f_i = 0$, is the same in both cases:

$$M = \frac{S}{R}\frac{1}{p_g} = \frac{S}{R}f_g. \tag{25}$$

For example, a specimen grating with $f_g = 5\ \mu\text{m}^{-1}$ observed in an SEM with $S = 90$ mm and R set at 500 will yield a null field associated with the natural match condition when $M = 900$. Match conditions for fringes of division and multiplication will occur at magnifications of $900/\alpha$ or at $900\ \beta$, for α and β integers.

An experiment was conducted using a specimen grating with $f_g = 5\ \mu\text{m}^{-1}$. The grating area was small ($h = 63\ \mu$m) so that $h < H$ for all choices of M used in the experiment. The SEM was operated with nominal values of $R = 500$ and $S = 90$ mm. The magnification was changed so we observed mismatch conditions with both positive and negative fringes. The results for N as a function of M, presented in Fig. 9, show a linear relation as expected from Eq. (24). The slope of the N vs M relation is [from Eq. (24)]

$$\frac{dN}{dM} = \frac{-hR}{S} . \qquad (26)$$

The slope was determined from the least squares fit of the data as −0.325 . We also noted that the match condition occurred at $M = 977$. From the match condition we could determine that $S/R = 195.4$ μm. For $S = 90$ mm we find that $R = 478$ lines. This result for R agrees with the nominal value supplied by the manufacturer of the SEM.

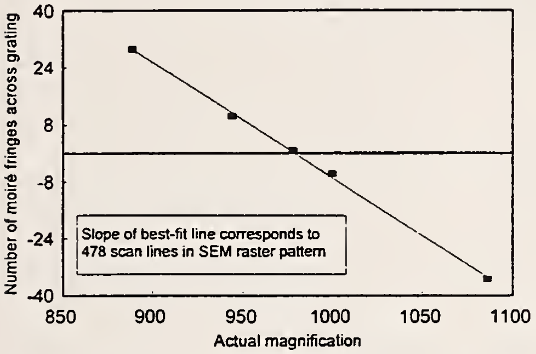

Fig. 9. Fringe count N over specimen grating at different magnifications.

5. Magnification Calibration

The interpretation of moiré fringe patterns depends on precise knowledge of the magnification at any setting M employed to produce a pattern. To check the accuracy of the magnification of the SEM, we measured the length of a distinctive feature on the surface of a specimen at $M = 1000$. We then measured the length of this same feature at other magnifications as indicated on the SEM character display. We found that the actual magnifications were different from the indicated magnifications, as shown in Fig. 10. In preparing Fig. 10 we assumed that the microscope was absolutely correct at $M = 1000$. An improved calibration technique should employ a calibration standard so that the accuracy of all magnification settings could be established.

Examination of Fig. 10 shows that the magnification errors are less than 5 %. Nevertheless the errors are significant in the present analysis as accurate magnification values must be employed in Eq. (23) to properly characterize the scanning line function produced by the SEM. Similarly, the micrometer bar, which also appears in the image display of many microscopes, must also be accurately calibrated if it is to be useful in the quantitative interpretation of e-beam moiré fringes.

The actual magnifications given in Fig. 10 were employed in preparing the data presented in Fig. 9.

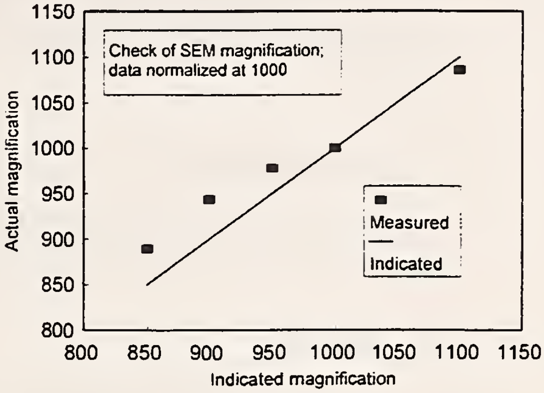

Fig. 10. Actual versus indicated magnification showing relative errors in the SEM magnification calibration. Data normalized to a magnification of 1000.

6. Conclusions

The formation of e-beam moiré fringes in a SEM can be described with a model based on a Fourier series representation of the specimen grating line function $G(y')$ and the raster scan line function $B(y)$. The moiré fringe intensity function $I(y)$ is the product of these two functions. The model describes the variation in the spatial frequency f_i of the moiré fringes with the magnification used in producing the image. It also provides a means for estimating the contrast of different moiré fringe patterns that are observed in the SEM. The spatial frequency f_i of the moiré fringes can be used to measure the spatial frequency f_g of the specimen grating to determine local displacements and strains.

The sensitivity and resolution of measurements made with e-beam moiré are limited by the frequency of the specimen grating. Fringes of multiplication offer enhanced displacement sensitivity per fringe, but require that the specimen grating be fabricated with a trough-ridge ratio that produces substantial higher order Fourier components. Fringes of division are observed as easily as natural moiré fringes because the raster scan lines at low magnifications exhibit significant Fourier coefficients for the higher order terms in the expansion. Fringes of division are useful because they permit a larger field of observation while maintaining the same displacement sensitivity per fringe as is achieved with the natural moiré patterns.

Fringes of rotation are easy to observe by operating the SEM control for the e-beam scan line direction. This control is useful for alignment and for establishing the sign of the moiré fringe frequency f_i.

A method was described for characterizing the SEM based on determining mismatch fringes at different magnifications. The method is dependent on the use of accurate magnification values. We found that calibration of the SEM at each discrete magnification setting was essential.

7. Acknowledgments

J. W. Dally thanks the Office of Naval Research and the National Science Foundation for support during this study.

8. References

[1] Vincent J. Parks, Geometric moiré, in Handbook on Experimental Mechanics, Albert S. Kobayashi, ed., Prentice-Hall, Englewood Cliffs, New Jersey (1987) pp. 282–313.
[2] A. J. Durelli and V. J. Parks, Moiré Analysis of Strain, Prentice-Hall, Englewood Cliffs, New Jersey (1970).
[3] P. S. Theocaris, Moiré Fringes in Strain Analysis, Pergamon Press, Elmsford, New York (1969).
[4] Daniel Post, Moiré interferometry, in [1].
[5] S. M. Graham, Sensitivity and resolution limitations of various moiré methods, Opt. Lasers Eng. **12**, 119–133 (1990).
[6] J. McKelvie, On the limits to the information obtainable from a moiré fringe pattern, in Proceedings of the 1986 SEM Spring Conference on Experimental Mechanics, Society for Experimental Mechanics, Bethel, Connecticut (1986) pp. 971–980.
[7] Y. Morimoto T. and Hayashi, Deformation measurement muring powder compaction by a scanning moiré method, Exper. Mech. **24**, 112–116 (1984).
[8] S. Kishimoto, M. Egashira, and N. Shina, Measurements of grain boundary sliding and observation of microgrids for high temperature use, J. Soc. Mat. Sci. Japan, **40** (452), 637–641 (1991) (in Japanese).
[9] J. W. Dally and D. T. Read, Electron beam moiré, Exper. Mech. 33, 270–277 (1993).
[10] C. A. Sciamaralla, Basic optical law in the interpretation of moiré patterns applied to the analysis of strains—part I, Exper. Mech. 5, 154–160 (1965).
[11] D. Post, Sharpening and multiplication of moiré fringes, Exper. Mech. **28** (4), 329–335 (1988).

About the authors: *David T. Read is a physicist with the Materials Reliability Division of the Materials Science and Engineering Laboratory at NIST. James W. Dally is recently retired from the Mechanical Engineering Department at the University of Maryland. The National Institute of Standards and Technology is an agency of the Technology Administration, U.S. Department of Commerce.*

A7

Electron-Beam Moiré Study of Local Deformation in Conductive Adhesives

by Drexler and Berger (1996)

ELECTRON-BEAM MOIRÉ STUDY OF LOCAL DEFORMATION IN CONDUCTIVE ADHESIVES

E. S. Drexler* and J. R. Berger**
*Materials Reliability Division, National Institute of Standards and Technology, Boulder, Colorado 80303
**Division of Engineering, Colorado School of Mines, Golden, Colorado 80401

ABSTRACT

Electron-beam (e-beam) moiré is a recently developed technique for micromechanics. It allows one to combine the resolution of the scanning electron microscope (SEM) with the strain measurement capabilities of moiré. With e-beam moiré we are able to study locally the effect of temperatures ranging between −50 and 150 °C on conductive adhesives (CAs) and their interfaces. With this technique we measured the local displacements due to the thermal expansion of the copper and the CA. The modified lap-shear specimens were made of copper-to-copper attached with CAs and cured according to the manufacturer's instructions. A cross section of each material was polished and a moiré grating was written on the surface using e-beam lithography techniques. Digital images of the moiré were collected from the SEM at regular temperature intervals. The images were compared and the displacements measured. Local regions of large displacements were observed in the paste specimen. Permanent deformations in the film specimen resulted from exceeding the glass transition temperature of the CA.

INTRODUCTION

E-beam moiré is a recently developed technique first described in [2] and advanced in [1, 3−5]. Utilizing many of the principles of video moiré [6], e-beam moiré is an advancement in resolution, as it is conducted in the scanning electron microscope (SEM). E-beam moiré is based on the fundamentals of optical moiré while exploiting the spatial resolution of the SEM. The limitations of the relatively long wavelength of light are circumvented by imaging with an electron beam. As with moiré interferometry, e-beam moiré does not require a separate, tangible reference grating. The reference grating is an integral part of the SEM--the rastering of the electron beam--and exists whenever the current in the filament is sufficient to produce an image. The electron beam rasters across the field of view at regular intervals, 480 raster scans per image for a typical imaging system. The pitch of the "reference grating" is, therefore, dependent on the magnification and the viewing area of the system. The specimen grating is a series of ridges and trenches generated by e-beam lithography. This lithography takes place in the SEM with the aid of a computer program that controls the location and dwell time of the electron beam.

The magnification for the lithography is nominally the same as for the imaging. The number of lines written is 1 or 2 times the number of rasters of the electron beam so that the initial correlation is approximately 1-to-1 (or 1-to-2). Because the SEM is focussed and tuned using electromagnetic lenses to adjust for differences in focal distance, it is virtually impossible to replicate tuning conditions between sessions on the SEM. A null field, one for which an exact 1-to-1 correlation exists between the specimen and reference gratings, is very rare; therefore, moiré fringes will usually be present for the initial condition.

The resolution of the technique ranges from 90 to 900 nm/fringe order. Resolving values for strain using the technique depends on the pitch of the specimen grating and the ability to discern fractions of fringes. The ideal initial condition would have a few high-contrast fringes, such that resolving to 1/10 of a fringe is possible.

The fringe center is a contour of equal displacement on the surface of the specimen. The effect of the cross-line grating is analogous to having a full-view 0–90° displacement gage with resolution on the order of tens of nanometers. Thus, strains calculated from data obtained with this technique are fully quantitative.

Thermal loading tests were conducted on 2 specimens, a CA paste and a film, in a temperature range from −50 to 150 °C. Moire images were acquired at each temperature and compared with the image from the initial condition.

EXPERIMENT

Tests presented here were conducted on two different isotropic CAs (ICAs), one in paste form and the other a film. The specimens are made up of OFHC copper and CA, as shown in Figure 1. The film specimen was cured at 150 °C for 30 min under continuous pressure, then allowed to cool to room temperature before the pressure was relieved. The paste specimen was assembled and cured without pressure in an oven set to 150 °C for 6 min. The specimen was then removed from the oven and allowed to cool to room temperature.

Each specimen was nominally prepared according to the description given in [5]. The only major deviation is that once the pattern was written a second pattern was superimposed 90° to the first. This provided cross-line gratings needed for the complete determination of in-plane displacements.

The thermal load testing of each CA material was conducted in the SEM using a combined heating and cooling stage over a nominal temperature range of −50 to 150 °C. Cooling was provided by liquid-nitrogen–cooled nitrogen gas flowing through tubing in the stage. A controller maintained the set temperature by balancing the heater output with the chilled air.

Before any images of Pattern A in Figure 1 were acquired, the stage was cycled between 0 °C and 100 °C twice before returning to the ambient temperature noted when the filament was first saturated. This was to ensure that any reseating of the specimen due to heating and cooling of the stage occurred prior to the start of image acquisition. The one-hour period required to do this cycling also gave the electron beam time to stabilize. Images were then stored digitally from both 0° and 90° orientations at ambient temperature. (Throughout the remainder of this paper *u*-field and 0° will refer to the observed images where the grating lines were perpendicular to the interface. *V*-field and 90° images have the grating lines parallel to the interface.) Subsequent 0° and 90° images were acquired at temperature intervals of ~50 °C.

In the film specimen (location B in Figure 1) images were collected from the 0 and 90° orientations one hour after saturating the filament, but before thermally cycling the stage. The stage was then cycled between 0 and 100 °C twice, as before. A second pair of images was acquired at the noted ambient temperature after the thermal cycling. These images were used as the initial condition for the test. Digital images from the 0 and 90° orientations were stored at temperature intervals of 50 °C. The fringe centers from each image from both tests were traced.

The fringe centers were identified on the *u*-field and *v*-field images. Line profiles were chosen running perpendicular and parallel to the orientation of the reference grating on each image. For the *u*-field images three line profiles were chosen such that one was through the CA and the other two were approximately equidistant from the CA, one in the 9.5 mm copper and the other in the 0.4 mm copper.

A graph was made of the distance along the chosen trace versus the assigned fringe order. The fringe order was then converted into length by multiplying by the pitch of the reference grating p_r. With e-beam moiré, since the initial fringe field is rarely null, every subsequent image is analyzed by studying the difference between it and the initial condition image. The slopes obtained from the line profiles from the initial images must be subtracted from the subsequent images to see how each loading step affected the fringe field. Strain data were calculable from these plots of relative displacement versus position along the trace. The slope $\partial u/\partial x$ and $\partial v/\partial y$ of the curves from the line profiles perpendicular to the orientation of the reference grating in the *u*-field and *v*-field images, respectively, are the normal strains. The shear strain is the sum $\partial u/\partial y + \partial v/\partial x$ of the slopes from the curves obtained parallel to the orientation of the reference grating,

RESULTS

CA paste. As one looks at the images collected of the fringe field at each temperature, the amount of local deformation occurring in the CA at 150 °C was notable. In Figure 2a of the *u*-field, the fringes curve through the CA paste and the fringe density was not regular. The corresponding *v*-field image (Figure 2b) shows the fringes following a circuitous path through the CA. (The moiré fringe field images displayed in this study were colorized by computer manipulation to aid in locating the fringe centers. All micrographs acquired from an SEM image are originally black and white.)

The analysis of the series of the *u*-field images showed that the behavior in the thin copper, the CA, and the thick copper were all very similar. Below room temperature the curves exhibited a gradual negative slope, indicative of contraction. Above room temperature there was little sign of expansion at 50 °C, especially in the thin copper. By 100 °C the slope had steepened sharply at all three line traces, in a positive sense, and it steepened still more by 150 °C. The magnitude of the value for the slope when the temperature was increased by 100 °C was far greater than it was when decreasing the temperature 100 °C. The glass transition temperature T_g of the paste is 80 °C. When T_g was exceeded the coefficient of thermal expansion nearly quadruples. The line profile from the CA is shown as an example in Figure 3.

One other significant point to note is the behavior of the curve at the two highest temperatures, particularly in the thin copper and in the CA. In both cases the slope flattened out as it approached the top of the image. The pattern was located at the edge of the lap of the specimen. The flattening of the slope was the effect of the free surface on the thin copper and the CA. That is, there are no normal or shear stresses (or corresponding strains) at a free surface.

The displacement-versus-position curves for the *v*-field showed very unusual behavior at the higher temperatures (see Figure 4 from the center of the pattern). Through 50 °C the curves acted in a regular and supportable manner. As the temperature was reduced the slope became increasingly more negative, with a sharper drop occurring in the CA. As the temperature increased it looked as though the material would behave in the reverse fashion at 50 °C; the curve demonstrated a positive slope becoming more positive through the CA. However at 100 °C the slope became slightly negative, and at 150 °C, significantly negative through the CA. It was clear that locally, around the CA, between 50 and 100 °C the fringe field passed through a null, and the fringe density started to increase in the region, giving the appearance of being in a state of contraction, whereas the region was actually in a condition of greater expansion.

CA film. The first image collected from the paste specimen in the 0° orientation showed that the fringes were bending as they crossed the CA. Because the image was acquired after the specimen and stage were cycled twice between 0 and 100 °C, it was unknown whether the shear deformation was the result of relaxation of residual stresses before exposure to temperature extremes, or whether it was due to thermal cycling. In this test on CA film, images were collected before and after thermally cycling the specimen and stage. Figure 5 shows the ambient temperature images from the 0° orientation before and after cycling. The shear that developed in the CA was the direct result of thermally cycling the specimen and stage between 0 and 100 °C.

The post-cycling ambient-temperature images were used for the initial condition when analyzing the data from this test. The *u*-field data exhibited the anticipated behavior; the slopes become increasingly more negative as temperatures decrease, and increasingly more positive as temperatures increase for all three line profiles (eg. from the CA is shown in Figure 6).

Tracing the fringes from the v-field was very difficult, because the fringe center in the CA was ambiguous. The data would appear to suggest that the CA remains contracted regardless of whether the temperature was increasing or decreasing (see the displacement versus position curves from the center of the specimen shown in Figure 7). The fringe density in the local region of the CA gives some indication that the pattern experienced a null between 0.4 and -9.9 °C. However, the data were not clear enough to unequivocally support this.

CONCLUSIONS

The experiments conducted on the two forms of ICAs yielded useful information on the conduct of these materials under these testing conditions. Both the CAs performed well under the imposed thermal loading conditions. Even though T exceeded T_g and regions of great expansion resulted, the materials did not debond at the copper/CA interface, nor did the silver particles shift or rotate. The CAs kept enough stiffness at the higher temperatures to function as they were designed to in this specimen.

If these materials are to replace solder in fine-pitch applications, it is of concern that they retain the deformation induced at 100 °C. Figure 5 shows that the bending of the fringes in the CA after thermal cycling has a magnitude of approximately half a fringe or 225 nm, in the case of this pattern, which has a specimen pitch $p_s \approx 450$ nm. At the end of the thermal loading test an image was again acquired at approximately room temperature. That image shows the shift through the CA was nearly a full fringe. Indications are that the deformation does not continue to accumulate at the same rate however, as the final image from a second thermal loading test on the same specimen and pattern shows the fringe shift has the same magnitude at the end of the test as it had at the start. Deformations of this magnitude are probably insignificant for a well-placed, properly aligned surface-mount device with a lead pitch of 300 μm. But if pitches continue to become smaller these deformations will eventually lead to failed components.

REFERENCES

1. J. W. Dally and D. T. Read, Exp. Mech. **33**, 270 (1993).

2. S. Kishimoto, M. Egashire, and N. Shina, J. Soc. Mat. Sci. Jpn. **40**, 637 (1991).

3. D. T. Read and J. W. Dally, ASME J. Appl. Mech. **61**, 402 (1994).

4. D. T. Read and J. W. Dally, J. Res. Natl. Inst. Stand. Technol. **101**, 47 (1996).

5. D. T. Read and E. S. Drexler, ASME Proc. Mech. Mat. Electron. Pack. AMD-187 **2**, 185 (1994).

6. Y. Morimoto and T. Hayashi, Exp. Mech. **24**, 112 (1984).

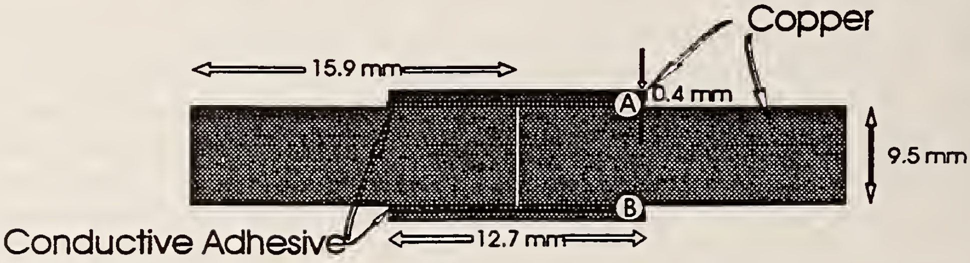

Figure 1. Sketch of the specimen configuration used in the thermal loading tests. The site of the observed pattern for the paste thermal test is A, the film thermal test is B.

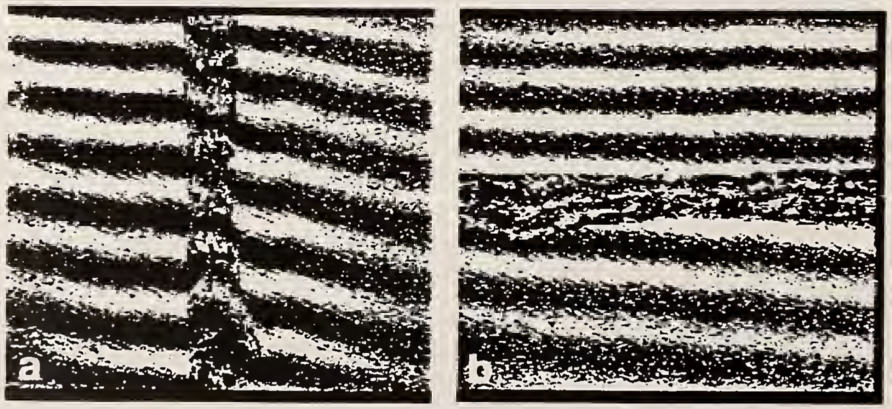

Figure 2. Images at 220× from the CA paste acquired at 150.2 °C of (a) the *u*-field image, and (b) the *v*-field image

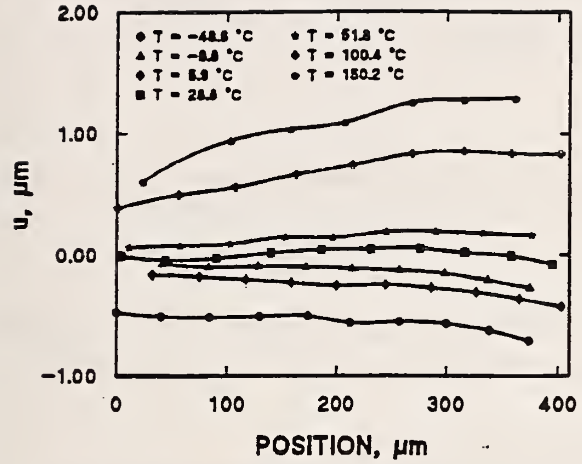

Figure 3. Displacement versus position plots of the *u*-field data on the CA paste.

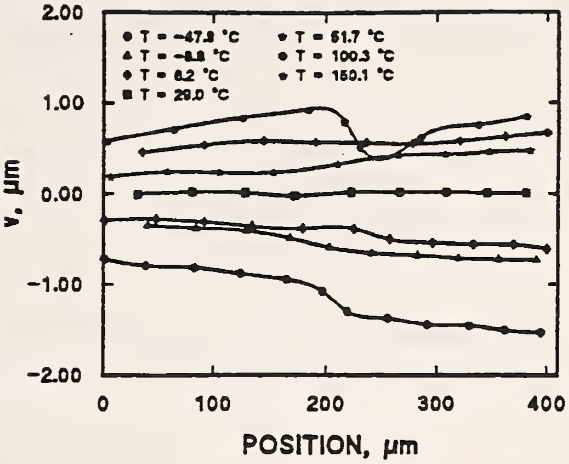

Figure 4. Displacement versus position plots of the *v*-field data on the CA paste.

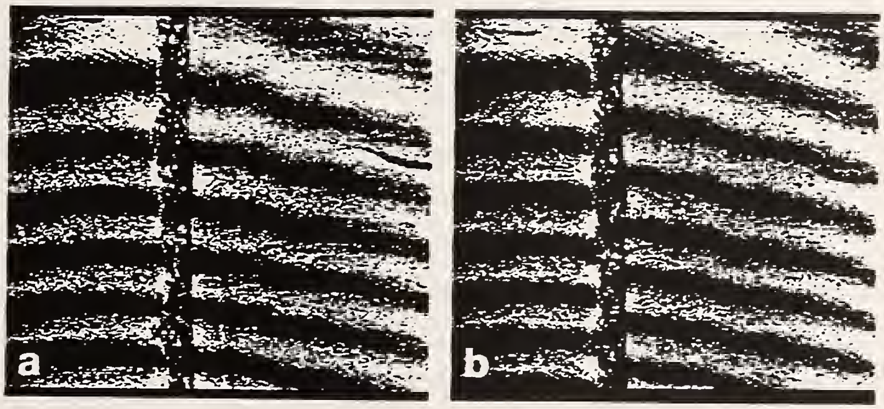

Figure 5. *U*-field images from the CA film acquired at ~28 °C (a) before and (b) after thermally cycling the specimen and stage twice between −50 °C and 150 °C.

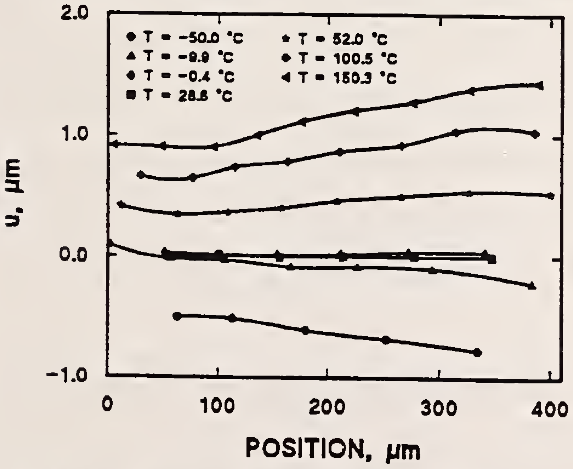

Figure 6. Displacement versus position plots of the *u*-field data on the CA film.

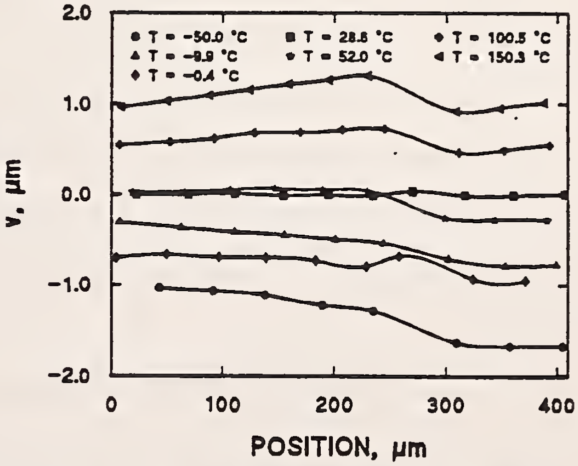

Figure 7. Displacement versus position plots of the *v*-field data on the CA film.

A8

Mechanical Deformation in Conductive Adhesives as Measured with Electron-Beam Moiré

by Drexler and Berger (199?)

Mechanical Deformation in Conductive Adhesives as Measured with Electron-Beam Moiré

E. S. Drexler
Materials Reliability Division
National Institute of Standards and Technology
Boulder, CO 80303

J. R. Berger
Division of Engineering
Colorado School of Mines
Golden, CO 80401

Abstract

Two forms (paste and film) of isotropically conductive adhesives (CAs) were mechanically loaded in shear mode. The specimens were instrumented with crossed-line gratings so that normal and shear displacements could be measured. The CA paste specimen failed outside the observed region at a stress 28% below the manufacturer's predicted value. In the observed region there were no normal strains, only shear strains restricted to the CA. In the film specimen the conducting particles began breaking away from the matrix epoxy at very low loads. However, the specimen continued carrying the additional loading increments until the load was transferred to the adjacent material.

Introduction

The electronics packaging industry routinely uses conductive adhesives (CAs) for packaging applications, most commonly for die attachment, and is considering its use for a number of other applications. When industry is evaluating CAs for different applications, the tests they use typically involve assessment of the electrical properties under various environmental conditions. In addition to measuring the contact resistance, some laboratories also measure certain mechanical properties of the CA joint with respect to the temperature and/or temperature/humidity exposure. Most of these laboratories assess the adhesion strength of an attached component through use of tests designed to provide a comparative value for the shear strength (Gilleo, 1993; Hogerton, et al., 1990; Honoré, et al., 1992; Keusseyan and Dilday, 1993; Kreutter, et al., 1992; Li and Morris, 1995; Liu and Rörgren, 1993; Liu, et al., 1995; Nguyen, et al., 1993;

Contribution of the U.S. National Institute of Standards and Technology, not subject to copyright in the U.S.A.

Rusanen and Lenkkeri, 1995; Stam, et al., 1995).

In this study the mechanical behavior of CAs will be characterized through the use of the electron-beam (e-beam) moiré technique (Dally and Read, 1993; Read and Dally, 1996). This technique is ideal for many electronic packaging situations where features are small and one is interested in knowing the influence of one material on the adjacent material. E-beam moiré is a fully quantifiable technique with which one can measure displacements on the order of tens of nanometers. The visual nature of the technique not only allows one to measure the *u*-field and *v*-field displacements from the area of interest, but upon loading the specimen one can also see developing regions of larger strains—potential failure sites.

Materials Evaluated and Specimen Preparation

Tests presented here were conducted on two different materials (see Drexler, 1996 for details on the sample preparation). Both materials were commercially available isotropically conductive adhesives, one a paste and the other a film. The CAs were stored in a standard freezer for three months, then moved to an ultra-low–temperature freezer set at –45 °C.

The specimen geometry was a double-lap–shear specimen as shown in Fig. 1. The copper pieces were pickled in a 50/50 solution of nitric acid (70.6%) and deionized water to remove the oxide layer. The larger pieces sat in the acid solution for 90 s, and the thinner pieces for 20 s. The pieces were rinsed in deionized water, put in a methanol ultrasonic bath for 30 s, then assembled as shown in Fig. 1.

The film specimen was prepared first. The film was first applied to both 12.7 × 12.7-mm pieces, preheated to 50 °C on a hot plate, then attached to the 15.9 × 12.7-mm pieces. A 140-kPa strain-gage clamp applied pressure during cure. The manufacturer recommends preheating the bonding surface to 45 °C and curing with continuous pressure of at least 35–70 kPa. The specimen was cured for 30 min, as specified by the manufacturer of the film, in a strain-gage oven with the temperature set to 150 °C. At the end of this period the specimen was removed from the oven and allowed to cool to room temperature before the clamp was removed.

A second specimen was fabricated with the paste CA. The CA was stroked with a wooden stick on the surface to be bonded. Teflon tape was wrapped around the 15.9 × 12.7-mm pieces to prevent a butt joint from forming. The specimen was assembled and cured in the oven set to 150 °C. As specified by the manufacturer, no clamping pressure was used. The specimen was allowed to cure for 6 min, because after the 3 min recommended by the manufacturer it did not appear completely set. The specimen was then removed from the oven and allowed to cool to room temperature.

The day after both specimens were cured, each was cut into approximate thirds, so that each piece was 3–4-mm thick. Each piece was ground flat on both sides using SiC paper in several steps from 120 to 1200 grit. One side of each specimen was then polished with 6-μm diamond spray on a napless synthetic silk polishing cloth. One of the three pieces from each type of CA was used to evaluate the CAs thermally (Drexler and Berger, 1997), the second piece was used for the mechanical deformation tests discussed here, and the third piece was held in reserve.

To provide adequate strength to the copper/CA specimens with respect to the anticipated shear strength of the CA, small pieces (12.2 × 3 × 1 mm) of 316LN stainless steel were glued onto the copper sheet using a low-shrinkage epoxy that cured at room temperature. During curing they were held together with binder clips, which exerted an indeterminate pressure. The polishing process as described above was then repeated.

Cross-gratings were prepared on each of the specimens on a different day. Immediately before writing the gratings, each specimen received a final polish with 1-μm diamond spray on synthetic silk polishing cloth. A thin coat of 2% poly methyl methacrylate (PMMA) was spun at 2250 rpm onto the surface of the specimen. The specimen was cured on a hot plate for1 h at 170 °C.

E-beam Lithography

The lithography was performed in a scanning electron microscope (SEM). A computer program controlled the location and dwell time of the electron beam, generating regularly spaced lines. Lines are actually a series of closely spaced, overlapping spots. To obtain cross-line gratings the lines are first written in one orientation, then the specimen is rotated 90°, and the lithographic process is repeated. This rotation takes place electronically rather than physically; the x-input is sent to the y-output, and vice versa, thereby changing the orientation of the beam. The effect is to rotate the specimen clockwise 90°.

To write the patterns, the microscope was set to 20 kV of accelerating voltage. An aperture of 50 µm and a probe current of 50 pA were chosen to focus the beam as tightly as possible. The astigmatism, centering of the aperture, working distance, and focus were also carefully adjusted and tuned in order to obtain as small a spot size as possible. A small spot size for the electron beam is necessary to obtain line pitches of 90–225 nm.

When all the patterns on a given specimen were completed, the specimen was removed from the SEM for development. During exposure the electron beam breaks up the polymer chains of the PMMA, but development of the specimen is required to wash those broken polymer chains away. The developer used was a 3:1 solution of isopropanol and methyl isobutyl ketone (MIBK). Following development, a thin (<10-nm) coating of gold-palladium (AuPd) was deposited over the polymer using a sputter coater to provide a conductive surface. The specimen remains cool throughout the sputtering process.

Mechanical Tests

The mechanical tests were conducted on a tension/compression stage situated within the vacuum chamber of the SEM. The stage has a motor-driven screw-type actuator with a load capacity of 4450 N. It is capable of only uniaxial compression and tension with the present hardware. A universal joint used to drive the stage, and the wires that monitor the load and displacement have access into the SEM chamber through a plate that replaces the side port.

The gage length of the specimen is limited to 15 mm. The specimen is installed on the stage with wedge grips, each end of which is tightened with two bolts. The motor speed is regulated with a pot-type knob that sets the rate between 0 and 100% of 330 rpm. The stage showed no discernable movement below 10%, however. Most of the loadings were conducted at 15%, taking less than 1 min to load 90 N. The load is indicated by a digital display on the controller for the stage.

Both mechanical tests were performed on the same day. The patterns had crossed-line gratings with a pitch of 350 nm, so displacement data were available from both the 0 and 90° orientations. The rotation of the scanning electron beam to interrogate both directions of displacement was performed using a controller designed specifically for precise 90° rotations. The gratings were located on the specimens near the inside free surface of the larger copper block. Their locations in Fig. 1 are indicated by *A* for the paste specimen and *B* for the film specimen. The specimen was loaded in tension with the loading axis parallel to the long dimension of the specimen.

The specimen containing the CA paste was tested first. The moiré effect was observed at an accelerating voltage of 7 kV, a working distance of 18 mm, a probe current of 15 pA, and a magnification of 550×. The filament was saturated 130 min before the first images were acquired. Images from both orientations were accumulated at nominal loads of 0 to 600 N in 80-N increments. At the end of each load increment, images were acquired after the SEM image had stabilized. A final set of images was also acquired at 0 N after the specimen was unloaded. The images were exported onto a computer where the fringe centers were digitally traced for later analysis.

The specimen containing the CA film was tested second. The working distance for this test was 17 mm. The accelerating voltage was 7 kV, the magnification was 550×, and, at the start of the test, the probe current was 15 pA. The probe current was reset to 18 pA later in the test because fringe contrast was poor in the CA. Due to time constraints, the filament was saturated for only 25 min before the first images were acquired. Images were accumulated from both orientations at nominal loads of 0 to 540 N in 80-N increments. The images were again exported to a computer where the fringe centers from each image were digitally traced.

Analysis of the Moiré Fields

The fringe-tracing program mentioned previously allows one to assign a locus of points that define the center of the fringe. This fringe center is also a contour of constant displacement on the surface of the specimen. The effect of the crossed-line grating is analogous to having a full-view 0 and 90° displacement gage. For the tests described here, the pitch of the specimen grating was 350 nm, resolvable to 1/10 of a fringe, translating to 35 nm of displacement. Thus, strains calculated from data obtained with this technique are fully quantitative.

Once the fringe centers were identified, analysis was completed in the manner described by Parks (1987). The fringe centers were identified on the *u*-field (0°) and *v*-field (90°) images. Line profiles were chosen running perpendicular and parallel to the orientation of the reference grating on each image. Three line profiles were chosen perpendicular to the orientation of the reference grating in each of the *u*-field and *v*-field images, and one trace was chosen at the midpoint of the images from the *u*-field and *v*-field images perpendicular to the orientation of the reference grating. For the *u*-field images the three line profiles were chosen so that one was through the CA and the other two were approximately equidistant from the CA, one in the 9.5-mm copper and the other in the 0.4-mm copper.

The distance along the chosen trace was graphed versus the measured fringe order. The fringe order was then converted into displacement by multiplying by the pitch of the reference grating. Since with e-beam moiré the initial fringe field is rarely null, an image was collected before applying the first load increment. The slopes obtained from the line profiles of the initial images were then subtracted from the data obtained from subsequent images obtained under load. Strain data were then calculated from these plots of relative displacement versus position along the trace. The slopes of the curves, $\partial u/\partial x$ and $\partial v/\partial y$, from the line profiles perpendicular to the orientation of the reference grating in the *u*-field and *v*-field images, respectively, are the normal strains. The engineering shear strain, γ_{xy}, is the sum of the slopes from the curves obtained parallel to the orientation of the reference grating, $\partial u/\partial y + \partial v/\partial x$.

Results: Conductive Adhesive Paste

The shear strength of the CA paste was evaluated using the modified lap-shear specimen shown in Fig. 1. The specimen was loaded until catastrophic failure occurred. The failure took place outside the field of view of the pattern studied. Failure was anticipated by rapid movement of the grating lines that were being observed, followed by the load dropping to 0 N. The fringe fields exhibited very little activity either locally or regionally while the loading was applied. The fringe density did not change significantly; however, the tilt of the fringes through the CA did change as the test progressed, indicating a change in the shear strain in the CA.

An error was made during testing when the microscope was refocused after the first loading was applied. Although the fringe field did not appear significantly different, it became apparent during analysis that the images acquired at 0 N were not appropriate to use as the initial condition for the remaining test. Berger, et al. (1997) found in previous studies that the initial fringe field was dependent on all SEM-controlled parameters such as focus, working distance, and accelerating voltage. Since it was not known whether plastic deformation occurred in the area of the pattern studied, the final 0 N image also could not be reliably used for the initial condition. We therefore used the images from the first load increment (82 N) for the initial condition.

Fig. 2 shows the curves for displacement versus position for the line trace located in the CA in the *u*-field images. These curves are representative of the curves obtained from each of the traces in the copper. All the curves remain essentially horizontal, indicating that there was no normal strain, except for the curve acquired at 260 N. That curve displays what seems to be significant compression for all three line profiles as the top of the pattern is neared. This behavior must be considered anomalous for the following reasons. Firstly, because of the specimen geometry there is no location where both the 9.5-mm copper and the 0.4-mm copper will simultaneously be in compression under tensile loading given a line drawn perpendicular to the loading direction. Secondly, the pattern itself is located near the mid-point of the specimen. This is the region where the 0.4-mm copper is subject to the greatest amount of tension. Finally, images acquired at loads above and below 260 N do not display similar behavior, and the loading was smooth and continuous, showing no jumps or drops indicative of slip occurring outside the field of view. This anomalous behavior was probably the result of the specimen or stage not being completely stabilized after the loading step was completed and the image was collected.

Since the curves for the other load increments are horizontal, no normal strain is detectable for any load. It should be noted that no normal strains were discernable in the region occupied by the grating including at the load increment prior to catastrophic failure.

Fig. 3, showing the *v*-field, displacement-versus-position curves, displays similar habitude to that of the *u*-field images. Again, the center line trace is representative of those obtained from the top and bottom of the pattern. All the curves are essentially horizontal except for the post-failure 0-N curve. The implication of the horizontal curves is that the material did not strain normally at any load increment all the way to nearly 600 N from its initial load of 82 N.

The post-failure 0-N curve exhibits a slightly negative slope. There are two possible sources for this: this slope difference could be the difference one would have observed if an initial image with 0-N load had been used, or the failure could have caused the specimen to move slightly out-of-plane, changing the focal plane from the surface of the specimen causing the fringe field to alter.

The reason why no normal strains are observed in the *u*- and *v*-fields becomes evident when the *u*-field displacement versus *y* position is studied. This information is displayed in Fig. 4. This figure shows that all the deformation was carried in the CA—each additional loading increment results in the increased magnitude of the slope of the corresponding curve. In this set of collected images $\partial v/\partial x$ was insignificant, so $\gamma_{xy} \cong \partial u/\partial y$. Fig. 5 shows the shear stress versus shear strain for this data. The elastic region is difficult to establish without a data point at 0 N and with so few data points. However, the general shape of the stress-strain curve is discernable.

Results: Conductive Adhesive Film

The mechanical loading of the film specimen showed many of the same effects as those observed in the paste mechanical test; insignificant normal strains were observed in the *u*-field or *v*-field images. However very little load was applied to the specimen (246 N) before the fringes were no longer traceable in the CA (Fig. 6a). Already at this load the fringes in the 0.4-mm and the 9.5-mm copper were no longer parallel (see Fig. 6b). This indicates that significant deformation has occurred in the CA. The specimen continued to carry the load without catastrophic failure and the images were collected in approximately 85-N increments to nearly 600 N. At this point the specimen would no longer carry the load, but was yielding in the 0.4-mm copper (see Fig. 7). Data were not available from within the CA from loads of 246 N and greater, but the $\partial u/\partial y$ data from the first three load increments (Fig. 8a) suggest that this component the shear strain increased with each load increment. The $\partial v/\partial x$ data (Fig. 8b) from the 0.4-mm copper in comparison, show that the shear strains are barely changing with each load increment until the 537-N load is achieved. The slope increases dramatically at that load, with evidence pointing to greater shear strains as the center of the specimen is approached.

Discussion and Conclusions

The experiments performed on the two forms of isotropically conductive adhesives yielded useful information on the conduct of these materials under these testing conditions. The mechanical tests revealed some fundamental behavioral differences between the conductive adhesive paste and the film. The CA paste specimen carried the load to failure with virtually no deformation to the copper and with measurable amounts of shear within the CA. Inspection of the CA in the fractured region showed deformation within the silver particles, but good continuity at the epoxy/silver interface. The specimen failed at 8.4 (±0.1) MPa though the manufacturer predicted a failure shear stress of 11.7 MPa. The only difference between the manufacturer's specification and the test described here was that the manufacturer's shear strength was based on an aluminum-to-aluminum specimen.

A 28% drop in expected shear strength leaves one speculating on possible explanations. The materials were stored for three months in a standard freezer before being transferred to an ultra-low–temperature freezer. The manufacturer specifies a storage life of six months at 10 °C, and one year at –40 °C for the CA paste. The material should not have degraded during the nine months that it was in storage. The mechanical paste specimen was prepared and instrumented with gratings four times, essentially thermally cycling it four times before any testing was conducted. A thermal fatigue test may indicate whether thermal cycling affects the shear strength to this degree.

The mechanical test on the film specimen showed evidence of failure at such low loads that one must wonder whether the film degraded during storage. The manufacturer suggests storing the film at 5 °C with shelf life of six months. (The manufacturer in 1995 updated the acceptable storage conditions to include one year at –40 °C. It is not clear if the chemistry changed during that time.) As with the paste the film was stored for a total of nine months before the specimen was made, three months in a standard freezer and an additional six months in an ultra-low–temperature freezer.

The film specimen showed curiously contrasting behavior during the test. Although damage occurred in the CA at low load levels, catastrophic failure of the CA never occurred in this test. The CA continued yielding until the strain, carried entirely by the CA, was sufficient to induce yielding in the copper, and once the copper started yielding and the CA no longer carried the load, the test was over. The manufacturer predicted a shear strength of 17.2 MPa for an aluminum-to-aluminum specimen. And although loads never approached this level, the CA never in fact actually failed mechanically.

Though the CA film never actually failed, damage had occurred. Evaluating the CA for use as a replacement for solder requires not only that it have mechanical strength, but that it also maintains a conducting path during that loading. Although this specimen was not designed to evaluate both situations, Fig. 9 shows that the conducting path, at least locally, has been compromised. The silver particle in the center of the image has broken away from the epoxy so that it is now isolated from the copper. As a result, at this location, a conducting path no longer exists between the copper and the conducting silver particles.

Acknowledgments

JRB acknowledges the support of the National Science Foundation and the National Institute of Standards and Technology under the joint NSF-NIST program CMS-9522147.

References

Berger, J. R., Drexler, E. S., and Read, D. T., 1997, "Error Analysis and Thermal Expansion Measurement Using Electron-Beam Moiré," submitted to *Experimental Mechanics.*

Dally, J. W., and Read, D. T., 1993, "Electron-Beam Moiré," *Experimental Mechanics*, Vol. 33, pp. 270–277.

Drexler, E. S., 1996, "Thermal and Mechanical Deformation Measurements of Conductive Adhesives Using Electron-Beam Moiré," M.S. Thesis, Department of Materials Science, Colorado School of Mines, CO, 116 p.

Drexler, E. S., and Berger, J. R., 1997, "Electron-Beam Moiré Study of Local Deformation in Conductive Adhesives," *Symposium Proceedings of the Fall 1996 Meeting of the Materials Research Society: Electronic Packaging Materials Science IX*, Vol. 445, S. K. Groothuis, P. S. Ho, K. Ishida, and T. Wu, eds, Materials Research Society, Pittsburgh, PA, pp. 75–80.

Gilleo, K., 1993, "Intrinsically clean polymer bonding: What are the trade-offs? " *Proceedings of the Surface Mount International Conference and Exposition*, pp. 655–661.

Hogerton, P. B., Carlson, K. E., Hall, J. B., Krause, L. J., and Tingerthal, J. M., 1990, "An evaluation of a heat-bondable, anisotropically-conductive adhesive as an interconnection medium for flexible printed circuitry," *Proceedings of the IEPS Technical Conference*, pp. 1026–1033, 1990.

Honoré, J. P., Rubin, H. D., and Zierold, M. K., 1992, "Reliability testing of conductive adhesives," *Proceedings of the NEPCON West Technical Program*, Vol. 3, pp. 1372–1380.

Keusseyan, R. L., and Dilday, J. L., 1993, "Electric contact phenomena in conductive adhesive connections," *Proceedings of the Surface Mount International Conference and Exposition*, pp. 567–571.

Kreutter, N. P., Grove, B. K., Hogerton, P. B., and Jensen, C. R., 1992, "Effective polymer adhesives for interconnect," *Proceedings of the 7th Electronic Materials and Processing Congress*, pp. 249–256.

Li, L., and Morris, J. E., 1995, "Structure and selection models for anisotropic conductive adhesive films," *Journal of Electronic Manufacturing*, Vol. 5, pp. 9–17.

Liu, J., and Rörgren, R., 1993, "Joining of displays using thermosetting anisotropically conductive adhesives," *Journal of Electronics Manufacturing*, Vol. 3, pp. 205–214.

Liu, J., Ljungkrona, L., and Lai, Z., 1995, "Development of conductive adhesive joining for surface-mount electronics manufacturing," *IEEE Transactions on Components, Packaging, and Manufacturing Technology—Part B*, Vol. 18, pp. 313–319.

Nguyen, G. P., Williams, J. R., and Gibson, F. W., 1993, "Conductive adhesives," *Circuits Assembly*, Vol. 4, pp. 36–38, and 41.

Parks, V. J., 1987, "Geometric moiré," in *Handbook on Experimental Mechanics*, A. S. Kobayashi, ed., Prentice Hall, Englewood Cliffs, NJ, pp. 282–313.

Read, D. T., and Dally, J. W., 1996, "Theory of electron-beam moiré," *Journal of Research of the National Institute of Standards and Technology*, Vol. 101, pp. 47–61.

Rusanen, O., and Lenkkeri, J., 1995, "Reliability issues of replacing solder with conductive adhesives in power modules," *IEEE Transactions on Components, Packaging, and Manufacturing Technology–Part B*, Vol. 18, pp. 320–325.

Stam, F., O'Grady, P., and Barrett, J., 1995, "Characterisation and reliability study of anisotropic conductive adhesives for fine pitch package assembly," *Journal of Electronics Manufacturing*, Vol. 5, pp. 1–8.

List of Figs.

Fig. 1. Specimen geometry for the specimens tested in this study. A indicates the pattern location for the paste test, and B the location for the film test.

Fig. 2. Normal displacement versus position (x) for the u-field taken from the center of the pattern (the CA) from the specimen fabricated with the CA paste.

Fig. 3. Normal displacement versus position (y) for the v-field taken from the center of the pattern from the specimen fabricated with the CA paste.

Fig. 4. Shear displacement versus position $\partial u/\partial y$ for the specimen fabricated with the CA paste.

Fig. 5. Shear stress versus shear strain for the specimen fabricated with the CA paste.

Fig. 6. Images at 550× of the (a) u-field and (b) v-field moiré fringe fields at a load of 246 N on the specimen fabricated with the CA film.

Fig. 7. V-field image at 550× of the moiré fringe field at a load of 537 N on the specimen fabricated with the CA film.

Fig. 8. Shear (a) $\partial u/\partial y$ data from the CA for the first three load increments, and (b) $\partial v/\partial x$ data from the 0.4-mm-thick copper from the specimen fabricated with CA the film.

Fig. 9. Image at 6500× of the CA film specimen at a load of 328 N. (The ubiquitous array of dots is the crossed-line grating.)

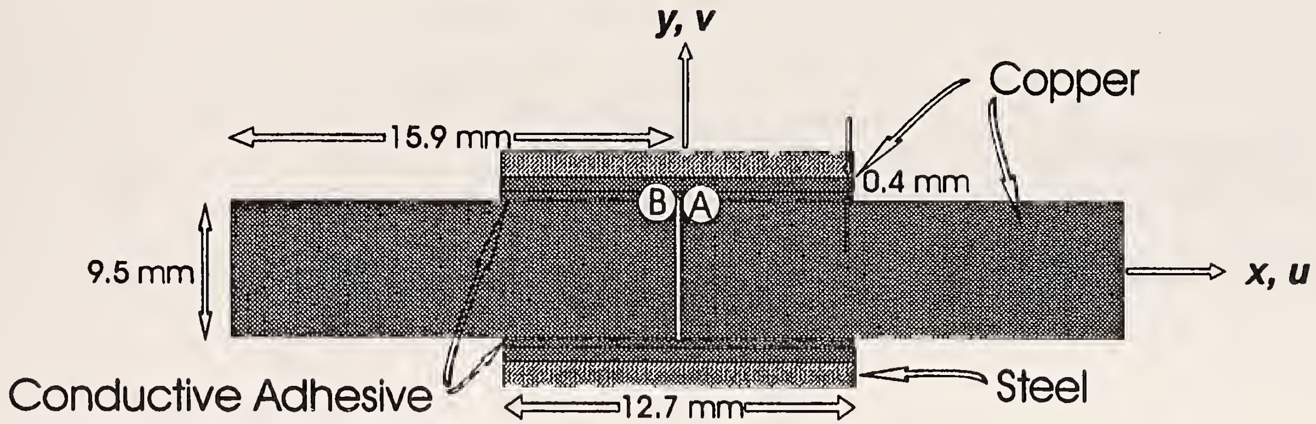
y, v
Copper
15.9 mm
0.4 mm
B
A
9.5 mm
x, u
Conductive Adhesive
12.7 mm
Steel

Figure 1

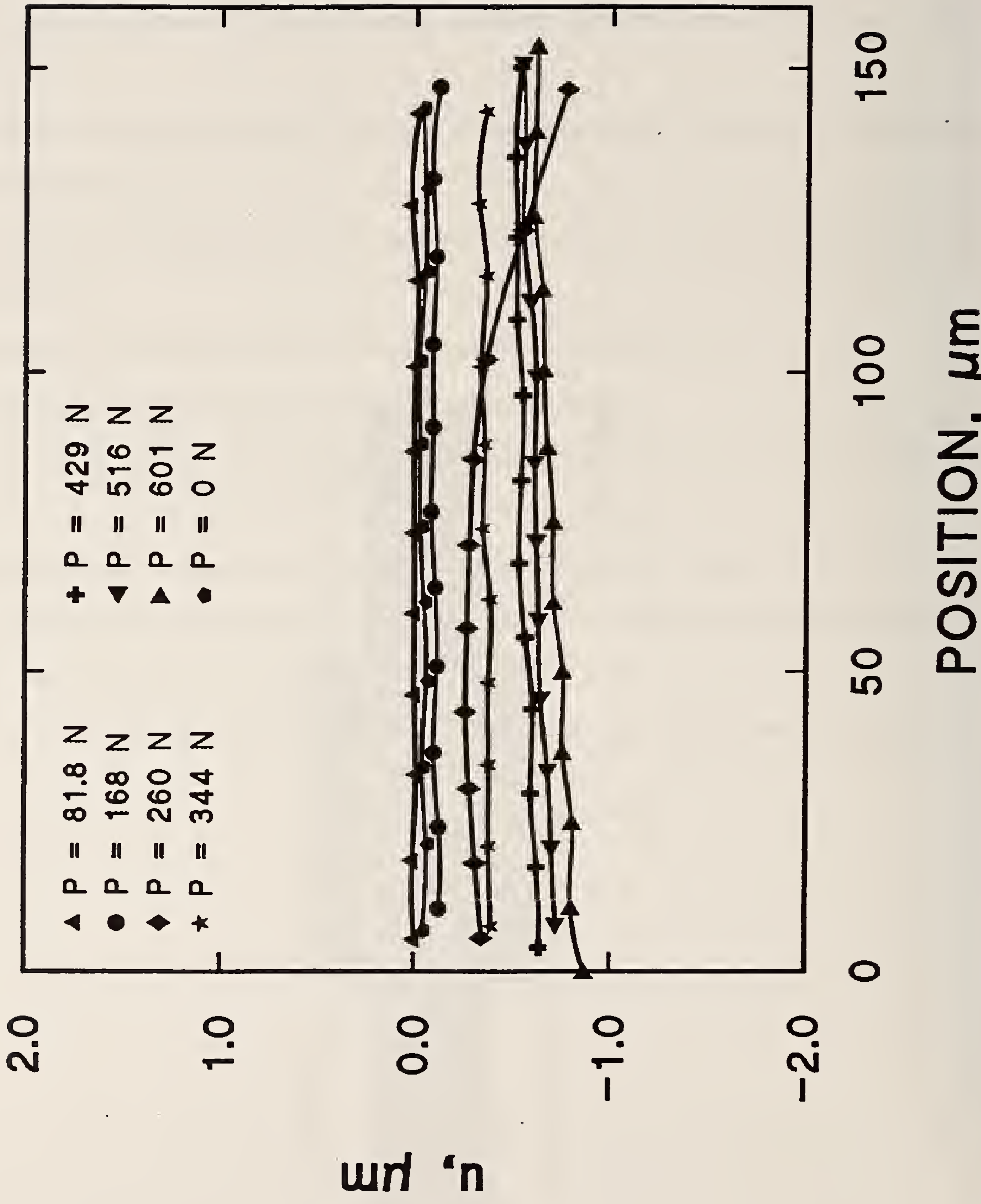
▲ P = 81.8 N
● P = 168 N
◆ P = 260 N
★ P = 344 N
✚ P = 429 N
▼ P = 516 N
▲ P = 601 N
● P = 0 N
2.0
1.0
0.0
−1.0
−2.0
0
50
100
150
u, µm
POSITION, µm

Figure 2

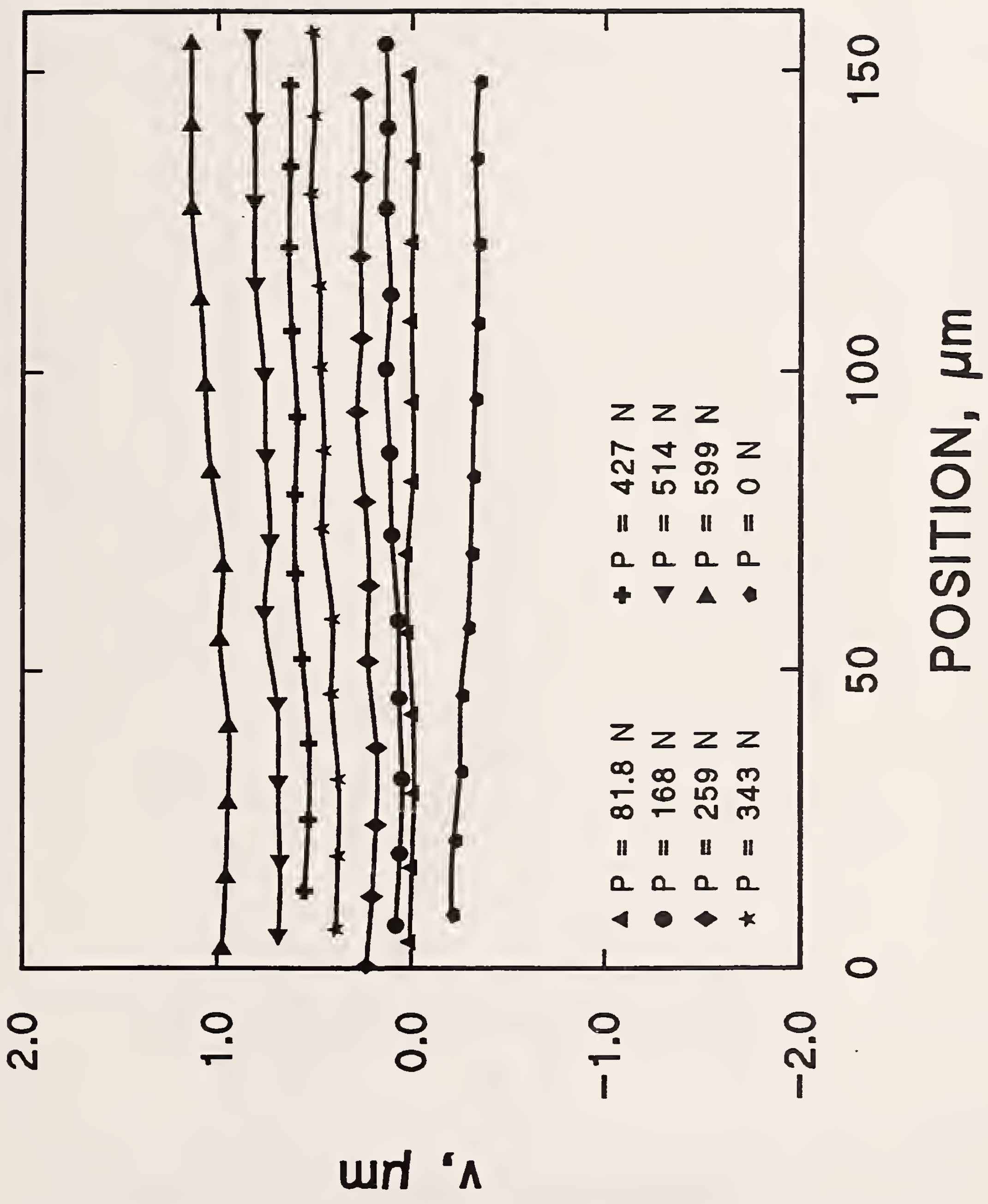
v, μm
2.0
1.0
0.0
−1.0
−2.0
0
50
100
150
POSITION, μm
▲ P = 81.8 N
● P = 168 N
◆ P = 259 N
★ P = 343 N
✚ P = 427 N
▼ P = 514 N
▲ P = 599 N
● P = 0 N

Figure 3

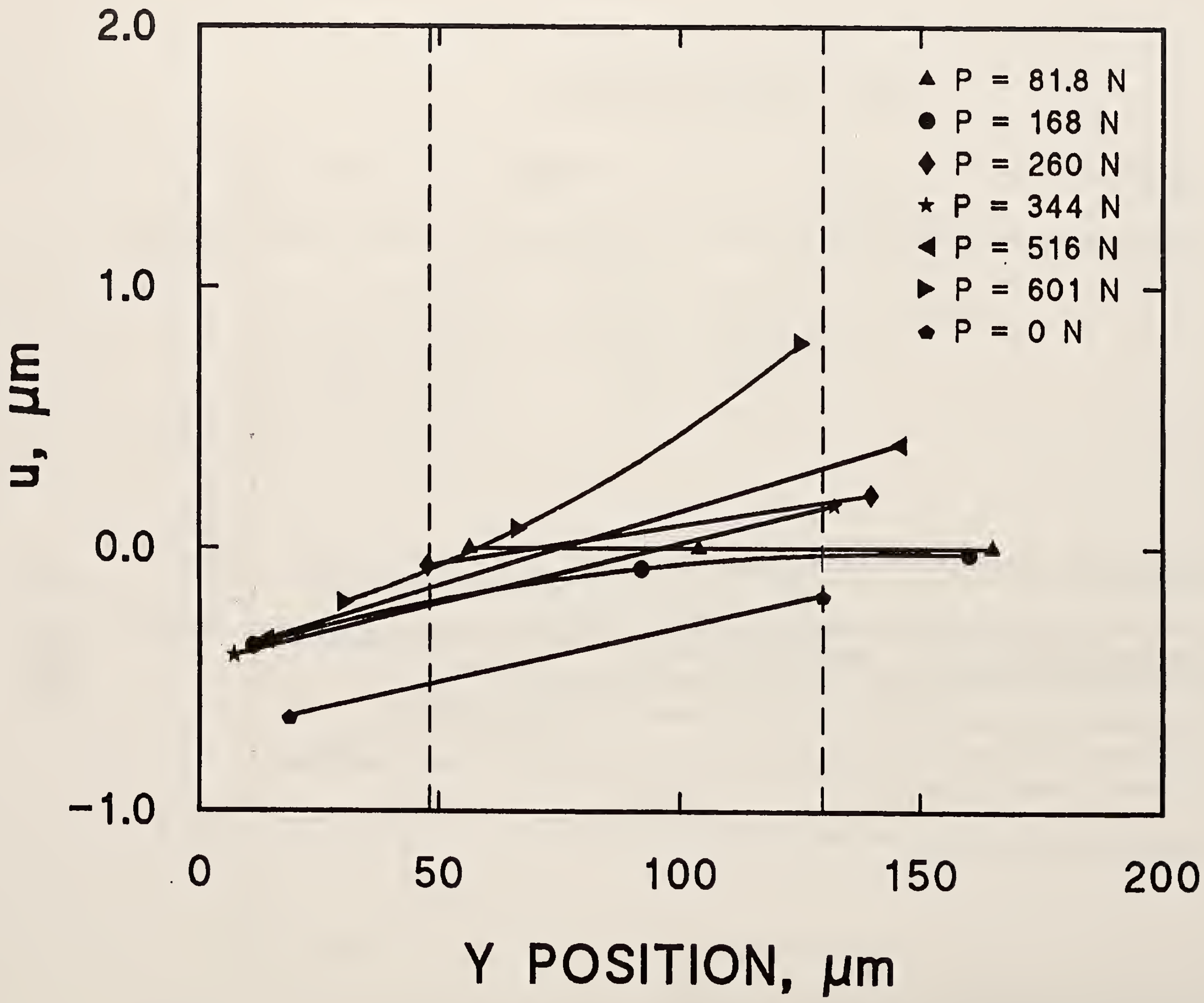
2.0
1.0
0.0
−1.0
u, μm
0
50
100
150
200
Y POSITION, μm
▲ P = 81.8 N
● P = 168 N
◆ P = 260 N
★ P = 344 N
◀ P = 516 N
▶ P = 601 N
⬟ P = 0 N

Figure 4

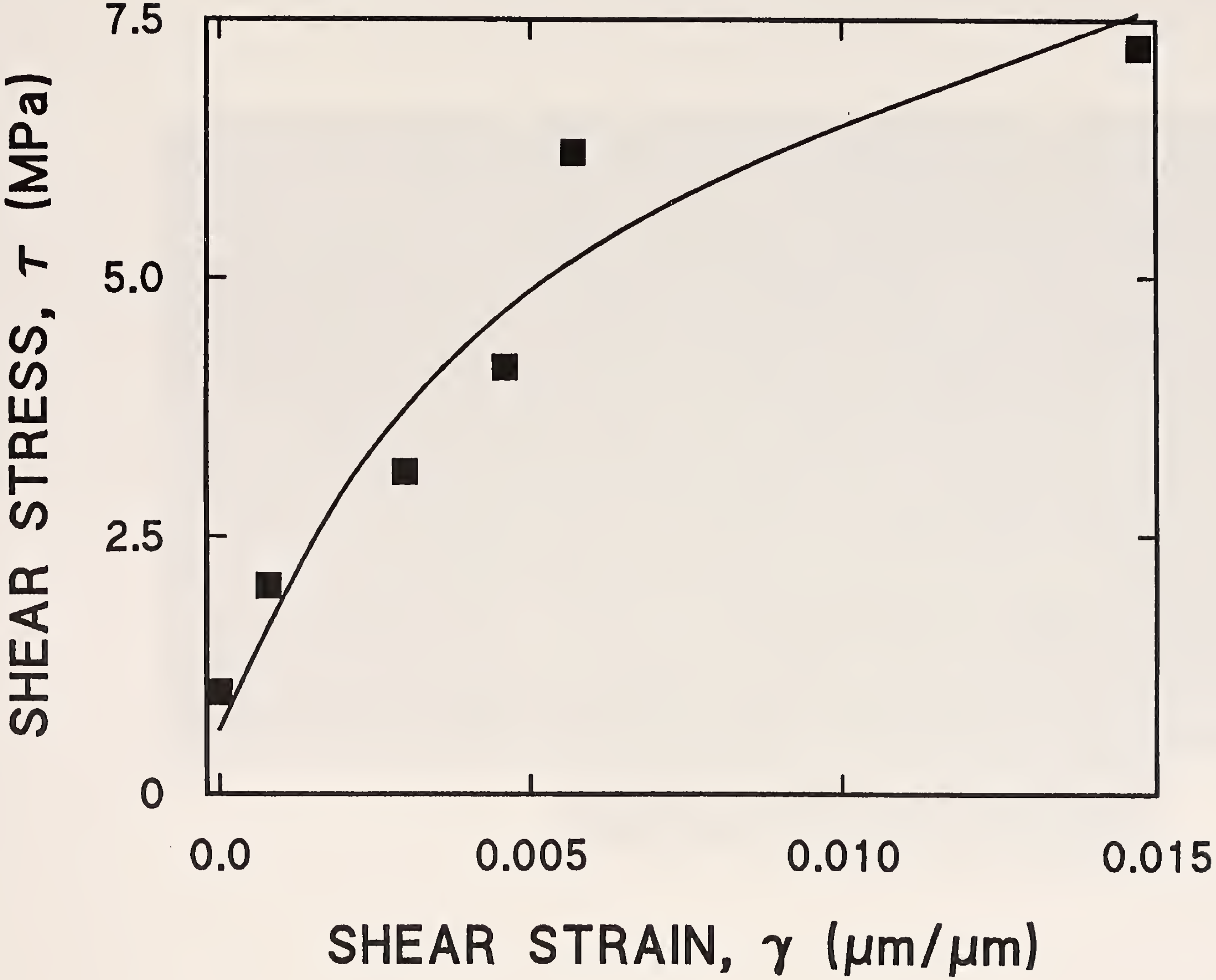
7.5
5.0
2.5
0
0.0
0.005
0.010
0.015
SHEAR STRESS, τ (MPa)
SHEAR STRAIN, γ (μm/μm)

Figure 5

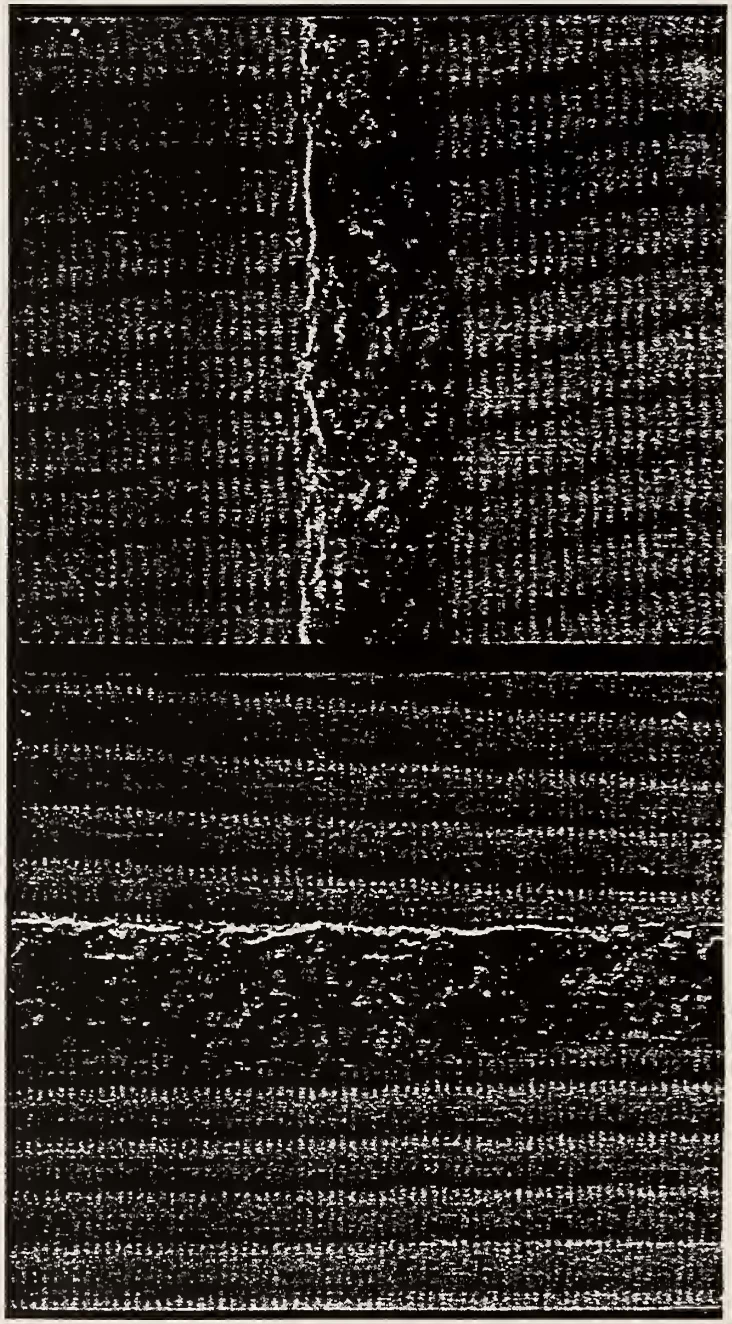

Figure 6

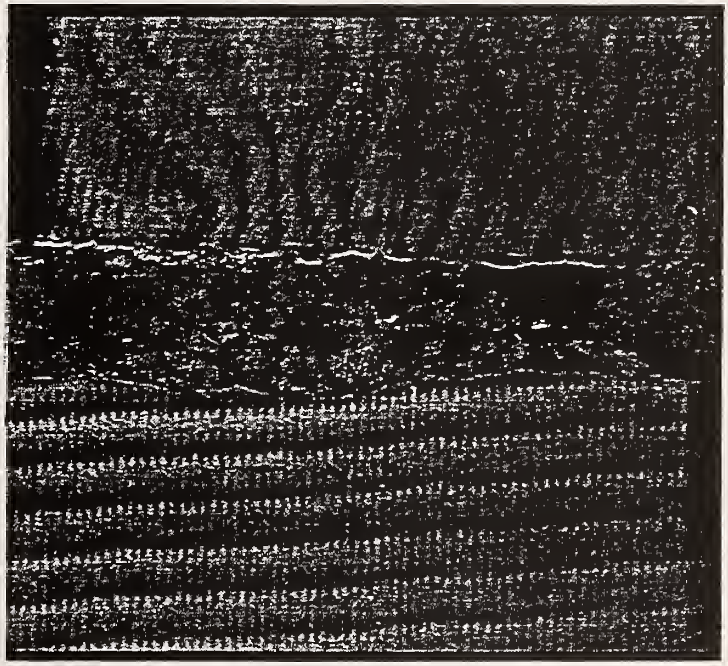

Figure 7

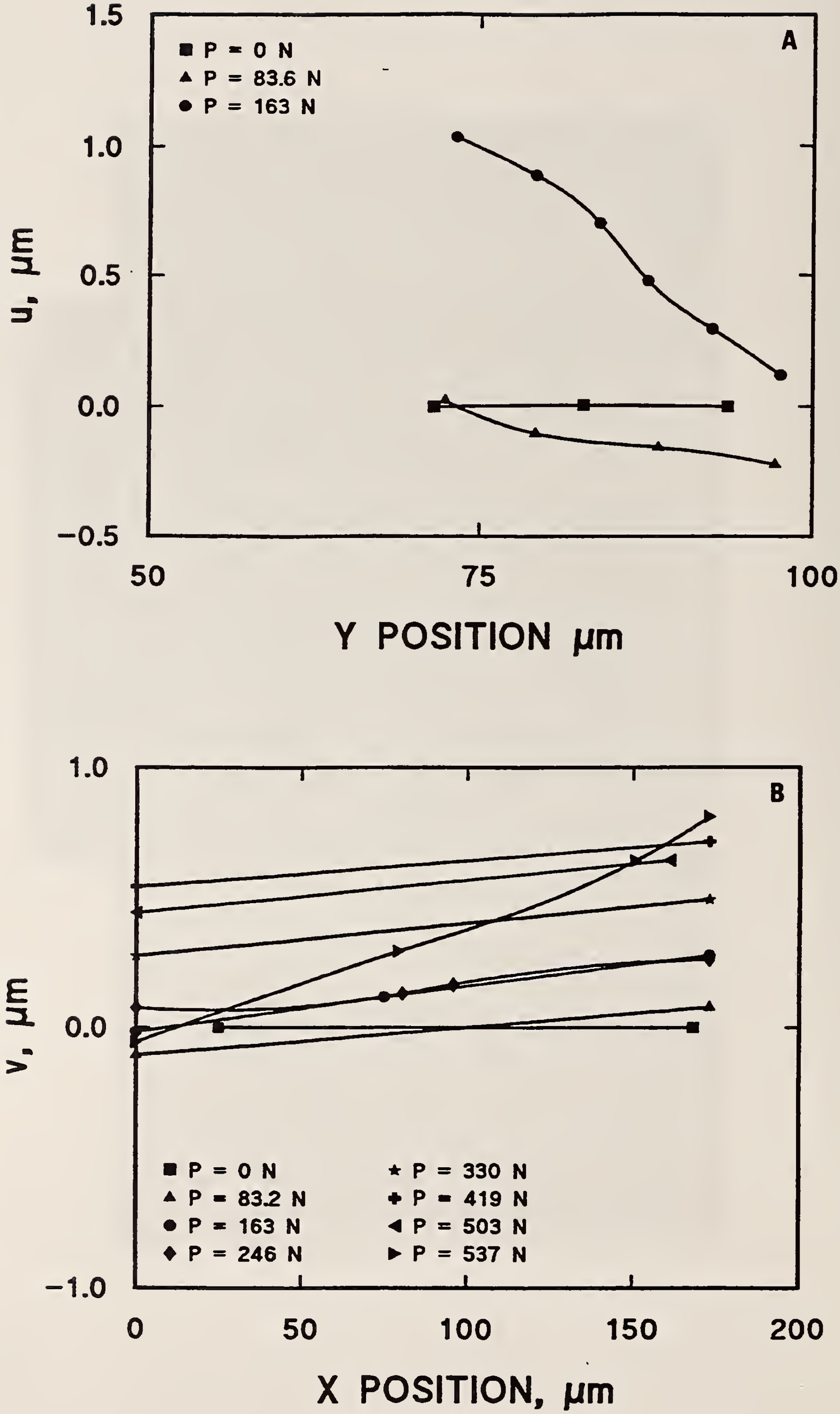
1.5
■ P = 0 N
▲ P = 83.6 N
● P = 163 N
A
1.0
0.5
0.0
−0.5
u, μm
50
75
100
Y POSITION μm
1.0
B
0.0
−1.0
v, μm
■ P = 0 N
▲ P = 83.2 N
● P = 163 N
◆ P = 246 N
★ P = 330 N
✚ P = 419 N
◀ P = 503 N
▶ P = 537 N
0
50
100
150
200
X POSITION, μm

Figure 8

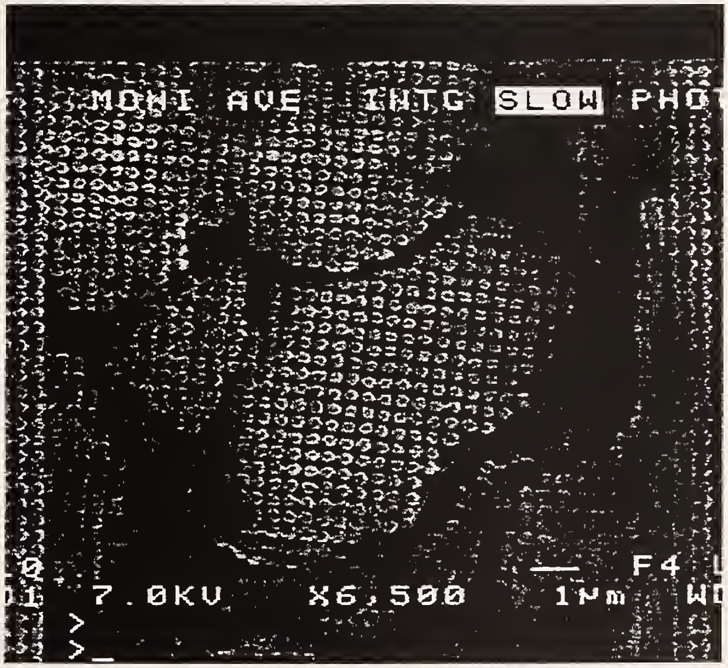

Figure 9

A9

Error Analysis and Thermal Expansion Measurement with Electron-Beam Moiré

by Berger, et al. (199?)

Error Analysis and Thermal Expansion Measurement with Electron-beam Moiré*

J. R. Berger[1], E. S. Drexler[2], and D. T. Read[2]

[1]Division of Engineering
Colorado School of Mines
Golden, Colorado 80401

[2] Materials Reliability Division
National Institute of Standards and Technology
Boulder, Colorado 80303

Abstract

We present a study of errors incurred when using the experimental technique of electron-beam moiré. We find that there are two sources of error: error manifested as an apparent magnification drift and error due to fringe tracing. The error due to fringe tracing is nearly negligible in comparison to the error due to magnification drift. We demonstrate the usefulness of the error estimate by investigating the thermal expansion of commercially pure copper. We find that our average result for the coefficient of thermal expansion is within 1.8% of handbook values for this material with a possible error due to apparent magnification drift of 9%.

Introduction

The experimental technique of electron-beam moiré is a relatively new member to the family of moiré methods. Based on the initial work of Kishimoto, et al. [1], Dally and Read [2, 3] developed the method to its present, mature state. The method relies extensively on the use of a scanning electron microscope (SEM) for both production of the specimen gratings and formation of a reference grating.

---

* Contribution of the National Institute of Standards and Technology, not subject to copyright.

The specimen gratings are produced using electron-beam (e-beam) lithography. Details of producing the specimen gratings are given in [2] where the importance of strict control over the process variables is emphasized.

The reference grating for e-beam moiré is produced by the raster scanning motion of the electron beam in the vacuum chamber of the SEM. As such, it is necessary to perform all tests within the SEM. The raster scanning of the electron beam is very similar to the scanning video moirė technique developed by Morimoto and Hayashi [4] for low-frequency specimen gratings. Unlike the traditional geometric [5] or interferometric [6] moiré methods, e-beam moiré allows one to easily vary the effective pitch of the reference grating by varying the beam controls on a typical SEM. Read and Dally [3] developed a model to interpret fringe fields obtained as the electron-beam diameter, the pitch of the raster scan, and the angle between the scan lines and grating lines were varied.

Our concern here is a determination of factors which may influence a measurement made with e-beam moiré at "fixed" settings on the SEM. This investigation was motivated by an attempt at benchmarking the method through a determination of the coefficient of thermal expansion in a bulk copper specimen. Initial measurements indicated that the fringe pattern appeared to change over time. This led us to a parametric study of the influence of instrument drift resulting in an apparent change in magnification and fringe tracing errors on the quantitative measurement of displacements.

Magnification Errors

Before studying possible error sources with e-beam moiré, it is instructive to identify the key parameters in formation of the reference grating. We are considering a scenario where the specimen grating has been prepared and the specimen placed within the vacuum chamber of the SEM. We view the moiré fringe pattern with no thermal or mechanical load on the specimen. As noted in previous studies [2, 3] it is usually not possible to obtain an ideal null field with e-beam moiré since the magnification is adjusted in discrete increments. Under these conditions, variations in the observed fringe field must be due to variations in those parameters which contribute to the formation of the reference grating. We first consider those factors which affect the pitch of the reference grating. As described in [2, 3], the pitch of the reference grating for e-beam moiré can be calculated as

$$p_{ref} = \frac{S}{MR}, \tag{1}$$

where S is the nominal image size, M is the magnification of the SEM, and R is the number of raster scan lines. The nominal image size, S, and the number of raster scan lines, R, are fixed for a given SEM during a given experiment. Therefore, according to eq (1), only a change in magnification over time can contribute to an apparent change in the pitch of the reference grating. The apparent change in magnification may be due to a number of instrument-related issues (accelerating voltage stability, stability of the electronic magnification unit, etc.). For this paper, we will treat all of these sources as an *apparent* change in magnification. Note that small changes in the magnification can contribute strongly to the apparent pitch of the reference grating since they are inversely proportional to each other. Read and Dally noted in [3] that the value of M must be precisely known for proper interpretation of the moiré fringe fields. They further noted that the apparent magnification from the SEM character display differed from actual measured magnifications by approximately 5% for the SEM used in their investigations. No time variation of M was considered by the authors.

If some variation occurs in the magnification of the SEM, we can write the pitch of the reference grating as

$$p_{ref} = \frac{S}{(M+\Delta M)R} , \tag{2}$$

where ΔM is the variation in the magnification. We consider the case of uniform axial strain on a specimen and calculate the error in the strain measurement due to the magnification variation. Relative to a null condition, Read and Dally [3] calculated the tensile strain in terms of reference and specimen grating frequencies as

$$\varepsilon = -\frac{f_i}{\left(f_{ref}+f_i\right)} . \tag{3}$$

Including a variation in magnification from eq (2) which effects both f_i and f_{ref}, eq (3) rewritten in terms of grating pitches is

$$\varepsilon = \frac{p_g MR}{S} - 1 + \frac{p_g R \Delta M}{S} , \tag{4}$$

where the last term represents the error term. It is helpful to consider the total strain as an apparent strain,

$$\varepsilon_{app} = \varepsilon_{true} + \varepsilon_{\Delta M} , \tag{5}$$

where

$$\varepsilon_{true} = \frac{p_g R M}{S} - 1 , \tag{6}$$

$$\varepsilon_{\Delta M} = \frac{p_g R \Delta M}{S} . \tag{7}$$

For purposes of this analysis, we can further simplify eq (7) by noting that, for small strains,

$$\frac{p_g R}{S} \approx \frac{1}{M} . \tag{8}$$

Equation (7) can then be written as

$$\varepsilon_{\Delta M} \cong \frac{\Delta M}{M} . \tag{9}$$

For a specific example, consider a specimen grating with p_g = 180 nm observed in the SEM at a nominal magnification of 1100X. From eq (1) we obtain a nominal reference grating pitch of p_{ref} = 170.5 nm for our SEM where S = 90 mm and R = 480 lines. Assume we subject the specimen to a uniform strain of 1200 με. From eq (3), assuming no change in the magnification, our specimen grating then has a pitch of p_g = 170.7 nm. At a value of ΔM = 0.20X (with a nominal magnification of 1100X) the additional strain obtained from eq (9) is 182 με. The error in the strain measurement would then be 15%, a significant error. To maintain less than 5% error in the strain measurement would require control on the magnification such that ΔM < 0.07X.

The above analysis highlights the necessity of strict control on magnification for quantitative measurements with e-beam moiré. As noted by Read and Dally [2], the nominal magnification must be accurately known for proper interpretation of the moiré field. It is now clear that not only must the nominal magnification be well known but the control on factors influencing the magnification must be exceptionally stable. We have treated all time-dependent errors as magnification errors for the reasons outlined at the beginning of this section. It is important to note that this error is *manifested* as an apparent drift in the magnification. Any drift in the instrument such as working distance, accelerating voltage, electronic magnification control, or other instrument-related issues can produce an apparent drift in the magnification. Our goal here is to study the influence of these apparent magnification drifts and not to isolate the precise cause for a given test on our particular instrument.

Studies of the Temporal Variation of the Fringe Fields

A series of experiments were performed in order to identify and quantify factors which varied with time in a typical e-beam moiré experiment. For each of the experiments, a single homogeneous, polycrystalline copper specimen (99.999% pure copper) was used. The specimen was disk-shaped with a diameter of 5 mm and a thickness of 2 mm. The specimen was instrumented with a line grating located near the center of the specimen with p_g = 180 nm. The specimen grating was etched into the surface of the copper. The specimen was placed in the SEM and all tests were performed at a magnification setting of 1100X. This is the magnification setting associated with the near null-field for the specimen grating frequency used in this experiment. The temperature of the testing stage was monitored during the acquisition of images. The maximum temperature variation observed in all of our tests was ± 0.6 °C.

For our initial test, moiré fringe fields were obtained at fixed settings on the SEM over a period of 240 minutes at 30 minute intervals. For the particular test analyzed here we had an initial field of approximately 4 fringes. We have also observed that the number of fringes in the initial field may vary for a given specimen grating due to slight changes in either working distance or focus as the SEM is set up for a particular experiment.

Each acquired image was analyzed to obtain the average number of moiré fringes across the image. The analysis was based on a fringe analysis program developed at NIST. The program requires the user to specify points located along a fringe center. The software then performs a spline-fit to the data. Obviously some statistical variation can occur due to errors in locating the fringe center or from the use of different subsets of data from the same moiré field. Similar errors were noted by Barker, et al. [8] in analyzing moiré data collected near crack tips. We address the variation in the average number of fringes due to these errors below.

The average number of fringes across each acquired image as a function of time is shown in Fig. 1. A clear variation in the average number of fringes occurs over time. Note that the first data point shows the greatest variation from the mean value. This was typical of all the experiments we performed. For the data shown in the figure, we obtain a mean value of 4.34 fringes with a standard deviation of 0.14 fringes. Our field of observation at 1100X is 81.8 μm which yields a mean moiré fringe frequency of 0.0530 fringes/μm with a standard deviation of 0.0017 fringes/μm. Assuming this variation in the fringe field is strictly due to factors influencing the magnification of the SEM, we can calculate from the apparent change in magnification required to produce one standard deviation. We first calculate from eqs (1) and (2) the nominal magnification required to produce the observed moiré field frequency. We obtain a nominal magnification of $M =$ 1056X. The magnification was set on the SEM at 1100X, our calculated value is within the usual 5% error allowed in the magnification calibration. To produce one standard deviation in the fringe field we predict a value of $\Delta M = 0.32$X for the data shown in Fig. 1.

As noted above we usually observed the greatest variation in the fringe field with the first data point. This suggests that the instrument has not yet stabilized and experiments should only be performed after waiting a period of time. If we only consider the data points obtained after 30 minutes had elapsed we obtain a mean value of 4.30 fringes with a standard deviation of 0.07. The mean value is comparable to that obtained previously with all data points. Therefore, our nominal magnification is approximately the same ($M =$ 1056X). We note that the standard deviation has decreased from 0.14 to 0.07. We obtain a value of $\Delta M = 0.16$ required to produce one standard deviation in the fringe field. This is perhaps a more realistic estimate for expected variations in the apparent magnification.

The probe current in the SEM was initially suspected of producing apparent variations in the fringe field. This was based on recordings of probe current over time as each experiment was performed. To investigate the likelihood of probe current causing variations in the fringe field we performed a series of tests where the probe current was varied and images acquired. The average number of fringes plotted as a function of probe current is shown in Fig. 2. For this particular data set, the mean number of fringes is 4.95 with a standard deviation of 0.10. In comparison with Fig. 1 it is clear that the variation we observed over time is approximately the same as the variation observed over the time we varied the probe current. Note in Fig. 2 that the probe current was varied from approximately 0 pA to -100 pA. The observed variation in probe current during tests similar to that which provided the data in Fig. 1 was only ± 0.6 pA. We therefore concluded that the probe current was not responsible for the observed temporal variation in the fringe field.

Finally, we considered the variation in the average number of fringes due to the fringe tracing procedure. To investigate this we acquired an image and performed six independent tracings of the fringe centers with the fringe analysis software used in our study. Of concern here was variation in the location of the center of the fringes and the effect of the number of points along each fringe center in the spline-fit to the data. The results are shown in Fig. 3 for the average number of fringes across the entire image for each of our tracings. As shown in the figure, a variation of approximately ± 0.05 fringes occurs with a standard deviation of 0.02 fringes This is far below the observed variation over time shown in Fig. 1. We conclude that fringe tracing is not responsible for the observed variation in the fringe field.

Coefficient of Thermal Expansion for Copper

To provide a benchmark for the e-beam moiré method in thermal stress studies we performed two experiments to determine the coefficient of thermal expansion, α, of copper. The first experiment used a copper specimen with a geometry identical to that of the specimen previously described but with a line grating of pitch 900 nm. The second experiment was performed using the same specimen used for the studies of the temporal variation of the fringe field. Both specimens had line gratings which were etched into the surface of the specimen to avoid high temperature deterioration of the PMMA coating normally used for producing gratings with e-beam lithography. Both specimens were tested on a thermal stage in the SEM. The heating/cooling stage fits securely on the shuttle base within the SEM chamber. The resistive heating unit has a temperature range to 400 °C. The stage is cooled by circulating liquid nitrogen chilled nitrogen gas through the stage. The stage can be cooled down to -185 °C. A platinum resistance thermocouple is located just below the specimen and the desired stage temperature is achieved through balancing the heater output and the chilled gas. The entire stage is electrically grounded and the 10^{-5} torr vacuum of the SEM chamber minimizes heat transfer.

The procedure for both experiments was the same. The specimen was placed in the vacuum chamber of the SEM and thermally cycled twice between -50 °C and +150 °C. The temperature was then set at the starting temperature for the test of -50 °C. Images of the moiré field were acquired at intervals of approximately 50 °C. After each increment in temperature the specimen was allowed to equilibrate before acquisition of the moiré field. For assessing equilibrium we waited until the fringe field changed less than 0.25 fringes per minute across the field of view. This required waiting a maximum of 30 minutes. Typical fringe fields are shown in Fig. 4 at temperatures of -49.6 °C and 150.6 °C.

The average number of fringes across the field as a function of temperature are plotted in Figs. 5a and 5b for the two tests we performed. The first test, shown in Fig. 5a, was conducted before we were aware of possible errors due to temporal variations in the fringe field. Only three data points were obtained in that test. After observing the temporal variations in the fringe fields detailed in the first part of this paper we repeated the experiment but collected data during both heating and cooling of the specimen. Shown in Fig. 5b are the mean values of the data at each temperature with bars indicating the spread in the data.

We calculate the coefficient of thermal expansion from the fringe field following Bowles, et al. [9]. We are only interested in the *change* of fringe order with temperature over the uniform displacement field so we calculate the slope of the average number of fringes with respect to temperature, s_f. The coefficient of thermal expansion can then be directly calculated as

$$\alpha = \frac{s_f}{R} . \tag{10}$$

From eq (10) we can estimate α by dividing the slope of a best-fit line through the data in Figs. 5a and 5b by R (recall that $R = 480$ for our SEM). Summarized in Table I are the results of this calculation.

Table I

Coefficient of Thermal Expansion from the E-beam Moiré Data

Test	Slope, s_f	Correlation Coefficient, r	α (/°C)
1 (Fig. 9)	8.61×10^{-3}	0.997	17.6×10^{-6}
2 (Fig. 10)	6.96×10^{-3}	0.966	14.8×10^{-6}
		Average $\alpha =$	16.2×10^{-6}

The average coefficient of thermal expansion from the moiré data can be compared to a handbook value [10] of $\alpha = 16.5 \times 10^{-6}$ /°C for pure copper. Our average result is apparently within 1.8% of the handbook value. However, we must inspect our result in light of the parametric studies performed on the apparent magnification drift.

Estimate of the Error

Based on the parametric studies detailed in the previous section we concluded that variation in the apparent magnification in the SEM is the principal source of error. This variation is not due to probe current drift. Magnification drift in the SEM can occur through slight variations in the high accelerating voltage, through drift of the magnification control unit, or other instrument-related factors. Clearly we are expecting a level of performance and stability from the SEM which it was not intended to meet. The drift of ± 0.32X at 1100X which produced one standard deviation in the fringe field for the experiment of Fig. 1 represents a variation of only ± 0.03% in the magnification.

We now consider a variation in apparent magnification during a thermal expansion test. The apparent coefficient of thermal expansion can be calculated from the apparent strains as

$$\alpha_{app} = \frac{\Delta\varepsilon_{app}}{\Delta T}. \tag{11}$$

provided the thermal strains are linear over the temperature increment ΔT. Writing the apparent strains as shown in eq (5) we have

$$\alpha_{app} = \frac{\Delta\varepsilon_{true}}{\Delta T} + \frac{\Delta\varepsilon_{app}}{\Delta T}. \tag{12}$$

We can put this equation in a more useful form as

$$\alpha_{app} = \alpha_{true}\left(1 + \frac{\Delta M}{\alpha_{true} M \Delta T}\right), \tag{13}$$

where

$$\alpha_{true} = \frac{\Delta\varepsilon_{true}}{\Delta T}\,. \tag{14}$$

Based on our investigations concerning the apparent variation in magnification, we are concerned with apparent variations in magnification of approximately 0.32X at 1100X. From eq (13) we obtain

$$\frac{\alpha_{app}}{\alpha_{true}} = 1.088\,.$$

We can therefore anticipate obtaining an estimate of the coefficient of thermal expansion to within approximately 9%. If we consider the average value of the coefficient of thermal expansion given in Table I and the values obtained from the individual experiments of Figs. 5a and 5b, we obtain $\alpha = 16.2 \times 10^{-6}$ /°C ± 8.5%. This is consistent with the anticipated error in the measurement predicted from eq (13).

Summary

We have presented a study concerning the magnitude of errors from a variety of sources when using e-beam moiré. Based on parametric studies of the temporal variation of the fringe patterns we identified the major source of error as being an apparent magnification drift. It was demonstrated that the magnification error causes a change in the frequency of the observed moiré field. For the simple case of uniform strain the error was non-negligible for typical values of magnification drift. This demonstrates the need for strict monitoring and control of the magnification when performing measurements with e-beam moiré. Finally, we calculated the coefficient of thermal expansion for copper in light of these potential errors. We obtained an average value for the coefficient of thermal expansion within 1.8% of handbook values. This result was fortuitous as our expected error in the measurement due to the apparent drift in magnification was approximately 9%. Future work will focus on the issue of magnification control and stability in the SEM.

Acknowledgment

One of us (JRB) acknowledges the support of the National Science Foundation and the National Institute of Standards and Technology under the joint NSF-NIST program CMS-9522147 and additional support provided by the Materials Reliability Division of NIST.

References

[1] Kishimoto, S., Egashira, M., and Shina, N., "Measurements of Grain Boundary Sliding and Observations of Microgrids for High Temperature Use," *Journal of the Society for Materials Science Japan*, Vol. 40, pp. 637-641 (1991).

[2] Dally, J. W. and Read, D. T., "Electron-beam Moiré," *Experimental Mechanics*, Vol. 33, pp. 270-277 (1993).

[3] Read, D. T. and Dally, J. W., “Theory of Electron-beam Moiré,” *Journal of Research of the National Institute of Standards and Technology,* Vol. 101, pp. 47-61 (1996).

[4] Morimoto, Y. and Hayashi, T., “Deformation Measurement During Powder Compaction be a Scanning Moiré Method,” *Experimental Mechanics,* Vol. 24, pp. 112-116 (1984).

[5] Durrelli, A. J. and Parks, V. J., *Moiré Analysis of Strain*, Prentice-Hall, Englewood Cliffs, NJ, 1970.

[6] Post, D., Moiré Interferometry, *Handbook on Experimental Mechanics,* Society for Experimental Mechanics, Bethel, CT, 1989.

[7] Dally, J. W. and Riley, W. F., *Experimental Stress Analysis,* Third Edition, McGraw Hill (1992).

[8] Barker, D. B., Sanford, R. J., and Chona, R., Determining K and related stress-field parameters from displacement fields, *Experimental Mechanics*, Vol. 25, 399-407 (1985).

[9] Bowles. D. E., Post, D., Herakovich, C. T., and Tenney, D. R., “Moiré Interferometry for Thermal Expansion of Composites,” *Experimental Mechanics*, Vol. 21, pp. 441-447 (1981).

[10] *Handbook of Chemistry and Physics*, David R. Lide, Editor in Chief, 74th Edition, CRC Press, Boca Raton, Florida (1993).

List of Figures

Fig. 1 Average number of fringes for the copper specimen as a function of time.

Fig. 2 Average number of fringes as the probe current is varied.

Fig. 3 Average number of fringes from different tracings of the fringe pattern with the fringe pattern analysis software used in this study.

Fig. 4 Typical e-beam moiré fields acquired at temperatures of -49.6° C and 150.6° C

Fig. 5a First test for the average number of fringes as a function of temperature change for the copper specimen.

Fig. 5b Second test for the average number of fringes as a function of temperature change for the copper specimen. Shown are the mean values obtained at each temperature increment. The error bars indicate the variation in the experimental data.

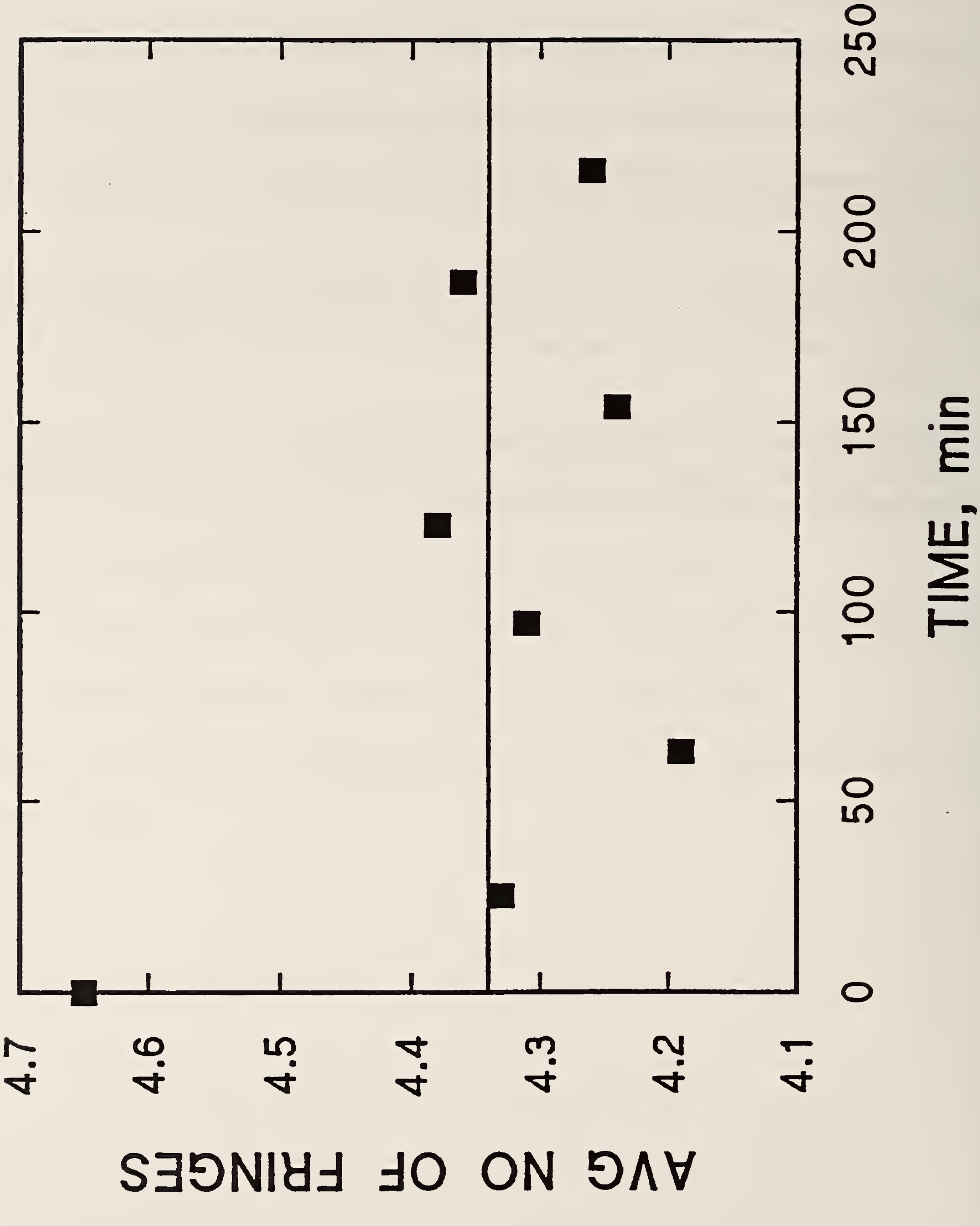

Berger, Drexler, and Read, Fig. 1

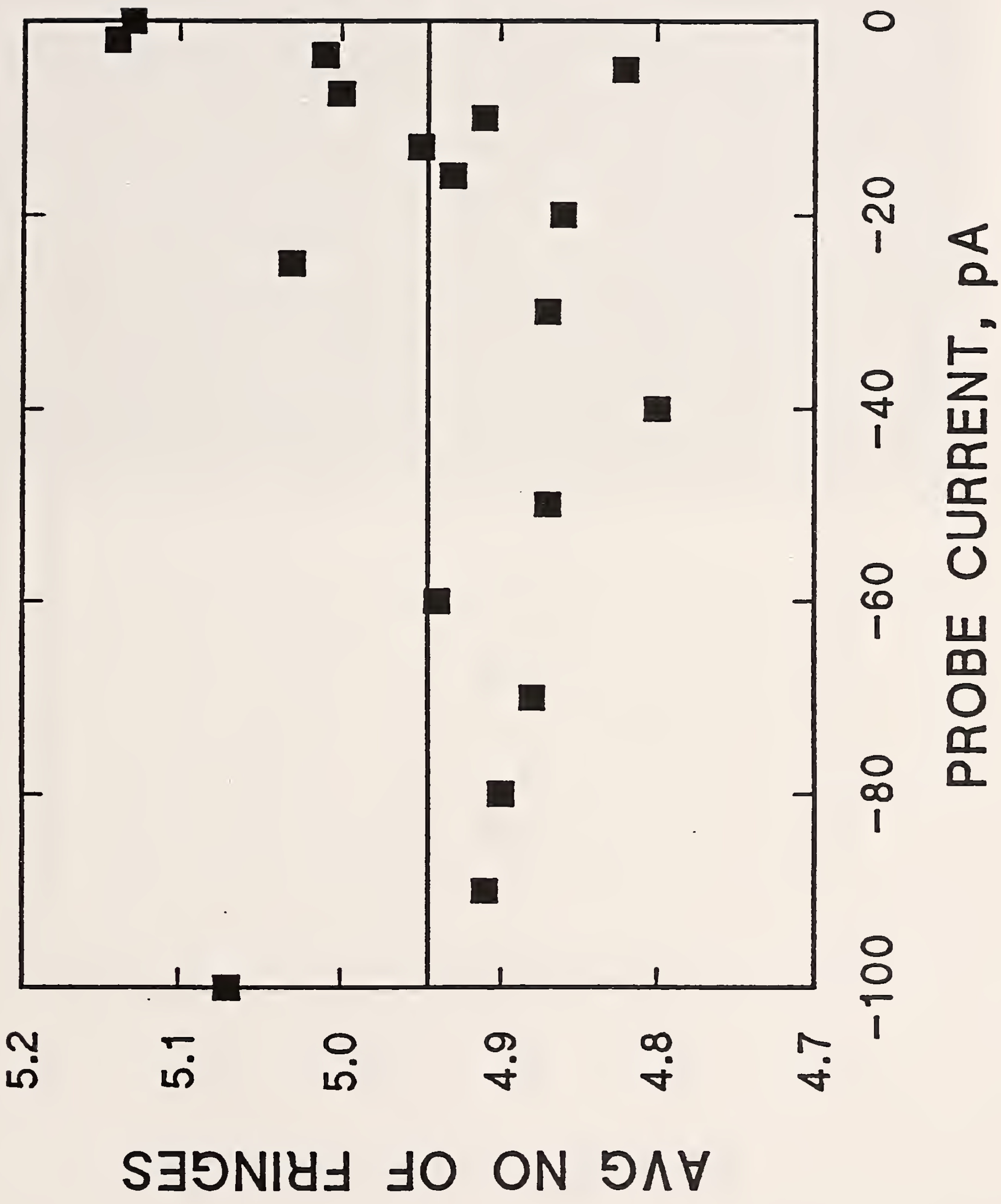

Berger, Drexler, and Read, Fig. 2

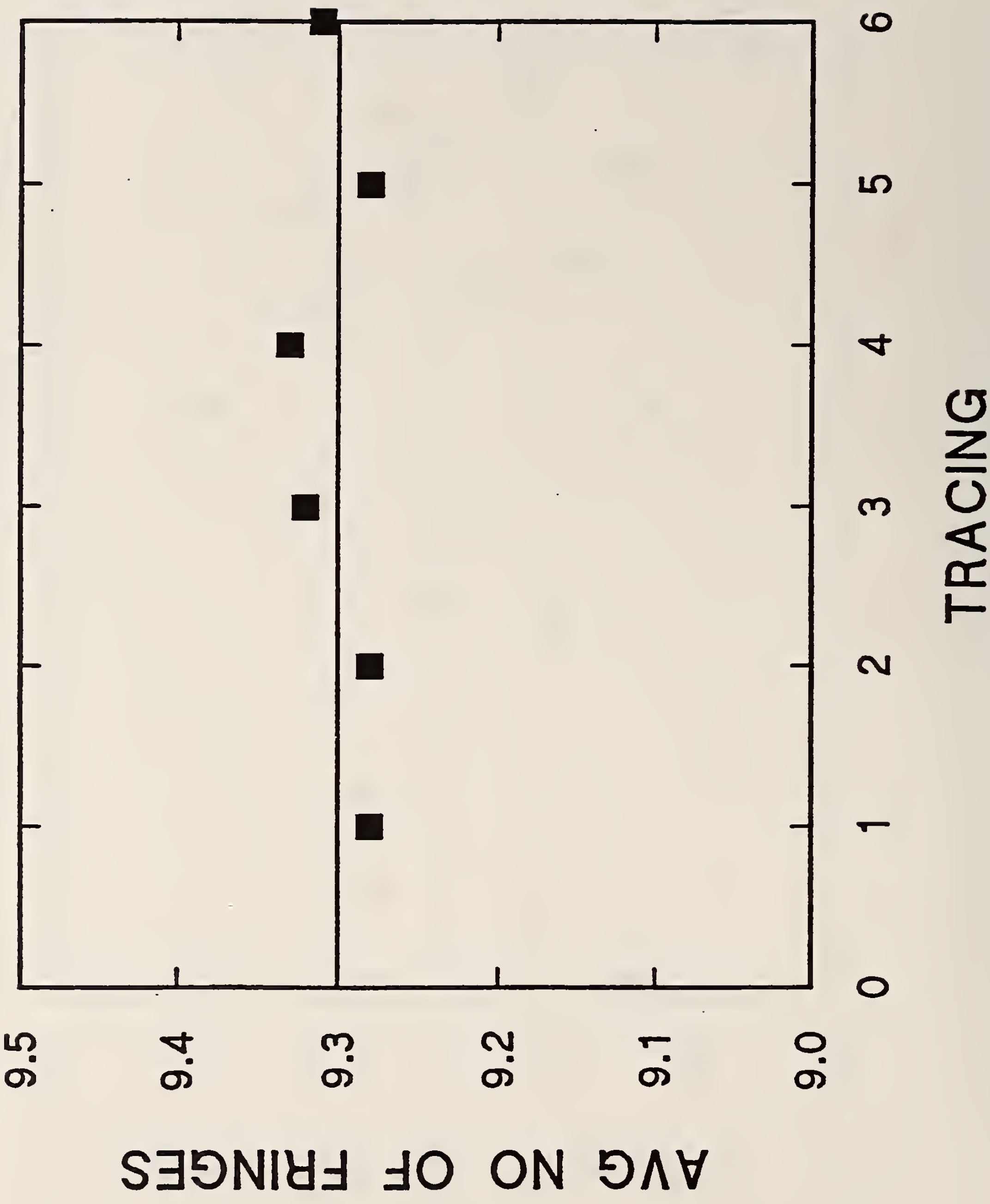

Berger, Drexler, and Read, Fig. 3

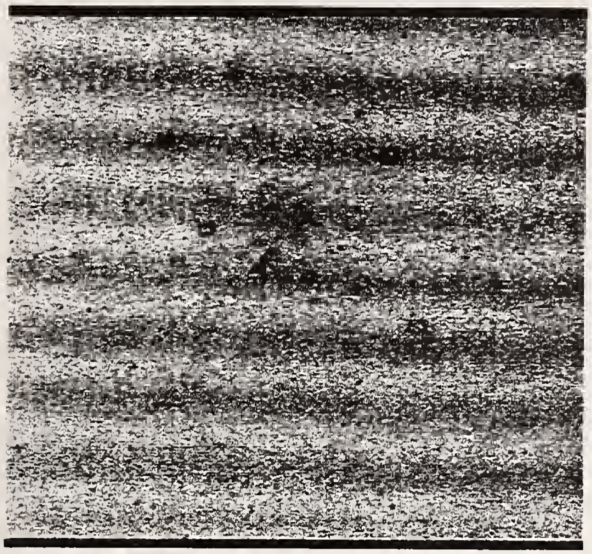

-49.6 C

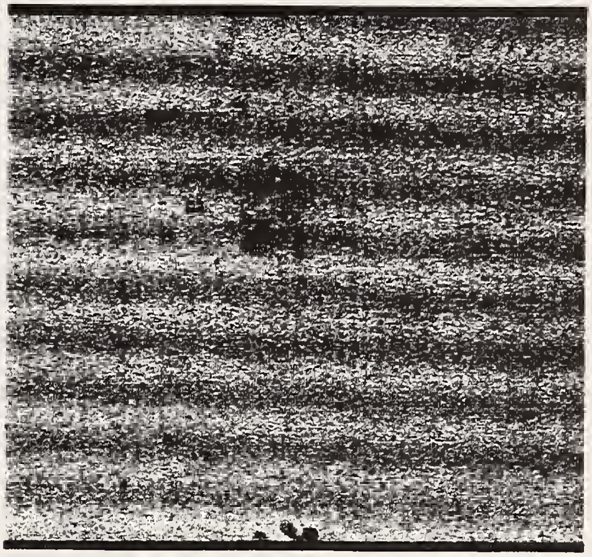

150.6 C

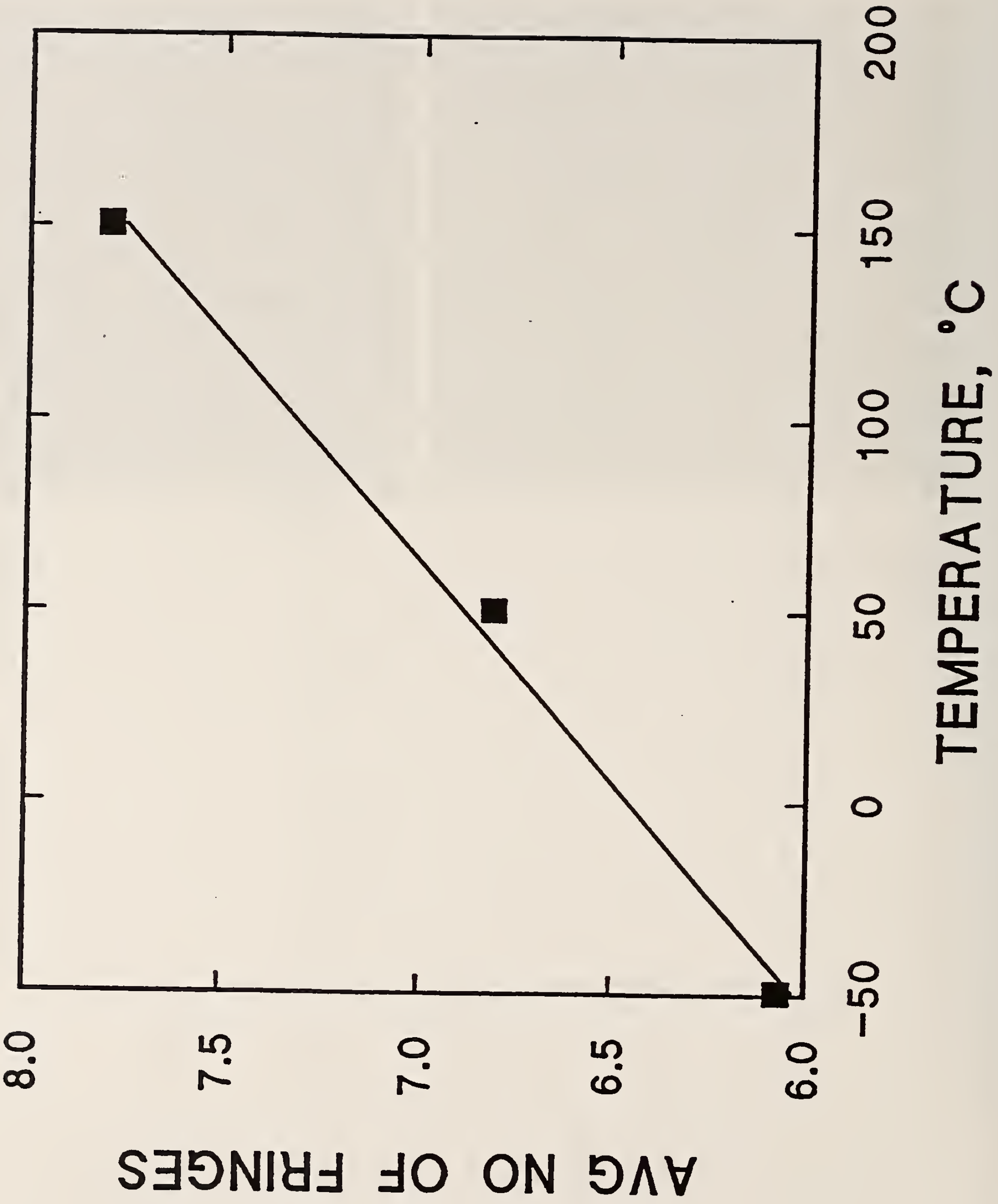

Berger, Drexler, and Read, Fig. 5a

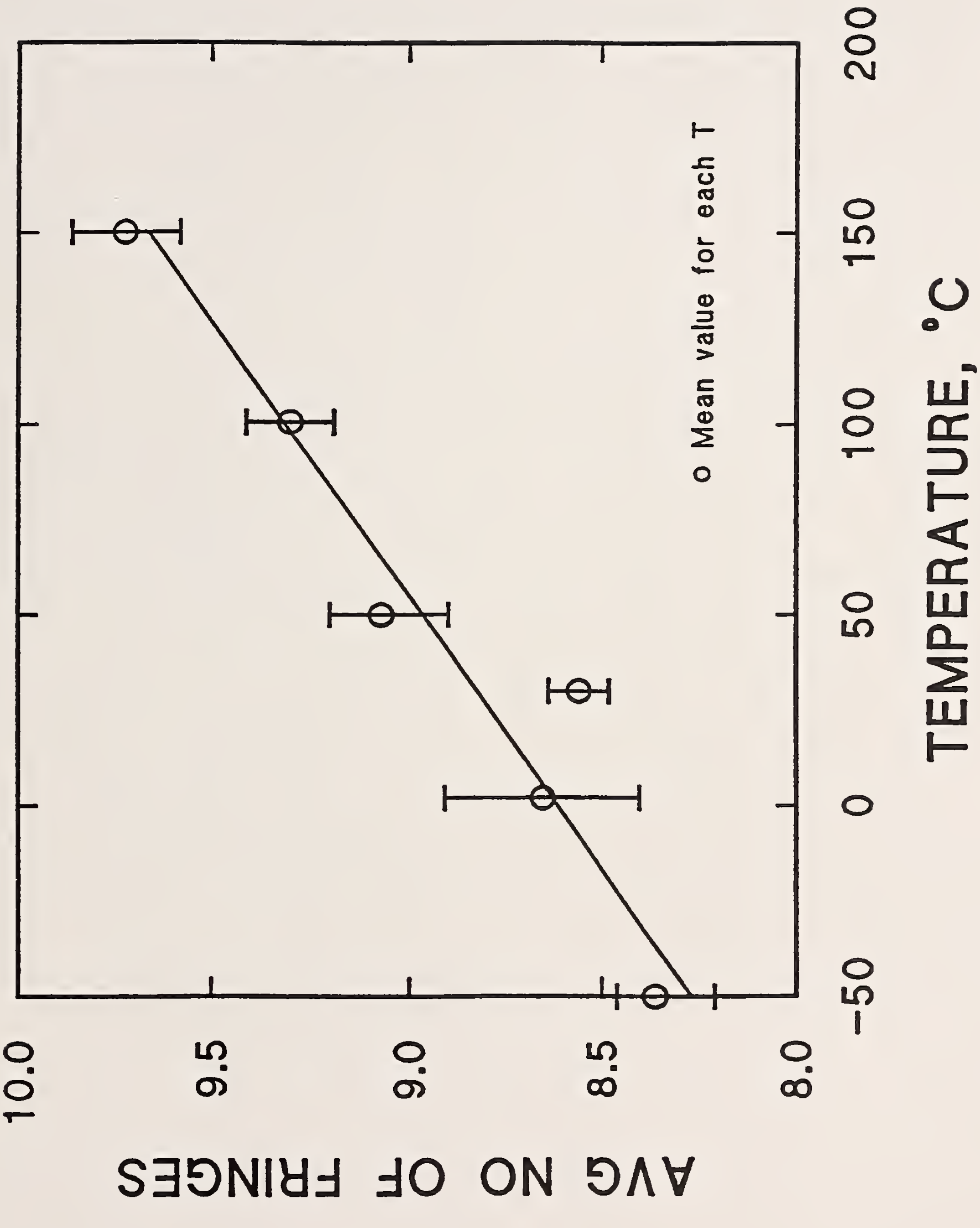

Berger, Drexler, and Read, Fig. 5b

Appendix B: Program Disk

NIST Technical Publications

Periodical

Journal of Research of the National Institute of Standards and Technology—Reports NIST research and development in those disciplines of the physical and engineering sciences in which the Institute is active. These include physics, chemistry, engineering, mathematics, and computer sciences. Papers cover a broad range of subjects, with major emphasis on measurement methodology and the basic technology underlying standardization. Also included from time to time are survey articles on topics closely related to the Institute's technical and scientific programs. Issued six times a year.

Nonperiodicals

Monographs—Major contributions to the technical literature on various subjects related to the Institute's scientific and technical activities.

Handbooks—Recommended codes of engineering and industrial practice (including safety codes) developed in cooperation with interested industries, professional organizations, and regulatory bodies.

Special Publications—Include proceedings of conferences sponsored by NIST, NIST annual reports, and other special publications appropriate to this grouping such as wall charts, pocket cards, and bibliographies.

Applied Mathematics Series—Mathematical tables, manuals, and studies of special interest to physicists, engineers, chemists, biologists, mathematicians, computer programmers, and others engaged in scientific and technical work.

National Standard Reference Data Series—Provides quantitative data on the physical and chemical properties of materials, compiled from the world's literature and critically evaluated. Developed under a worldwide program coordinated by NIST under the authority of the National Standard Data Act (Public Law 90-396). NOTE: The Journal of Physical and Chemical Reference Data (JPCRD) is published bimonthly for NIST by the American Chemical Society (ACS) and the American Institute of Physics (AIP). Subscriptions, reprints, and supplements are available from ACS, 1155 Sixteenth St., NW, Washington, DC 20056.

Building Science Series—Disseminates technical information developed at the Institute on building materials, components, systems, and whole structures. The series presents research results, test methods, and performance criteria related to the structural and environmental functions and the durability and safety characteristics of building elements and systems.

Technical Notes—Studies or reports which are complete in themselves but restrictive in their treatment of a subject. Analogous to monographs but not so comprehensive in scope or definitive in treatment of the subject area. Often serve as a vehicle for final reports of work performed at NIST under the sponsorship of other government agencies.

Voluntary Product Standards—Developed under procedures published by the Department of Commerce in Part 10, Title 15, of the Code of Federal Regulations. The standards establish nationally recognized requirements for products, and provide all concerned interests with a basis for common understanding of the characteristics of the products. NIST administers this program in support of the efforts of private-sector standardizing organizations.

Consumer Information Series—Practical information, based on NIST research and experience, covering areas of interest to the consumer. Easily understandable language and illustrations provide useful background knowledge for shopping in today's technological marketplace.

Order the **above** *NIST publications from: Superintendent of Documents, Government Printing Office, Washington, DC 20402.*

Order the **following** *NIST publications—FIPS and NISTIRs—from the National Technical Information Service, Springfield, VA 22161.*

Federal Information Processing Standards Publications (FIPS PUB)—Publications in this series collectively constitute the Federal Information Processing Standards Register. The Register serves as the official source of information in the Federal Government regarding standards issued by NIST pursuant to the Federal Property and Administrative Services Act of 1949 as amended, Public Law 89-306 (79 Stat. 1127), and as implemented by Executive Order 11717 (38 FR 12315, dated May 11, 1973) and Part 6 of Title 15 CFR (Code of Federal Regulations).

NIST Interagency Reports (NISTIR)—A special series of interim or final reports on work performed by NIST for outside sponsors (both government and non-government). In general, initial distribution is handled by the sponsor; public distribution is by the National Technical Information Service, Springfield, VA 22161, in paper copy or microfiche form.

U.S. Department of Commerce
National Institute of Standards and Technology
325 Broadway
Boulder, Colorado 80303-3337

Official Business
Penalty for Private Use, $300